國立交通大學

光電工程研究所

博士論文

廣義光管在照明與顯示系統之應用與探索

Generalized Light Pipe and Light Guide: Exploration and its Applications to Illumination and Ultra-thin Display

研究生：鄭伊凱

指導教授：陳志隆教授

中華民國 九十八 年 一 月

廣義光管在照明與顯示系統之應用與探索

Generalized Light Pipe and Light Guide: Exploration and its Applications to Illumination and Ultra-thin Display

研究生：鄭伊凱　　Student : Yi-Kai Cheng

指導教授：陳志隆　　Advisor : Jyh-Long Chern

國立交通大學

光電工程研究所

博士論文

A Dissertation
Submitted to Department of Photonics, Institute of Electro-Optical Engineering
College of Electrical and Computer Engineering
National Chiao Tung University
in Partial Fulfillment of the Requirements
for the Degree of Doctor of Philosophy
in
Electro-Optical Engineering
January 2009
Hsinchu, Taiwan

中華民國 九十八 年 一 月

廣義光管在照明與顯示系統之應用與探索

博士研究生：鄭伊凱　　指導教授：陳志隆教授

國立交通大學　　光電工程研究所

摘 要

在現今的光電產品中，光管與光導管一直是最基本與最重要的元件之一。有鑑於此，許多具有高傳輸效率或特殊需求的光管陸續被開發設計出來。以往，在照明設計的領域中，最佳化被視為困難的事情。如今拜電腦發達之賜，目前的商用光學軟體已逐漸提供設計者相當多的設計自由度，甚至自動最佳化的功能。然而，一組優良的起始設計或架構是軟體無法提供的。基於對於初始架構了解的需要，因此本論文探討了光線在光管與光導管中的基本行為與傳遞的機制。

本論文利用基礎的數學解析，模擬軟體的檢驗，與實際實驗的確認，探索了下列各項光管與光導管的基本特性：

（一）分析朗博光源在長直多邊型光管出口面的照度分布，特別是圓形和五邊型光管的能量集中現象，並包含了中空與折射材質。

（二）提出兩種光管架構，達到可以保持光學偏振特性並使出光方向偏折任意特定角度的角度偏移器。

（三）對於應用在超薄投影顯示器的楔形光導板的成像品質作像差分析，並對其特有的暗帶現象提出解決方案。同時將楔形光導板的概念延伸為全新的環場投影顯示器。

由本論文的探討，使設計者可以更加了解光管與光導管的基礎特徵，幫助設計者掌握其運作原理，並對於未來照明產品的設計與應用帶來更大的助益。

Generalized Light Pipe and Light Guide: Exploration and its Applications to Illumination and Ultra-thin Display

Doctoral Student: Yi-Kai Cheng **Advisor:** Dr. Jyh-Long Chern

Institute of Electro-Optical Engineering

National Chiao Tung University

Abstract

In current electro-optical product, light pipe and light guide are most basic and important elements. Thus, many light pipes with high transmission efficiency or special function are designed and developed. Formerly, in illumination design, the optimization was regarded as difficult work. By the development of computer, current commercial optical simulation package has provided the designer more and more design degrees of freedom, even an automatic optimization function. However, a fine initial design or configuration is unable to provide by software. Based on the requirement of regarding initial configuration, thus in this study, we discuss the basic behavior and the transmission mechanism for ray in light pipe and light guide.

By mathematical analysis, simulation verification, and experimental confirm, this study explores some fundamental characters of light pipes and light guides:

(1) Analysis of irradiance distributions of a Lambertian source in hollow and dielectric-filled straight polygonal light pipes, especially the flux localizations of circular and pentagonal light pipes.

(2) Proposing of two kinds of angular shifter which can preserve polarization and providing any desired angular deflection of the transmitted light.

(3) Providing aberration analysis for ultra-thin wedge plate display and proposing solutions to reduce dark zone. Also extending the conception of wedge plate light guide to a new circular display.

This study can help designers to further understand the fundamental property of light pipe and light guide, and have benefit to the designs and the applications for future illumination products.

誌　謝

感謝上天！終於完成這漫長的學業，感謝我的老闆忍耐了我這麼久，感謝父母親對我的栽培，感謝每一位曾經幫助我的人，謝謝。

2009.01 於交通大學

Table of Contents

Figure Captions

Table Captions

Chapter 1

Introduction

1-1 Historical Survey on the Development of Illumination

The history of illumination starts in the times when the humankind learned to produce fire. The first means of illumination were fires and cressets. Candles and oil lamps appeared later. Illumination means to use different kind of light sources to illuminate a specific place or environment. The light source includes both artificial light sources such as lamps and natural illumination of interiors from daylight. Artificial illumination (or lighting) is most commonly provided today by electric lights, but gas lighting, candles, or oil lamps were used in the past, and still are used in certain situations. Several common artificial light sources are introduced as below [1-1]:

1. **Candle:** The Latin word "candere" means to flicker. The early candle was made from various forms of natural fat, tallow, and wax. The Egyptians and Cretans made the candle from beeswax, as early as 3000 B.C. Candle was used in illumination before the invention of electric lights. In nowadays, candles are often used for festival or special commemoration days.

Figure 1-1-1 A burning candle

2. **Kerosene Lamp:** The kerosene lamp is the lighting device which uses kerosene as a fuel. It is the main light source before the prevalence of electric lights. The first kerosene lamp was found at Baghdad in 9th century. A more modern kerosene lamp was later constructed by a Polish inventor in 1853.

Figure 1-1-2 Kerosene lamp

3. **Incandescent Lamp:** It is a source of electric light that works by an electric current passes through a thin filament, heating it until it produces light. The enclosing glass bulb prevents the oxygen in air from reaching the hot filament. After 1879, Thomas A. Edison improved the lamp filament by tungsten. In 1906, the General Electric Company patented a method of making tungsten filaments for use in incandescent light bulbs. Finally improvements in efficiency and low cost for production of incandescent lamps were solved; the incandescent lamp with tungsten filament had been used until now.

Figure 1-1-3 Incandescent lamp

4. **Halogen Lamp:** A halogen lamp is an incandescent lamp in which a tungsten filament is sealed into a compact transparent envelope filled with an inert gas, plus a small amount of halogen such as iodine or bromine. The halogen cycle increases the lifetime of the bulb and prevents its darkening by redepositing tungsten from the inside of the bulb back onto the filament. Halogen lamp has a higher efficacy than a standard gas filled lamp. Because of their smaller size, halogen lamps can advantageously be used with optical systems that are more efficient.

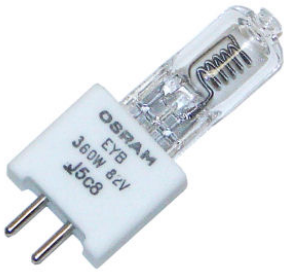

Figure 1-1-4 Halogen lamp

5. **Fluorescent Lamp:** A fluorescent lamp or fluorescent tube is a gas-discharge lamp that uses electricity to excite mercury vapor. The excited mercury atoms produce short-wave ultraviolet light that then causes a phosphor to fluoresce, producing visible light. Unlike incandescent lamps, fluorescent lamps always require a ballast to regulate the flow of power through the lamp. However, a fluorescent lamp converts electrical power into useful light more efficiently than an incandescent lamp. While larger fluorescent lamps have been mostly used in large commercial or institutional buildings, the compact fluorescent lamp is now being used as an energy-saving alternative to incandescent lamps in homes.

Figure 1-1-5 Different kinds of fluorescent lamp

6. **Neon Lamp:** A neon lamp is a gas discharge lamp containing primarily neon other inert gases at a low pressure. Applying a high voltage (usually a few thousand volts) makes the gas glow brightly. Neon Lamps are usually used for signboard which produced by the craft of bending glass tubing into shapes. Similar devices filled with other noble gases can produce different colors.

Figure 1-1-6 Neon sign

7. **Laser:** A laser is a device that emits light (electromagnetic radiation) through a process called stimulated emission. The term "laser" is an acronym for Light Amplification by Stimulated Emission of Radiation. The first working laser was demonstrated on 1960 by Theodore Maiman. Laser light becomes an important illumination source for current commercial devices due to it is usually spatially coherent and has a narrow wavelength spectrum. Common applications of lasers are optical storage devices, fiber-optic communication, laser printers and laser pointers.

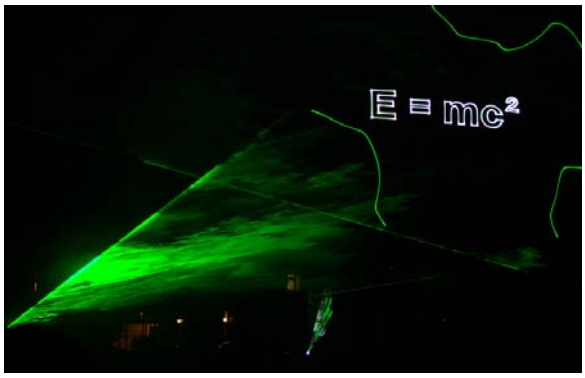

Figure 1-1-7 Laser projection

8. **LED (Light Emitting Diode):** It is a semiconductor diode that emits light when an electric current is applied in the forward direction of the device. The effect is a form of electroluminescence where incoherent and narrow-spectrum light is emitted from the p-n junction in a solid state material. LEDs are widely used as indicator lights on electronic devices and increasingly in higher power applications such as flashlights and area lighting. It has advantages in high efficiency, long lifetime, and rigid structure; which compared with traditional lamps. The color of the emitted light depends on the composition and condition of the semiconducting material used, and can be infrared, visible, or ultraviolet.

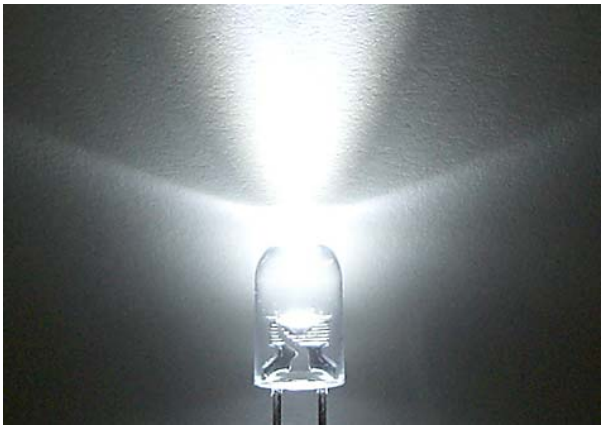

Figure 1-1-8 LED lamp

For summary, we list the development history of artificial sources in table 1-1-1.

Table 1-1-1 Development history of artificial sources

Years	Sources
Long time ago	Human began to use fire
Paleolithic period	Torch was found
B.C 3000	Egyptians and Cretans made the candle
577	Chinese invented match
800	First kerosene lamp was found at Baghdad
1879	T. A. Edison improved the tungsten incandescent lamp
1910	G. Claude made first neon lamp
1934	G. E. Inman built a prototype fluorescent lamp
1960	T. Maiman demonstrated the first working laser
1962	N. Holonyak Jr. developed the first practical visible-spectrum (red) LED

1-2 Classification of Approach to Illumination and More on Light Pipe

The illumination design is a scheme to control the behavior of light. We can adjust ray distribution by refraction, reflection, and scattering. The development of illumination until now can be concluded into three kinds of main forms.

1. **Abbe illumination**

Abbe illumination is a form of illumination where the source is imaged directly onto the object being viewed or projected. This requires a source of uniform intensity, such as an arc lamp. Abbe illumination has been used since the first projection systems in the 1600's. Its main drawback is that the uniformity of the source is "critical" to the uniformity of illumination of the object. So it is used when the source is sufficiently uniform for the system requirements.

2. **Köhler illumination**

Köhler illumination is a type of specimen illumination used in transmitted- or reflected-light microscopy. It was designed by August Köhler in 1893, and overcame limitations of previous types of sample illumination techniques (i.e., critical illumination) [1-2]. Prior to the advent of Köhler illumination, the filament of the bulb used to illuminate the sample could be visible in the sample plane. This created what is known as a filament image. Köhler illumination overcomes these limitations by utilizing a collector lens in front of the light source. This lens focuses the light at the condenser diaphragm, and this has the effect of putting the condenser diaphram and the filament image in conjugate planes. Thus, the filament image is no longer conjugate to the image plane, and is no longer visible.

3. **Rantsch Illumination**

In Rantsch illumination, the light passes through a condenser that images the source

into a relay lens. This relay lens images the condenser onto the object to be viewed/projected. In the vicinity of the object, there is a field lens that images the relay lens onto the objective/projection lens.

1-3 More on Light Guide and its Unique Application to Ultra-Thin Display

In recent years, information technology (IT) has brought great influence and impacts to human life. Among various IT products, display is one of the key devices. Although the technologies of display, such as plasma display and liquid-crystal display, are sufficiently mature, progressive improvements on the methods of wide viewing-angle and thin thickness are achieved where rear-projection displays have appealing advantages in screen appearance for human sense. Rear projection technique can be utilized to produce a display with a larger size and ultra-thin thickness. Although many progresses have been accomplished technically, there remain many challenges in developing ultra-thin display. Currently, rear-projection display could be realized with a ratio of projector's thickness and screen's diagonal length ~1:10 [1-3]. Nevertheless, this implementation requires an elaborate design of projection lenses [1-4] and a very unique hybrid (asymmetrical) Fresnel lens [1-5]. Theoretically, the analysis is difficult because common paraxial optics is generally not applicable. Hence, workable schemes actually demanded more fundamental understandings.

On the other hand, by utilizing a single, thin wedge-shaped sheet of glass or acryl, the injected rays from the thick end of the wedge will be guided to the top side, i.e., screen [1-6] ~ [1-9]. Wedge-plate display is the projection technique which includes an optical projection engine and a thin plate with a slope, utilizing the total internal reflection (TIR) of ray inside it, to guide image on the screen. The structure of wedge plate is a thin transparent sheet, and the bottom surface of this sheet has a slope, while the upper surface (output) is tilted by a small angle, so the meridional section of this sheet has a wedge shape, and typically the vertex angle of wedge is small than 5°.

The most attractive advantage of wedge-plate display is the thickness, which greatly improves the size of rear-projection display. Typically the thickness (the thick end of wedge plate) is less than 3 inches, while the width of a commercial 42-inch liquid crystal display (LCD) or plasma display panel (PDP) is about 4 to 10 inches. The ratio between the projector (plate) thickness and screen diagonal length can be rather large. Besides, due to the ray in wedge-plate display is injected by front projection and emerged by rear projection; wedge-plate display also has an advantage on high resolution as that of the projection TV. The critical issue for the industrialization of wedge-plate display is on the fabrication of wedge plate, since the optical engine has been an available technique as that in front or in rear projection displays. For examples, as the screen size of wedge-plate display is getting large, a special procedure to prevent the heat deformation when polishing acrylic is required. Meanwhile, to control of the cooling rate of acrylic liquid precisely when using modeling method to get an accurate shape of wedge plate is also necessary.

1-4 Patent Survey on Light Pipe and Light Guide

Light pipes and light guides provide the capability to collect or transport energy, changing propagation direction, and redistributing the profile of light beams, with high efficiency. Light pipes and light guides are widely used in current electro-optical systems, such as optical engines for projectors [1-10], backlight systems for liquid crystal panels [1-11], and some computer devices like the optical mouse [1-12] and power indicators for disk drives [1-13]. Some information devices are also illuminated through light pipes, such as automotive dashboards [1-14] and cell phone keyboards. Hence, the light pipe and light guide have become key elements in a variety of illumination and display systems and devices. It is important to design and manufacture light pipes and light guides with high transmittance and low energy losses.

The applications of light pipe and light guide may appear in more than one hundred years. Following we list several typical patents for light pipe and light guide.

(1): ***Light pipe having optimized cross-section*** [1-15]. This patent was applied on 1994 and the inventor is Steven G. Saxe (3M). The inventor proposed a serial of light pipes with different cross-section. The cross-sections of these light pipes were well designed so that it can guide rays into desire directions and distributions.

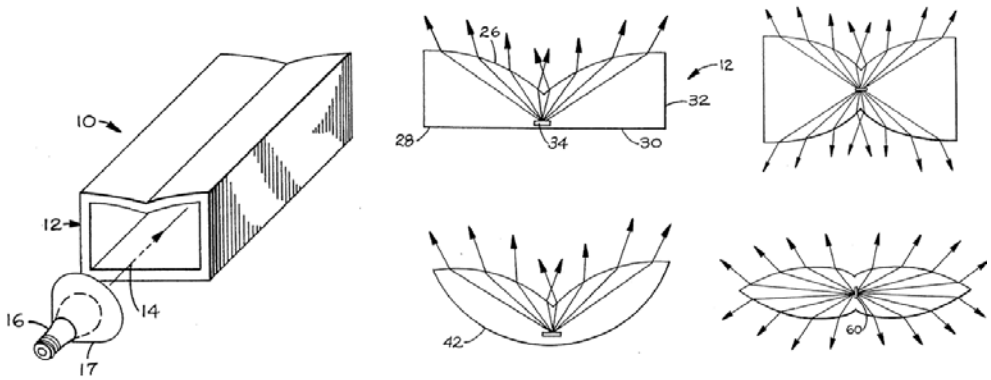

Figure 1-4-1 LED lamp

(2): ***Illumination engine for a projection display using a tapered light pipe*** [1-10]. This patent was applied on 1994 and the inventor is Kenneth K. Li (Wavien). The inventor used a tapered light pipe to collect the flux of the discharge lamp. He also designed a dual-focus reflector in which the source is at the first focal point and the tapered light pipe stands at the other one. This tapered light pipe can not only collect light but also control the emitting angle of ray for an illumination engine of projection display.

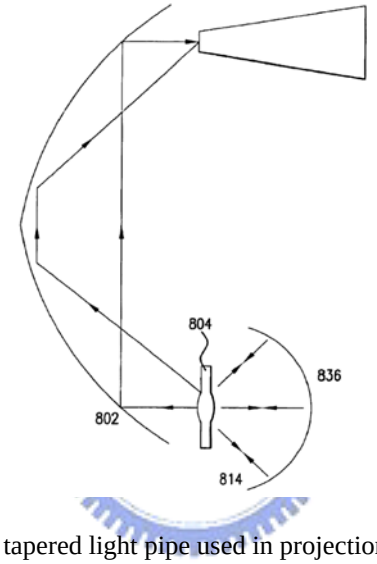

Figure 1-4-2 A tapered light pipe used in projection display engine.

(3): ***Dental Light Guide*** [1-16]. This patent was applied on 2008 and the inventors are Hohn West and Scott Ganaja (Den-Mat Holdings). This patent is in fact a light pipe design. The inventors design a light pipe to transmit and distribute light from light source (LED) to the tooth surface. The inventors also improve the entrance area of light pipe so that it can provide more collecting efficiency.

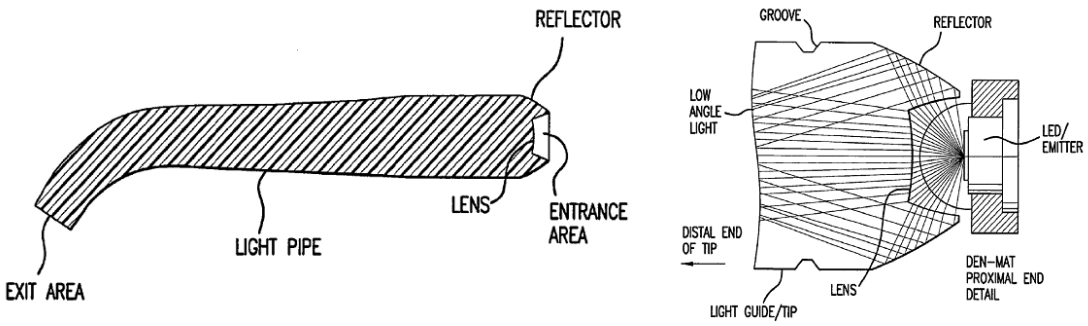

Figure 1-4-3 A dental light pipe

(4): ***Keypad Light Guide*** [1-17]. This patent was applied on 2008 and the inventors are T.-M. Hsu and W.-F. Cheng (Sutech Trdaing). The inventors design a compact light guide to illuminate the keyboard of cell phone or other portable devices. This light guide can provide uniform illumination for the keypad and only one LED source is need. It provides the portable devices consuming little power.

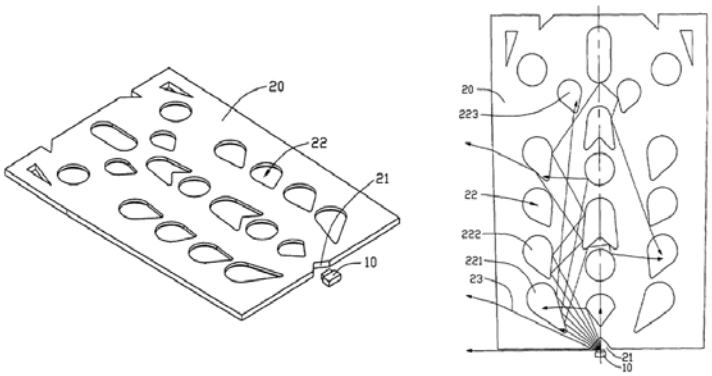

Figure 1-4-4 A compact light guide used for keypad

1-5 Study Concerns and Dissertation Organization

In recent ten years, there are many designs and analyses related to light pipes and light guides in the published literatures. Hawthorn examined the transmittance of skew rays in the infrared region, through metal light pipes with ray tracing [1-36]. Gupta et al. developed a concept of principle section to design the most efficient light pipe geometries [1-35]. Chien and Shieh designed an integrated polarized light guide [1-34]. Siitonen et al. did the LED coupling in to light guides [1-28] [1-33]. Derlofske et al. developed a flux confinement diagram (FCD) model to discuss the flux propagation of square light pipes and angular distribution [1-32]. Yang et al. also proposed a polarized light guide [1-31]. Chu and Chern demonstrated no-loss light pipes [1-30]. For reference, we made a list of the relevant literature of light pipes and light guides, which is shown in table 1-5-1 [1-18] ~ [1-36].

Table 1-5-1 List of publications regarding light pipe and light guide

Year	Authors / Source	Characteristics	Light pipe	Light guide
2008	P. Huang et. al., OL [1-18]	Design		Y
2008	F. Fournier et. al., OL [1-19]	Design	Y	
2008	F. Fournier and R. Jannick, AO [1-20]	Design	Y	
2008	C. Chen et. al., AO [1-21]	Design		Y
2008	C. Cheng and J. Chern, JOSA A [1-22]	Analysis	Y	
2007	J. Lee et. al., OL [1-23]	Design		Y
2007	Y. Ye et. al., AO [1-24]	Analysis		Y
2007	S. Park et. al., OExp [1-25]	Design		Y
2007	Y. Cheng et. al., JOSA A [1-26]	Analysis	Y	
2006	C. Cheng and J. Chern, JOSA A [1-27]	Analysis	Y	
2006	S. Siitonen et. al., AO [1-28]	Efficiency		Y
2006	Y. Cheng and J. Chern, JOSA A [1-29]	Analysis	Y	
2005	S. Chu and J. Chern, OL [1-30]	Analysis	Y	
2005	X. Yang et. al., OExp [1-31]	Design		Y
2004	J. F. V. Derlofske and T. A. Hough, OE [1-32]	Flux Analysis	Y	
2004	S. Siitonen et. al., AO [1-33]	Efficiency		Y
2004	K. Chien and H. D. Shieh, AO [1-34]	Design		Y

2001	A. Gupta et. al., AO [1-35]	Analysis	Y	
1999	D. G. Hawthorn and T. Timusk, AO [1-36]	Transmittance	Y	

In Table 1-5-1 we can find that most research works was published in previous five year and this shows that the studies of light pipes and light guides are current trend.

Light pipes and light guides are devices that can guide rays to a specific place. Generally, light pipe is a self-contained optical device that traps and guides light with no consideration of information propagation from the input to the output aperture, while the light guide could carry information content. Therefore, devices with abilities to carry and propagate light can be referred to a generalized light pipe or light guide, such as different shape of light tubes, the optical fibers, a plastic slab in back light system, and the wedge plate in an ultra-thin display, which is one of the concern of study.

In this dissertation, we would like to put emphasis on the discussions of the transmissive property of different shape of light pipes, the polarization behavior when ray propagates in light pipe, and the image behavior of light guide applied on an ultra-thin display. The dissertation is organized as the following. In chapter 2, we list and summarize the basic terms for light pipes and light guides. In chapter 3, we investigate the irradiance formation of different shapes of straight light pipes. We try to give a quantitative discussion of the uniformity on different light pipe geometries. In chapter 4, we propose new light pipe application on polarization-preserving angular shifter. We show these two new light pipes can preserve the polarization and deflect the output ray angle as we desired. In chapter 5, we discuss the aberration characteristics of a wedge-plate display optical system and provide two methods to reduce dark zone. We also propose a new type of circular display base on the wedge-plat display. Finally are the conclusions and future works.

References

[1-1] Wikipedia, http://en.wikipedia.org, key word= light source.

[1-2] A. Köhler, " Lighting system for cinematographs," US Patent # 1143287 (1915).

[1-3] S. Shikama, H. Suzuki, and K. Teramoto, “Optical system of ultra-thin rear-projector equipped with refractive-reflective projection optics,” SID Symposium Digest **33**, 1250-1253 (2002).

[1-4] H. Suzuki, K. Teramoto, J. Suzuki, and S. Shikama, “Image display device and adjustment for alignment,” US Patent #6631994 (2003).

[1-5] H. Suzuki, K. Teramoto, Y. Ashizaki, S. Sikama, H. Sekiguchi, T. Ryuugou, and K. Kojima, “Fresnel lens, screen, image displaying device, lens forming mold manufacturing method and lens manufacturing method,” US Patent #7116746 (2006).

[1-6] A. Travis, T. Large, and M. Buckingham, "Image quality in flat projection wedges," SID Symposium Digest **35**, 850–853 (2004).

[1-7] A. Travis, J. Moore, and J. Zhong, "Optical design of a flat panel projection wedge display," SID Symposium Digest **33**, 461–464 (2002).

[1-8] J. T. Veligdan, "Thin display optical projector," US Patent # 6002826 (1999).

[1-9] A. Travis and J. Zhong, "Linearity in flat panel wedge project," SID Symposium Digest **34**, 716–719 (2003).

[1-10] K. K. Li, “Illumination engine for a projection display using a tapered light pipe,” U.S. Patent #6739726 (2005).

[1-11] N. Takahashi and S. Umemoto, "Liquid crystal display apparatus having light pipe with reflective polarizer,” U.S. Patent #6778235 (2004).

[1-12] E. Nestler, "Light pipe for an optical mouse,” U.S. Patent #4716287 (1987).

[1-13] S. Staley and S. W. Stout, "Eject button for disk drive with light pipe", U.S.

Patent #6717769 (2004)

[1-14] J. Lee and J. E. Greivenkamp, "Modeling of automotive interior illumination systems," Opt. Eng. **43(7)** 1537–1544 (2004).

[1-15] S. G. Saxe, "Light pipe having optimized cross-section," U.S. Patent #5309544 (1994).

[1-16] J. West and S. Ganaja, “Dental Light guide, "U.S. Patent #7410283 (2008).

[1-17] T.-M. Hsu and W.-F. Cheng, “Keypad Light Guide, " U.S. Patent #7407314 (2008).

[1-18] P.-H. Huang, T. -C. Huang, Y. -T. Sun, and S. -Y. Yang, "Large-area and thin light guide plates fabricated using UV-based imprinting", Opt. Exp. **16**, 15033-15038 (2008).

[1-19] F. Fournier, W. J Cassarly, and J. P Rolland, "Method to improve spatial uniformity with lightpipes", Opt. Lett., **33**, 1165-1167 (2008).

[1-20] F. Fournier and J. P Rolland, "Optimization of freeform lightpipes for light-emitting-diode projectors", Appl. Opt. **47**, 957-966 (2008).

[1-21] C. -F. Chen, H. -T. Wang, and C. -H. Chen, “High throughput reflective light guide for planar illuminator”, Appl. Opt. **47**, 784-791 (2008).

[1-22] C. -M Cheng and J. -L. Chern, "Illuminance formation and color difference of mixed-color light emitting diodes in a rectangular light pipe: an analytical approach", Appl. Opt. **47**, 431-441 (2008).

[1-23] J. -H. Lee, H. -S. Lee, B. -K. Lee, W. -S. Choi, H. -Y. Choi, and J. -B. Yoon, "Simple liquid crystal display backlight unit comprising only a single-sheet micropatterned polydimethylsiloxane (PDMS) light-guide plate", Opt. Lett, **32**, pp.2665-2667 (2007).

[1-24] Y. Ye, D. Pu, Y. Zhou, L. Chen, "Diffraction characteristics of a submicrometer

grating for a light guide plate", Appl. Opt. **46**, 3396-3399 (2007).

[1-25] S. -R. Park, O. -J. Kwon, D. Shin, S. -H. Song, H. -S Lee, and H. -Y. Choi, "Grating micro-dot patterned light guide plates for LED backlights", Opt. Exp., **15**, 2888-2899 (2007).

[1-26] Y. -K. Cheng, M. -H. Wang, and J. -L. Chern, "Irradiance formations of on-axis Lambertian pointlike sources in polygonal total-internal-reflection straight light pipes", J. Opt. Soc. Am. A **24**, 2748-2757 (2007).

[1-27] C. -M Cheng and J. -L. Chern, "Optical transfer functions for specific-shaped apertures generated by illumination with a rectangular light pipe", J. Opt. Soc. Am. A **23**, 3123-3132 (2006).

[1-28] S. Siitonen, P. Laakkonen, P. Vahimaa, M. Kuittinen, and N. Tossavainen, "White LED light coupling into light guides with diffraction gratings," Appl. Opt. **45**, 2623-2630 (2006).

[1-29] Y. -K. Cheng and J. -L. Chern, "Irradiance formations in hollow straight light pipes with square and circular shapes," J. Opt. Soc. Am. A **23**, 427-434 (2006).

[1-30] S. -C. Chu and J. -L. Chern, "No-loss bent light pipe with an equiangular spiral," Opt. Lett. 30, 3006-3008 (2005).

[1-31] X. Yang, Y. Yan, and G. Jin, "Polarized light-guide plate for liquid crystal display," Opt. Express **13**, 8349-8356 (2005).

[1-32] J. F. V. Derlofske and T. A. Hough, "Analytical model of flux propagation in light-pipe systems," Opt. Eng. **43(7)** 1503–1510 (2004).

[1-33] S. Siitonen, P. Laakkonen, P. Vahimaa, K. Jefimovs, M. Kuittinen, M. Parikka, K. Mönkkönen, and A. Orpana, "Coupling of Light from an LED into a Thin Light Guide by Diffractive Gratings," Appl. Opt. **43**, 5631-5636 (2004)

[1-34] K. -W. Chien and H. -P. D. Shieh, "Design and Fabrication of an Integrated Polarized Light Guide for Liquid-Crystal-Display Illumination," Appl. Opt. **43**,

1830-1834 (2004)

[1-35] A. Gupta, J. Lee, and R. J. Koshel, "Design of efficient lightpipes for illumination by an analytical approach," Appl. Opt. **40**, 3640-3648 (2001).

[1-36] D. G. Hawthorn and T. Timusk, "Transmittance of skew rays through metal light pipes," Appl. Opt. **36**, 2787-2794 (1999).

Chapter 2

Term Summary and Simulation Tool

2-1 Concerns and Terms of Light Pipe Illumination

In this section, we will introduce the important definitions and terms used in light pipe analysis and design. For the illumination applications, the primary concept is radiometry and photometry. In optics, **radiometry** is the field that studies the measurement of electromagnetic radiation, including visible light. Following lists the important physical quantities for radiometry [2-1] [2-2].

1. **Energy:** it is the energy of electromagnetic waves. The quantity of radiant energy may be calculated by integrating flux (or power) with respect to time and, like all forms of energy, and its SI unit is the joule. The term is used particularly when radiation is emitted by a source into the surrounding environment. Radiant energy may be visible or invisible to the human eye.

2. **Flux:** In radiometry, flux or power is the measure of the total power of electromagnetic radiation (including infrared, ultraviolet, and visible light). The power may be the total emitted from a source, or the total landing on a particular surface. The SI unit of radiant flux is the watt (W), which has dimensions of energy/time or, in SI unit is joules/second.

3. **Intensity:** intensity is defined as power per unit solid angle. The SI unit of radiant intensity is watts per steradian ($W \cdot sr^{-1}$). Intensity is distinct from irradiance, which are often called intensity in branches of physics other than radiometry.

4. **Irradiance:** irradiance is radiometry terms for the power of electromagnetic radiation at a surface, per unit area. Irradiance is used when the electromagnetic

radiation is incident on the surface. The SI units for irradiance is watts per square meter ($W \cdot m^{-2}$).

5. **Radiance**: Radiance is radiometric measures that describe the amount of light that passes through or is emitted from a particular area, and falls within a given solid angle in a specified direction. They are used to characterize both emission from diffuse sources and reflection from diffuse surfaces. The SI unit of radiance is watts per steradian per square meter ($W \cdot sr^{-1} \cdot m^{-2}$).

Photometry is the science of measurement of light, in terms of its perceived brightness to the human eye. It is distinct from radiometry, which is the science of measurement of radiant energy (including light) in terms of absolute power; rather, in photometry, the radiant power at each wavelength is weighted by a luminosity function that models human brightness sensitivity. Typically, this weighting function is called the photonic sensitivity function, and Fig. 2-1-1 shows the function.

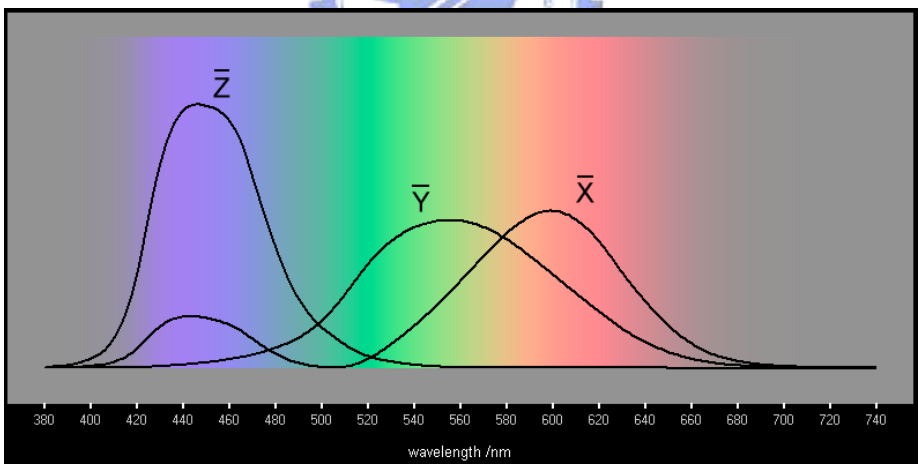

Figure 2-1-1 The photonic sensitivity function

Photometry has the same physical quantities as that in radiometry, but in different unit. Table 2-1-1 lists definitions and corresponding units for each physical quantity of radiometry and photometry.

Table 2-1-1 Comparison of radiometry and photometry

Quantities	Definition	Unit in Radiometry	Unit in Photometry
Energy	Energy	joule	joule
Flux	Energy per unit time	joule/s, watt	lumen
Intensity	Flux per solid angle	watt/sr	lumen/sr, cd
Irradiance	Flux per unit area	watt/m^2	lumen/m^2, lux
Radiance	Flux per solid angle per unit area	watt/sr/m^2	cd/m^2

2-2 Concerns and Terms of Ultra-Thin Display

In display system, the most important terms which will affect image quality are aberration and contrast ratio. Following we will introduce these decisive terms.

Aberration

Aberrations are departures of the performance of an optical system from the predictions of paraxial optics. Aberration leads to blurring of the image produced by an image-forming optical system. It occurs when light from one point of an object after transmission through the system does not converge into a single point. In 1850, Seidel investigated and codified the primary aberrations and delivered analytical expressions for their determination. For this reason, the primary image defects are usually referred to as the Seidel aberrations. Following are the Seidel aberrations [2-1] [2-3].

1. **Spherical aberration:** spherical aberration is the variation of focus when ray pass through different height of lens aperture. For an on-axis object, there will be only spherical aberration and it can be reduced by decrease the lens aperture.

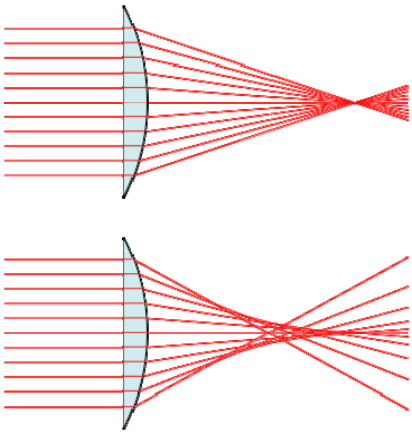

Figure 2-2-1 The spherical aberration

2. **Coma:** coma is the variation in magnification of the oblique rays. Coma can be minimized by choosing the curvature of the lens surfaces to match the application. Lenses in which both spherical aberration and coma are minimized at a single

wavelength are called aplanatic lenses.

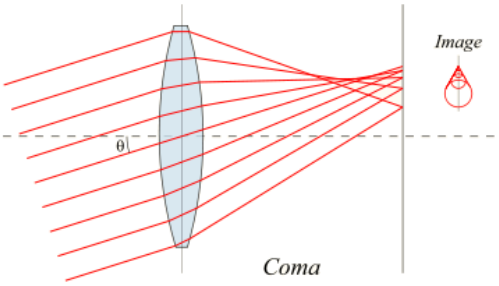

Figure 2-2-2 Coma

3. **Astigmatism:** astigmatism occurs when the tangential and sagittal images do not coincide. In the presence of astigmatism, the image of a point source is not a point, but takes the form of two separate lines as shown in Fig. 2-2-3. Between the astigmatic foci the image is an elliptical or circular blur.

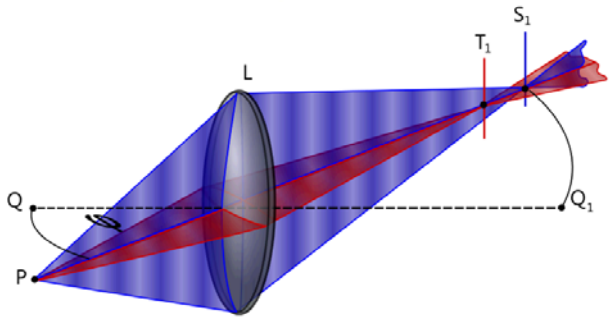

Figure 2-2-3 Astigmatism

4. **Field curvature:** when there is no astigmatism, the sagittal and tangential image surfaces will coincide with each other and lie on a curve surface. It is also called the Petzval surface. Utilizing a curved film, we can get a clearly image in each point of image surface

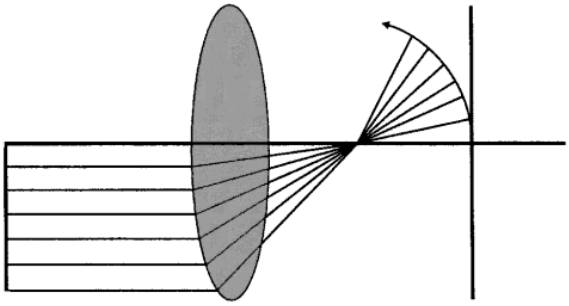

Figure 2-2-4 The field curvature

5. **Distortion:** distortion comes from the variation of magnification for different object height. Distortion usually increases as the cube of the image height, and it can be expressed as a percentage of the ideal image height.

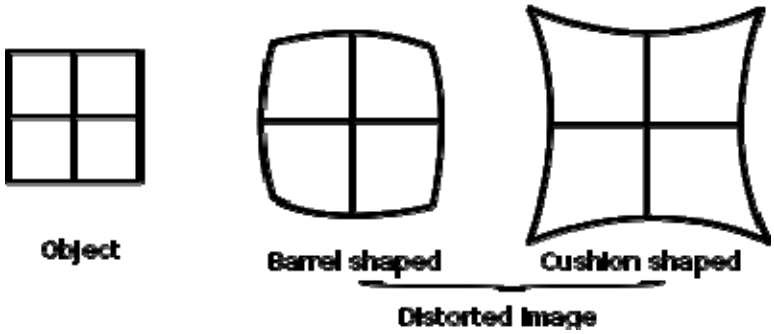

Figure 2-2-5 Distortion

Besides Seidel aberrations, there still be one aberration which affect the image quality of the display system, it is the chromatic aberration. **Chromatic aberration** is due to the index of refraction varies as a function of the wavelength of light, then the lens focus will also vary with wavelength. A cemented concave-convex lens pair can reduce chromatic aberration.

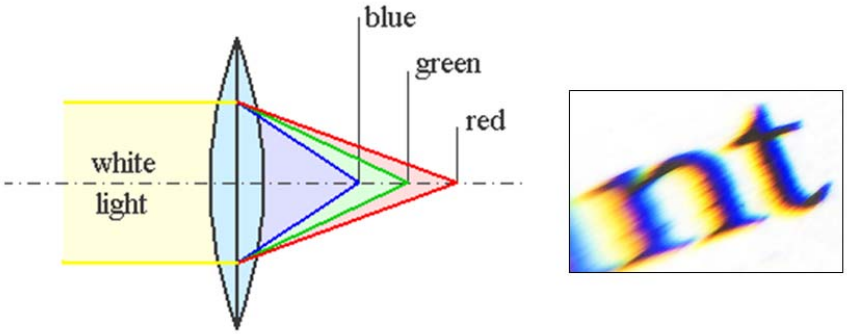

Figure 2-2-6 chromatic aberration

Contrast Ratio

The contrast ratio is a measure of a display system, defined as the ratio of the luminance of the brightest color (white) to that of the darkest color (black) that the system is capable of producing. A high contrast ratio is a desired aspect of any display, but with the various methods of measurement for a system or its part, remarkably different measured values can sometimes produce similar results.

ANSI contrast is the ratio between the average brightness of 8 alternating white rectangles and the average brightness of another 8 alternating black rectangles. The screen is divided into 4x4 rectangles, specified by ANSI (American National Standards Institute) [2-4]. It is also called "checkerboard" and is a more realistic way to test a projective display than full On/Off test.

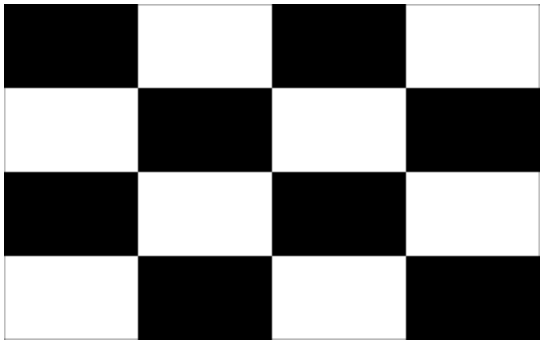

Figure 2-2-7 The ANSI contrast checkerboard

2-3 Survey of Simulation Tools

In this dissertation, we will investigate ray behavior for different kinds of light pipes and light guides by analytical method. To verify and explore our results, we used the simulation package, TracePro, which is available from the Lambda Research Corporation [2-5]. TracePro is commercial optical simulation software, and its calculation core is base on the Monte-Caro ray tracing. It can simulate the ray propagation in optical elements, and the optical properties are assigned to materials and surfaces in the model. Ray with flux and polarization state was defined when emitted, and the optical interactions include absorption, reflection and transmission, fluorescence and scattering will be executed accurately during the ray tracing. In the dielectric-air interface, ray will split according to the Fresnel equation [2-6], so TracePro can trace ray exactly for light pipe and light guide systems. The latest version of TracePro is version 4.1.8 (until December 2008).

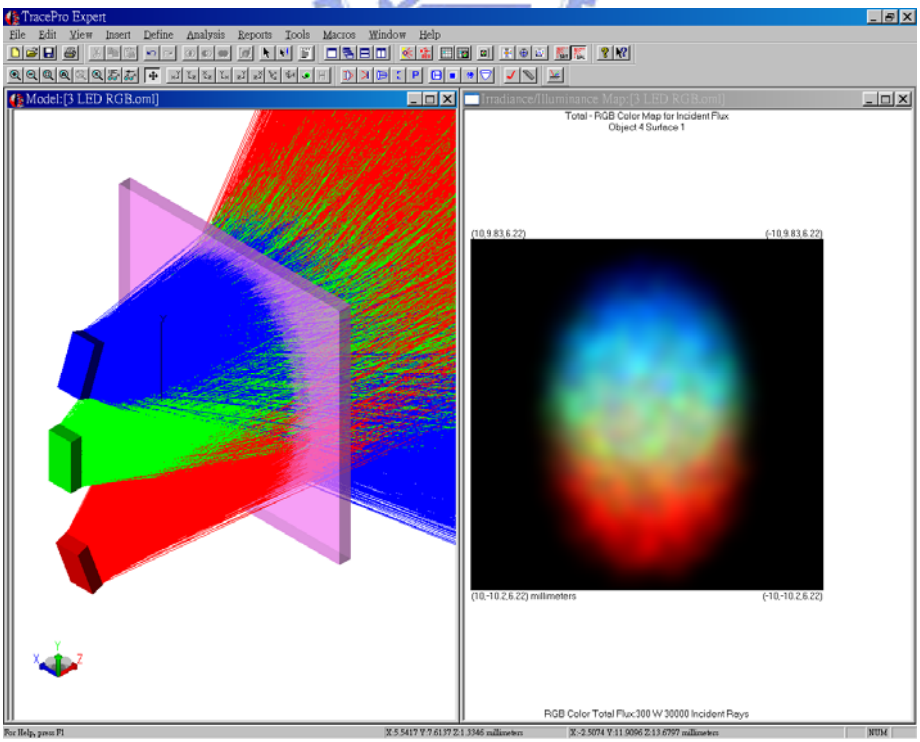

Figure 2-3-1 Operating window of TracePro

2-4 Summary of Key Setting in Simulation

In this dissertation, we use TracePro to verify our numerical analysis and investigate some real cases. Several common parameters and settings of ray tracing in TracePro are listed below.

(1): the point Lambertian sources are approximated by a small square emitting area, i.e., a 0.001mm*0.001mm region with Lambertian light emitting property, and typically 500,000 rays were traced to increase the sampling ratio. Each ray emitted from our point-like source carries the same flux, but the angular emitting probability will follow the Lambertian characteristics, $I(\theta) = \cos\theta$. The Lambertian point-like source will put near the light pipe or light guide input with a tiny distance (0.001mm).

(2): the selected material properties, such as Acrylic or BK7, are built in the electronic database of TracePro with refraction formula, so it can calculate the corresponding refractive index according to each input wavelength.

(3): the image plane will put just after the light pipe or light guide exit surface with a tiny distance (0.001mm). The sampling resolution of image plane will adjust for each case.

2-5 Conclusions

In this chapter, we list and summarize the important terms which will be identified in light pipe analysis/design or will affect the image quality of light guide display system. We also introduce the simulation tool, TracePro, and its key settings of source, material, and image plane. In the following chapters, we will go into the subjects of our study on light pipes and light guides.

Reference

[2-1] W. J. Smith, *Modern optical engineering*, 3rd ed. (McGraw-Hill, 2000).

[2-2] Wikipedia, http://en.wikipedia.org, key word= radiometry.

[2-3] Wikipedia, http://en.wikipedia.org, key word= aberration.

[2-4] More information on ANSI can be found at http://www.ansi.org.

[2-5] More information on TracePro can be found at http://www.lambdares.com.

[2-6] M. Born and E. Wolf, Principles of Optics, 7th ed.(Cambridge U. Press, 1999), pp. 42–43, 50–51.

Chapter 3

Irradiance Analysis of Light Pipes

3-1 Motivation

Light pipes are devices, which can guide rays to a specific place. Light pipes are widely used for illumination engines in projectors [3-1], as backlight systems for liquid crystal panels [3-2], in automobile dashboards [3-3] and in headlights [3-4], etc. Illumination systems and devices usually have irradiance or color uniformity requirements, so uniform spatial redistribution in an arbitrary light source is one of the most important properties of light pipe design. In the literature, articles discussing the properties of light pipes are available, but they are mostly focused on transmittance or flux analysis.

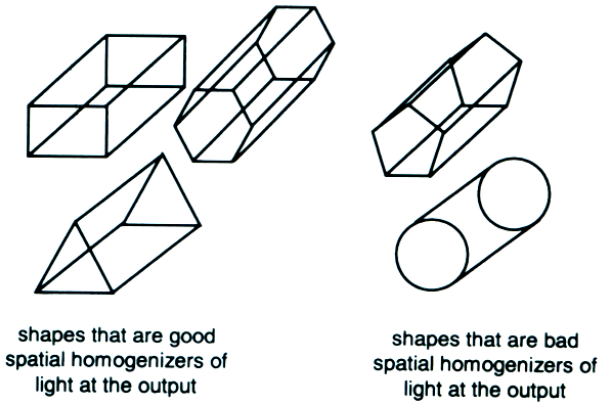

Figure 3-1-1 Irradiance properties of different shapes of light pipes

Refer to Fig. 3-1-1, Fischer and Tadic-Galeb indicated that triangle, rectangular and hexagonal shapes of light pipes are good special homogenizers, while circular and pentagonal are not [3-5]. On the same time, Gupta *et. al.* [3-6] also showed that a square light pipe has better spatial uniformity, and a circular light pipe there exists a hot spot at the center. The spatial uniformity of rectangular light pipe had been widely employed [3-1], but nearly no article has investigated the reason of its formation. An understanding of the mechanism of irradiance distribution would assist in the designs of light pipes for a variety of applications.

To explore the mechanism, the crucial factors that are involved in the irradiance distribution of light pipes should be clarified. Obviously, the emitting light source and the shape of the light pipe are two of them. The shape of the light pipe can modify the original characteristics of the spatial distribution of the source but not the angular distribution [3-7]. Square and circular light pipes have been considered in the literatures [3-5] [3-6]; although they are simple in outlook, they form the basic blocks for complex light pipe and are worthwhile to be explored further. On the other hand, there are various light sources in which a Lambertian source is of general interest. In this chapter we will investigate the formations of the irradiance distribution of different shapes of light pipes. We try to give a quantitative discussion of the uniformity of different light pipe shapes. The corresponding researches had also been published in academic papers [3-8] [3-9].

3-2 Irradiance Formation of Hollow Square Light Pipe

Flux Propagation in Two-Dimensional Light Pipes

First, the situation where light propagates in a two-dimensional light pipe with variations of length and width is discussed, as a basic building block of theoretical exploration. Consider a *hollow* straight light pipe with a length *L* and a width *D*, and, for simplification, the pipe wall has 100% reflection, as shown in Fig. 3-2-1(a).

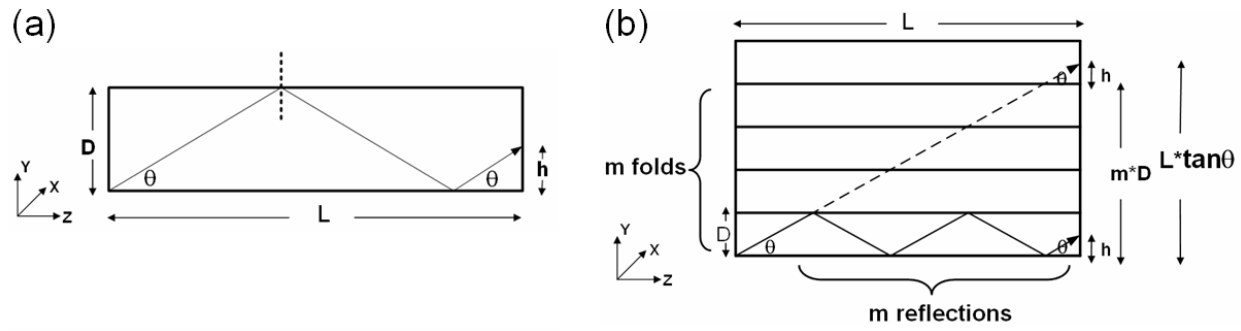

Figure 3-2-1 (a) Ray transported in a straight light pipe; (b) Ray transported in a folding light pipe.

When one ray with angle θ emitted from a point source incidents from the bottom of the light-pipe input, it will be reflected when it touches the pipe wall, and the angles between the ray path and the normal of reflective surface, before and after reflection, will be the same; finally this ray will exit the light pipe with the same angle θ at height *h* after reflecting *m* times. By taking the path of ray propagation as a straight line, as shown in Fig. 3-2-1(b), after *m* folds, where the ray goes forward a horizontal distance after each fold, the height *h*, where it finally reached the exit is given by

$$h(\theta) = k + (-1)^m (L\tan\theta - mD), \qquad (3\text{-}2\text{-}1)$$

where *k*=0 (*D*), if *m* is even (odd), and $m = Int[\frac{L\tan\theta}{D}]$ is the integer part of $\frac{L\tan\theta}{D}$ (e.g., $Int[\pi]$=3)**,** which corresponds to the reflection times inside the light pipe. From Eq. (3-2-1) we can see that the exit height of the ray in the light pipe *h* is interrelated to the incident angle θ. As a numerical example, we set *L*=10 and *D*=2; the functional graph of $h(\theta)$ is shown in Fig. 3-2-2(a). If there is a point source with Lambertian characteristics, the

intensity follows $I(\theta)=\cos\theta$. That means for one Lambertian ray propagates in θ direction, the flux collected from this ray in unit solid angle is $\cos\theta$, and the irradiance on unit pixel of detector contributed by this ray is also $\cos\theta$. According to Eq. (3-2-1), we can solve all θ_i for some particular h_0, i.e., $h_0 = k + (-1)^m (L\tan\theta_i - mD)$, here the subscript i denotes the available ith solution by counting the intersection points of $h(\theta)=h_0$ successively in Fig. 3-2-2(a). In other words, the irradiance at height h_0 of the exit port is

$$E(h_0)=\sum_{i=1}^{\infty}\cos\theta_i \,. \qquad (3\text{-}2\text{-}2)$$

Analytical derivation of irradiance *E(h)* for arbitrary height *h* is cumbersome; simple form is available only in some asymptotic cases, such as *L/D*>>1, and in that case, *E(h)* will approach to a constant irradiance distribution. By taking Eqs. (3-2-1) and (3-2-2), i.e., a semi-analytical approach, we turn to consider the cases that generally don't have simple analytical form, hereafter. The irradiance distribution *E(h)* of the case of *L*=10 and *D*=2 (*L/D*=5) is shown in Fig. 3-2-2 (b). We can see that the irradiance distribution of a Lambertian point source is uniform.

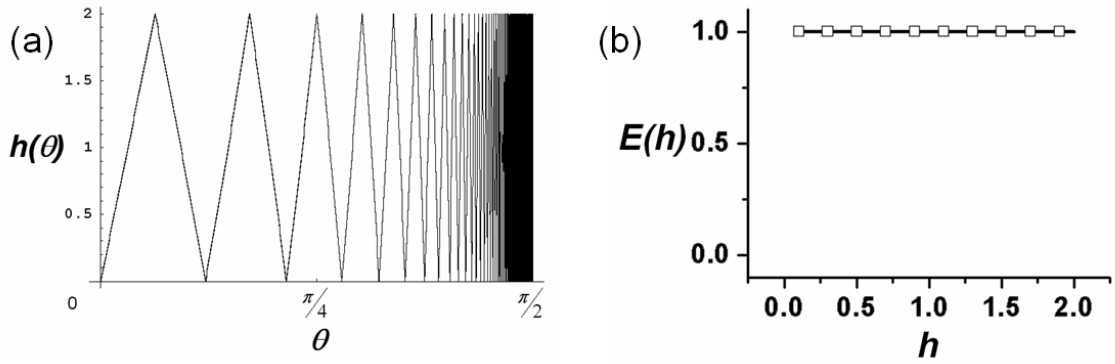

Figure 3-2-2 (a) Functional graph of Eq. (2-2-1); (b) Irradiance distribution of one-dimensional source at light pipe output.

When the incident position *P* has a vertical displacement *d* from the bottom, we can trace this ray back along its incident direction, as if it intersects the z-axis at point *P'* where *P'* has a horizontal distance $L'=\dfrac{d}{\tan\theta}$ to *P*, as shown in Fig. 3-2-3(a). It is clear that the ray

incidence from *P* would have the same behavior as the ray incidence from *P'*. In other words, for a non-zero incident height *d*, with a replacement of $L\tan\theta$ in Eq. (3-2-1) with $L\tan\theta+d$, we have

$$h(\theta,d)=k+(-1)^{m'}\left(L\tan\theta+d-m'D\right), \qquad (3\text{-}2\text{-}3)$$

where k=0 (*D*), if *m'* is even (odd), and $m'=Int[\frac{L\tan\theta+d}{D}]$.

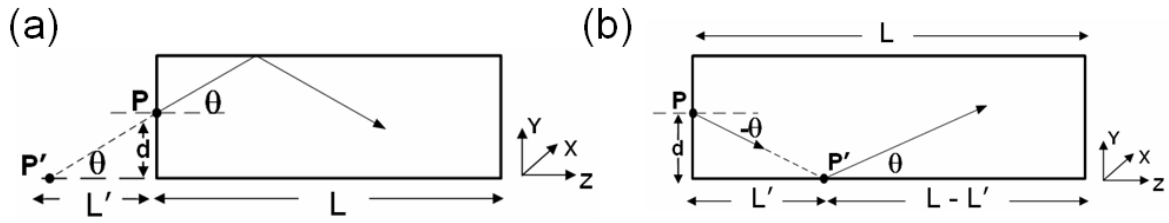

Figure 3-2-3 (a) Ray transported in a straight light pipe, when source position has a shift distance d; (b) Ray transported in a straight light pipe when the incident angle is negative

As a numerical example, again set L=10 and D=2; then d=0.5 and the irradiance distribution $E(h)$ can be seen in Fig. 3-2-4 which is denoted by a line with empty squares (note that the incident angle ranges from 0° to +90°, i.e., only a half of the angular distribution). By similar consideration, the incidence with a height *d* and angle $-\theta$ can be derived by replacing $L\tan\theta$ in Eq. (3-2-1) with $L\tan\theta$-*d*, as shown in Fig. 3-2-3(b). And we have

$$h(-\theta,d)=k+(-1)^{m''}\left(\,|L\tan\theta-d|\,-m''D\right), \qquad (3\text{-}2\text{-}4)$$

where k=0 (*D*), if *m"* is even (odd), and $m''=Int[\left|\frac{L\tan\theta-d}{D}\right|]$. The part with absolute value in Eq. (3-2-4) is to prevent a negative *h* when $L\tan\theta$ is small than *d*, i.e., ray transmits to output without reflection. Taking $d\to D-d$ into Eq. (3-2-3) and comparing to Eq. (3-2-4), one can find

$$h(-\theta,d)=D-h(\theta,D-d), \qquad (3\text{-}2\text{-}5)$$

and the total irradiance contribution is

$$E(h)_{full-angle}=E(h)_{+\theta}+E(h)_{-\theta}, \qquad (3\text{-}2\text{-}6)$$

where the subscripts $+\theta$ and $-\theta$ denote the emitting angles. The irradiance distribution for

an entire one-dimensional Lambertian point source is also shown in Fig. 3-2-4 which is denoted by the line with solid circles, by which we can see that the output irradiance distribution remains uniform for the whole region with the current setting, i.e., L=10, D=2 and d=0.5.

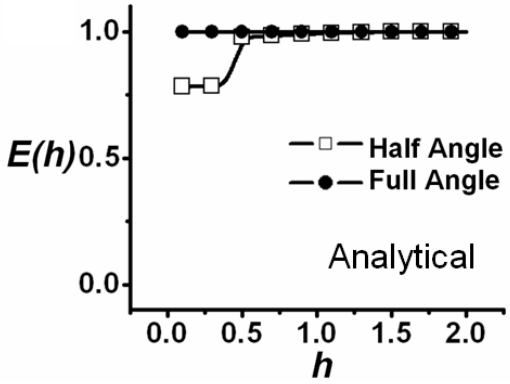

Figure 3-2-4 Irradiance distribution of two-dimensional half-angle and full-angle sources at light-pipe output when source position has a shift distance d

Extension to Three-Dimensional Case

Next we extend our discussion to a three-dimensional case. When the incident plane M of a one-dimensional point source (the degree of freedom is denoted by the angle θ) has an additional azimuth angle ϕ, the path of ray locations on the output plane will be a trapped path in a cross section of light pipe, as shown in Fig 3-2-5. The position function (P_x, P_y) of this trapped path is given by

$$\left[P_x(\theta,\phi), P_y(\theta,\phi)\right] = \left[h(\theta)\sin\phi, h(\theta)\cos\phi\right] \qquad (3\text{-}2\text{-}7)$$

It has infinite number of solutions of θ for every ϕ in specifying a position (P_{x_0}, P_{y_0}). After we scan the azimuth angle ϕ from 0 to 2π, the one-dimensional Lambertian point source becomes a two-dimensional one with parameters θ and ϕ. Gupta, Lee and Koshel used a principle section in simplifying the geometry of light pipe from three-dimensional to two-dimensional for analysis [3-6]. Here, however, we will pay more attention on irradiance

formation.

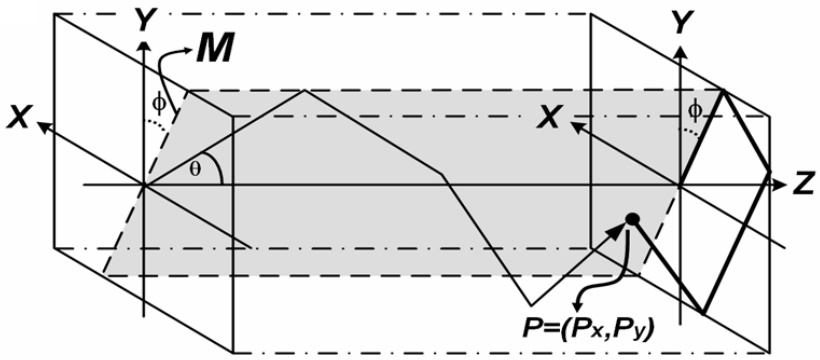

Figure 3-2-5 Schematic diagram of a two-dimensional Lambertian skew ray propagated in a square three-dimensional light pipe.

Due to the two components of Eq. (3-2-7) having the same ray-tracing characteristics of Eq. (3-2-1), one can expect there to also be a uniform irradiance distribution for the three-dimensional case. On the other hand, the ray emitting angles of the two components in the orthogonal coordinate will remain unchanged (or a change of sign) due to the direction of normal remains the same in any place of pipe wall. In other words, a square light pipe can modify a Lambertian point source into a uniform spatial distribution, while angular characteristics remain unchanged.

Simulation Verification

We used TracePro to verify the previous deduction. A hollow square light pipe with length *L* and width (or diameter) *D*, and the pipe wall reflectance set as 100%, was used. For the point source, we defined a grid source lying on the y-axis; each ray, emitted from the same point, but with a different angle θ, carried the flux $\cos\theta$. We selected each angular displacement as 0.01°; there were 9,001 rays for the half-angle source and 18,001 rays for the full-angle source. We then built a small square Lambertian point-like source as that described in section 2-4. The detector has 21x21 sampling pixels so that we can collect irradiance data from position *h=0* to *h=2*, each spaces of 0.1. Finally, we set the reflection

cut-off times to be 1,000 to prevent the computer from shutting down, because the perfect reflection of the pipe wall, and the number of rays reflected inside the light pipe, was a tangent function, which diverts at 90°.

As a case of two-dimensional space, we traced this Lambertian point-like source incidence to a square light pipe, which set L=10, D=2, and d=0.5, using TracePro. This result is shown in Fig. 3-2-6, which presented the same feature as that of semi-analytical derivation shown in Fig. 3-2-5.

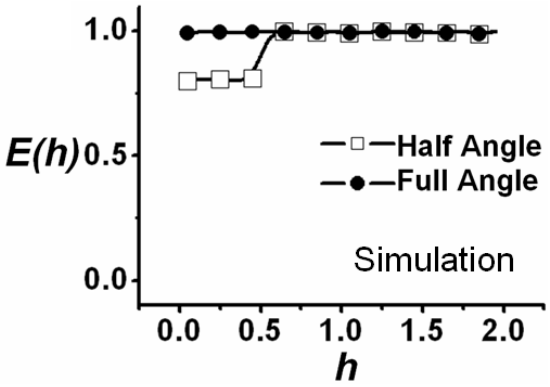

Figure 3-2-6 Simulation results of a one-dimensional source at light pipe output for half-angle and full-angle Lambertian sources.

Next, we discuss the case of three-dimensional space. We traced a Lambertian point-like source (note that the size is only 10^{-6} of the size of incident plane), which was initially placed at the center (P_x, P_y)=(1.0,1.0) of the light-pipe input, then moved the source horizontally to 0.25D, (P_x, P_y)=(0.5, 1.0) and traced it again. From Figs. 3-2-7(a) and 3-2-7 (b) we can see that, when the light from a point-like source is incident to a square light pipe, the irradiance distribution at the output had a uniform behavior. To identify the uniformity, we introduced the uniformity deviation defined by

$$\delta = \left[\frac{1}{n} \sum_{i=1}^{n} \left| E_i - \overline{E} \right| \right] \Big/ \overline{E}, \qquad (3\text{-}2\text{-}8)$$

where $\overline{E}$ stood for the average irradiance of n sampling points. We chose totally 441 (=21x21) sampling points, which were equally apart from each other located at the

observation plane, to calculate the uniformity deviation. The uniformity deviation values in Figs. 3-2-7(a) and 3-2-7(b) was tiny (1.783% and 1.767%, respectively), this agrees with our expectations laid out in previous discussion. To have a close look on the uniformity, the variation of irradiance at different pixels along the two lines of cross-section plots of Fig. 3-2-7(a), i.e., in the x- and y-directions is shown with an enlarged scale as shown in Fig. 3-2-7(c).

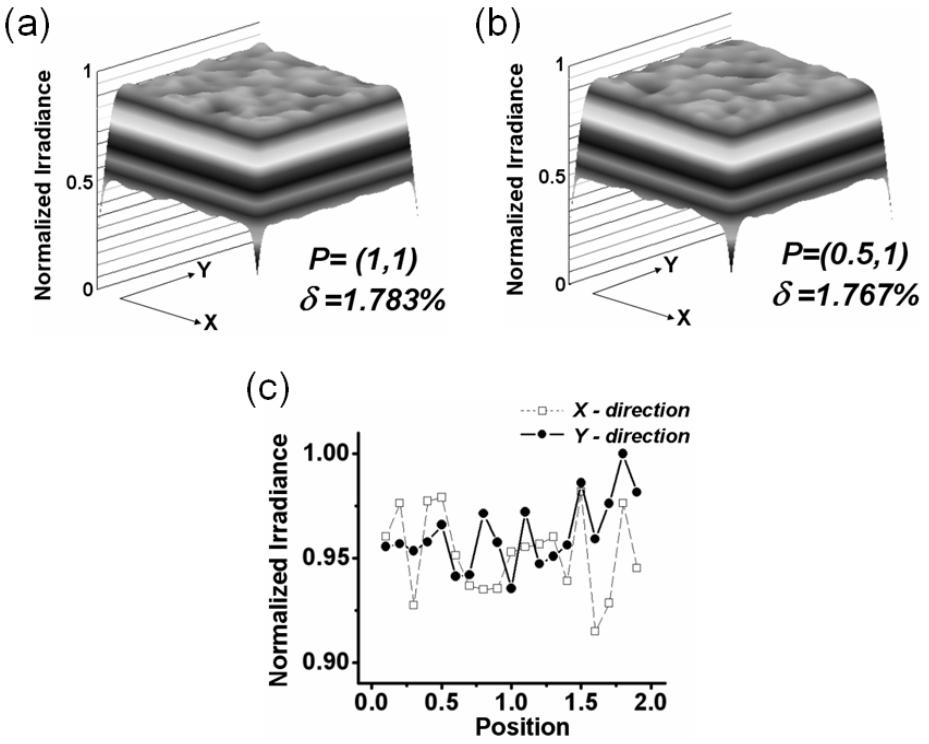

Figure 3-2-7 (a) and (b) Irradiance distribution of *L/D*=5 light pipes with sources in different incident positions (a) Source at input center; (b) Source has a horizontal shift; (c) cross-section plots in x and y directions of (a).

3-3 Irradiance Formation of Hollow Circular Light Pipe

Deduction for Circular Light Pipe

Now, we turn to investigate the case of circular light pipe. The circular light pipe has a diameter of cross section *D* and a length *L*. We consider a Lambertian point source, as in the case of three-dimensional square light pipe, in which the ray emitted along an incident plane *M'*, which has an angle ϕ related to the y-axis, as shown in Fig. 3-3-1. Because the normal vector of any point on the wall of circular light pipe is directed to the center and is orthogonal to the z-axis, every ray originating from the ϕ-angled cross-section of the source will propagate only along the plane *M'*, and the collection of ray locations on the exit plane will be a straight line.

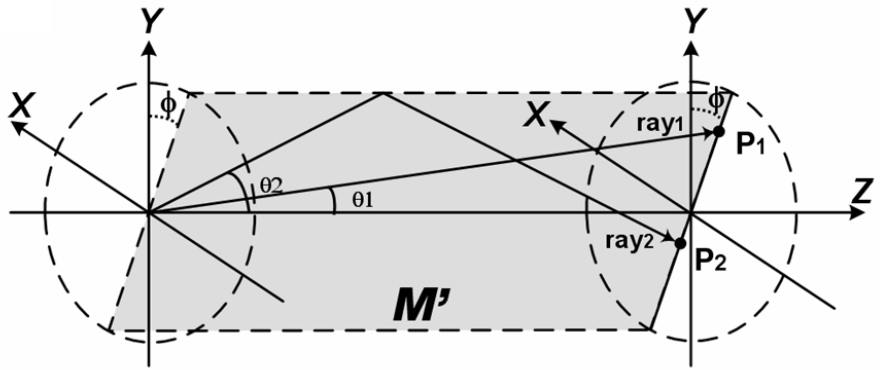

Figure 3-3-1 Schematic diagram of a two-dimensional Lambertian skew ray propagated in a circular three-dimensional light pipe.

Referring to Figs. 3-2-4 and 3-2-6, the irradiance along the straight line is uniform. In other word, every straight line, formed by a point source in two-dimensional space on the exit surface, has a uniform line distribution of irradiance. As long as the angle ϕ varies from 0 to 2π, now a point source located in a three-dimensional space is formed, as shown in Fig. 3-3-1. Referring to Fig. 3-3-2 which provides a schematic diagram of pixel distribution on the exit surface, we can imagine equally spaced sensor pixels over the straight line (ΔD is the size of a dot pixel of the sensor); hence, there are $N_d=D/\Delta D$ pixels. If we denote that the received flux is *F* for the straight-line area ($\sim D \times \Delta D$), then each dot pixel shares F/N_d. The

straight-line area was shone from a Lambertian point source with a cross section *M'* that had a ϕ angle now, with respect to the y-axis, and can be assumed to occupy a size $\Delta\phi$ angle. Hence, effectively, there are N_s source and $N_s = 2\pi/\Delta\phi$. Therefore, the irradiance at a point that has a distance *R* to the center, is as follows

$$
\begin{aligned}
E(R) &= \frac{Total\ \ flux\ of\ \ one\ circle}{Total\ \ area\ of\ \ one\ circle} \\
&= \frac{(\frac{F}{N_d})\cdot N_s}{\pi R^2 - \pi(R-\Delta D)^2} \\
&= \frac{\frac{F}{D/\Delta D}\cdot\frac{2\pi}{\Delta\phi}}{2\pi R\Delta D - \pi\Delta D^2} = (\frac{F}{D\Delta\phi}\cdot\frac{1}{R})(1-\frac{\Delta D}{2R})^{-1} \\
&\approx (\frac{F}{D\Delta\phi}\cdot\frac{1}{R})[1+\frac{\Delta D}{2R}-(\frac{\Delta D}{2R})^2+...].
\end{aligned}
\qquad \text{(3-3-1)}
$$

As a result, there is high location of irradiance concentrated at the center, decaying along the radial direction in proportion to $\frac{1}{R}$ approximately.

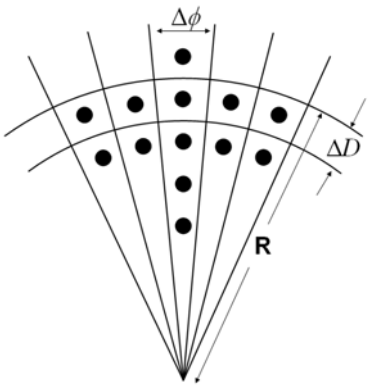

Figure 3-3-2 Schematic diagram of pixel density for circular light pipe.

Simulation Verification

Similar to the simulation analysis in section 3-2, we also traced for circular light pipe in which the Lambertian point-like source was placed at the center of the light pipe input (*R*=0). From Fig. 3-3-3(a) we can see that there was a hot spot in the light- pipe output. On the other hand, from Fig. 3-3-3 (b) we can see that the irradiance cross-section of the hot spot

had a symmetrical profile where a fitting curve was also provided. The profile had a peak value at the light-pipe center, with the irradiance decaying steadily along the radial direction in $\frac{1}{R}$, which is consistent with Eq. (3-3-1). A fitting curve of $E = a_1 R^{b_1}$ is used and the results of fitting is: a_1=0.02794 and b_1= -1.03216. The difference between the theoretical leading-order estimate and the simulation is ~3%. Inclusion of higher order theoretical estimate leads to a closer value to that of simulation.

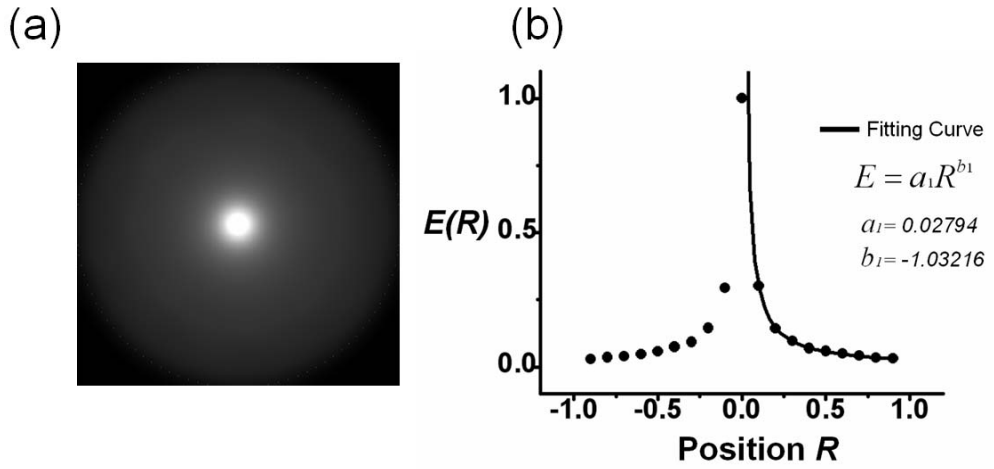

Figure 3-3-3 Simulation result of a circular light pipe: (a) hot-spot irradiance distribution of a circular light pipe, (b) cross-section profile.

Evolution from Circular to Square Light Pipe

It is known that a square light pipe has good spatial distribution, while a circular light pipe, in contrast, has hot-spot localization [3-6]. As shown above, a circular light pipe does, indeed, have energy localization. *Why does the localization vary with the shape of the light pipe?*

Unlike the case of a square light pipe, the pixel density argument cannot be used to deduce the result, because there is no straight line of uniform irradiance in most of the area. Nevertheless, to solve this issue, we modified the circular shape of light pipe to be flat, in an angle range of α at each quadrant, as shown in Fig. 3-3-4(a). The influence of the deformation α about the irradiance distribution on the exit surface can be identified. To identify the deformation of a circular light pipe, we introduced a deformation scale, defined by the root mean square of radius difference between the modified shape and a circular shape,

counted from all angles, i.e.,

$$\Delta = \frac{1}{2\pi}\sqrt{\int_0^{2\pi}(D_m(\theta) - R_s)^2 d\theta} \qquad (3\text{-}3\text{-}2)$$

where $D_m(\theta)$ is the length to the center of the deformed shape and R_s is the radius of the circular shape. Practically, the RMS circular difference may be defined by the root mean square of radius difference, between that of the modified shape and the circular shape, with each sampling taken by one degree. In Fig. 3-3-4(b) the variation of the peak value of the hot spot with deformation scale D_m is shown. As the deformation scale becomes large the localization gradually disappears. We applied an exponential curve to explore the trend of (normalized) central irradiance versus deformation scale, i.e., $E(_{R=0}) = a_2 e^{b_2 \Delta} + c_2$. It is found that a well-fit decay rate can be deduced, b_2~ -3.935.

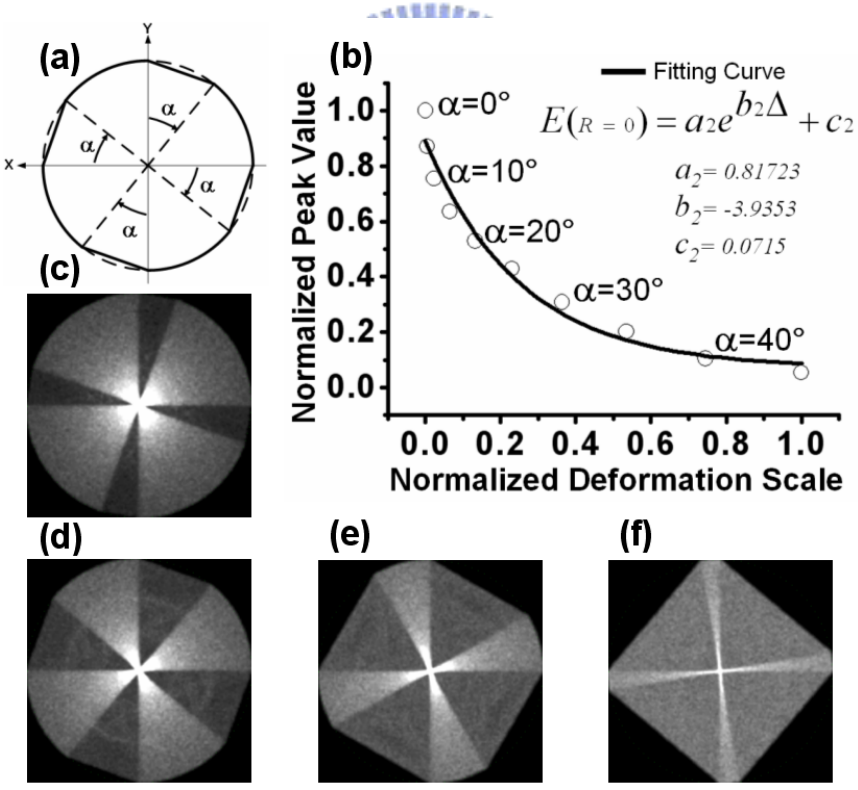

Figure 3-3-4 Simulation result for a modified-shape light pipe. (a) Schematic diagram of a modified-shape light pipe; (b) influence of the deformation scale on the hot-spot peak value; (c)–(f) distribution of light at the output port when α is (c) 10°, (d) 20°, (e) 30°, (f) 40°

In Fig. 3-3-4(c)-(f), a series of distribution plots at the exit facet of the modified-shape light

pipe is provided. One can see that the hot spot was gradually destroyed and the irradiance distribution became uniform, as α increased. It has been numerically verified that in current form of mixed-shape light pipe, the central peak value of irradiance is linearly decreasing with an increase of the angle α. In current form of mixed-shape light pipe, which is symmetrical respect to the center of light pipe, the amount of angle α is related to the area ratio of the linear portion (a manifestation of rectangular/square light pipe) and the circular portion (a manifestation of circular light pipe).

3-4 Irradiance Formations of Polygonal Total-Internal-Reflection Light Pipes

Three-Dimensional Dielectric-Filled Light Pipe

Figure 3-4-1 shows a two-dimensional straight light pipe filled with dielectric material, where the refractive index *n* can transmit rays via TIR, and all rays propagate in the same plane. When a ray propagates in air (n=1) and enters the light pipe at point *p*, the incident angle θ_i and the entrance angle θ_e satisfy Snell's law: $\sin\theta_i = n\sin\theta_e$. This ray encounters multi-reflections until it reaches the exit. The reflected angle on the pipe wall is $90° - \theta_e$. The number of reflections *m* depends on the light pipe width *D*, light pipe length *L*, and entrance angle θ_e, i.e.,

$$m = Int[\frac{L\tan\theta_e}{D}] \qquad (3\text{-}4\text{-}1)$$

where *Int* is the floor function. This function represents the integer part of the number inside the parenthesis (e.g., $Int[\pi]$=3). Snell's law indicates that the entrance angle θ_e is restricted from 0° to the critical angle θ_c, while the incident angle θ_i ranges from 0° to 90°. After *m* reflections, this ray exits the light pipe and contributes to the flux at the exit point. All rays emitted from the source contribute to the spatial distribution, or the irradiance distribution on the light pipe exit. Compare to the results in previous two sections, ray propagation behaviors in two-dimensional dielectric-filled straight light pipes and hollow straight light pipes are the same, except for the emission angular range of entrance angle. Therefore, the dielectric-filled light pipe should also exhibit a uniform irradiance distribution.

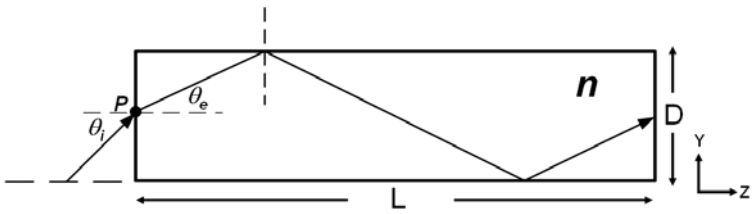

Figure 3-4-1 Schematic diagram of a ray transported in a dielectricfilled straight light pipe.

Three-Dimensional Case

In real three-dimensional cases of different light pipe geometric shapes, rays from the same source emit in different directions or propagate in different planes. After one ray touches the pipe wall, it may not continue in the same plane. Ray location distributions in a light pipe exit plane are complex, but can nevertheless be analyzed, as the following section shows. Specifically, ray analysis can be achieved by path projecting and mirror folding. Pentagonal and square light pipes serve as examples of each approach.

Path Projecting

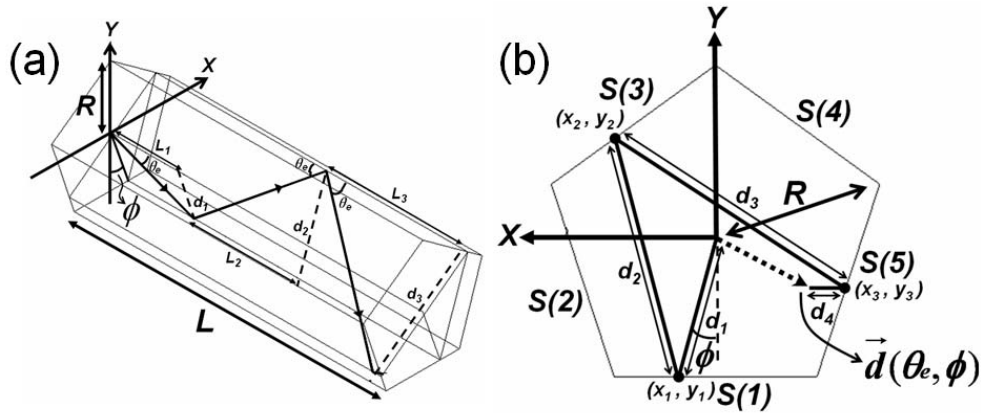

Figure 3-4-2 (a) Schematic diagram of a ray propagated in a pentagonal light pipe; (b) Ray path projection on the pentagonal light pipe exit surface.

According to Fig. 3-4-2(a), one ray emitted from the point source lying on the origin shines into a pentagonal light pipe, where θ_e is the entrance angle, ϕ is the angle between the projection of the incident ray on the entrance surface and the negative y-axis, L is the pipe length, and R is the pentagon circumradius. The entire three-dimensional source is composed of many two-dimensional sources, i.e., from $\phi=0^\circ$ to $\phi=360^\circ$. Figure 3-4-2(b) shows the ray propagation path projected on the light pipe output. Thus, a three-dimensional case can be treated as a two-dimensional case. The pentagon's symmetry allows discussion of only the emitting angular $0^\circ<\phi<36°$ instead of $0^\circ<\phi<360^\circ$. Figure 3-4-2(b) shows that if ϕ is selected, when θ_e increases, the ray distributes along a fixed path on the output surface where d is the projected length of the ray location path for some specific θ_e of light pipe

output, and $\vec{d}$ is the vector from the center to the exit position. According to Fig. 3-4-2(a), the value of *d* is

$$d(\theta_e) = \sum_{i=1}^{m+1} d_i(\theta_e) = \sum_{i=1}^{m+1} L_i \tan\theta_e \qquad (3\text{-}4\text{-}2)$$

where *m* is the number of reflections. Referring to Fig. 3-4-2(b), we can determine $\vec{d}$ by the following: if the ray entrance angle θ_e has the same emitting range (from 0 to $\theta_{e\max}$, where $\theta_{e\max}$ is the maximum of θ_e), when the angle ϕ increases, the ray reflection surface sequence changes.

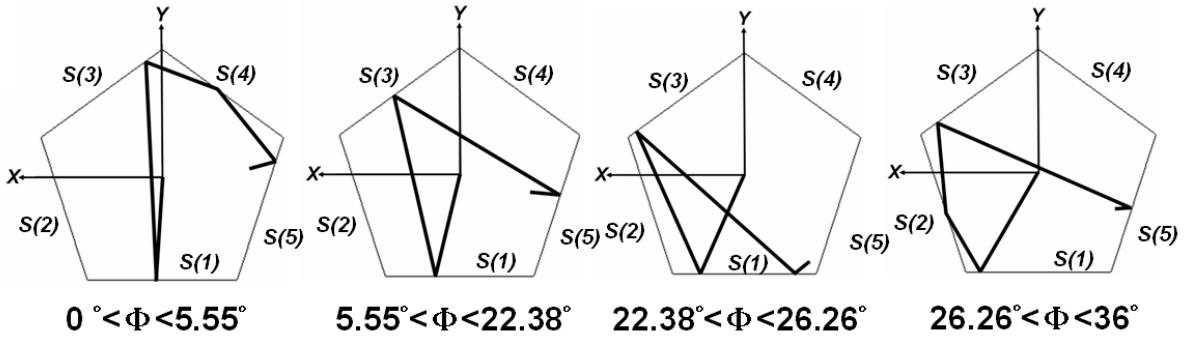

Figure 3-4-3 Four conditions of path projection method.

Figure 3-4-3 shows that the reflection surface sequence can be used to classify the projected exit location paths into four conditions, and further, derive the ray exit location vector $\vec{d}$. These four conditions were chosen by ray tracing, and a different range of ϕ angle lead to different reflection times and reflection surfaces. If the length *L* changes, the selected conditions of path projection method also change. A L/R ratio (L/R=10) serves as an example to demonstrate this method. Table 1 lists the results, where *S(i)* is the symbol of the i^{th} light pipe edge, (x_i, y_i) is the ray intersection point, and the i^{th} light pipe edge. The deductions in Table 3-4-1 produce a ray exit location vector $\vec{d}(\theta_e, \phi)$ on the light pipe exit surface for any θ_e and ϕ.

Table 3-4-1: Ray exit location deduction of pentagonal light pipe

Condition	Range/(No. of Reflections)	Vector Form
1:	$0 < d \leqslant d_1\,(0)$	$\vec{d}=(d\sin\phi,-d\cos\phi)$
$0^\circ < \phi < 5.5^\circ$,	$d_1 < d \leqslant d_1+d_2\,(1)$	$\vec{d}=(d\sin\phi,(d-2d_1)\cos\phi)$
$S(1)\rightarrow S(3)\rightarrow$	$d_1+d_2 < d \leqslant d_1+d_2+d_3\,(2)$	$\vec{d}=\begin{pmatrix}(d_1+d_2)\sin\phi-(d-d_1-d_2)\cos(18^\circ+\phi),\\(d_2-d_1)\cos\phi-(d-d_1-d_2)\sin(18^\circ+\phi)\end{pmatrix}$
$S(4)\rightarrow S(5)$	$d_1+d_2+d_3 < d \leqslant d_1+d_2+d_3+d_4\,(3)$	$\vec{d}=\begin{pmatrix}(d_1+d_2)\sin\phi-d_3\cos(18^\circ+\phi)-d_4\cos(54^\circ-\phi)+(d-d_1-d_2-d_3-d_4)\cos(18^\circ+\phi),\\(d_2-d_1)\cos\phi-d_3\sin(18^\circ+\phi)-d_4\sin(54^\circ-\phi)-(d-d_1-d_2-d_3-d_4)\sin(18^\circ+\phi)\end{pmatrix}$
	$d_1+d_2+d_3+d_4 < d\,(4)$	$\vec{d}=\begin{pmatrix}(d_1+d_2)\sin\phi-d_3\cos(18^\circ+\phi)-d_4\cos(54^\circ-\phi)+(d-d_1-d_2-d_3-d_4)\cos(18^\circ+\phi),\\(d_2-d_1)\cos\phi-d_3\sin(18^\circ+\phi)-d_4\sin(54^\circ-\phi)-(d-d_1-d_2-d_3-d_4)\sin(18^\circ+\phi)\end{pmatrix}$

where $d_1=\dfrac{R\cos 36^\circ}{\cos\phi}$, $d_2=\sqrt{(x_2-x_1)^2+(y_2-y_1)^2}$, $d_3=\sqrt{(x_3-x_2)^2+(y_3-y_2)^2}$, $d_4=\sqrt{(x_4-x_3)^2+(y_4-y_3)^2}$

$(x_1,y_1)=(R\cos 36^\circ\tan\phi,-R\cos 36^\circ)$, $(x_2,y_2)=\left(\dfrac{R(1+2\cos 36^\circ)}{\cot\phi+\tan 36^\circ},\ R-\tan 36^\circ\cdot x_2\right)$,

$(x_3,y_3)=\left(\dfrac{y_2-\tan(18^\circ+\phi)x_2-R}{\tan 36^\circ-\tan(18^\circ+\phi)},\ R+\tan 36^\circ x_3\right)$, $(x_4,y_4)=\begin{pmatrix}\dfrac{\tan(54^\circ-\phi)x_3-y_3-R(\cos 36^\circ+\sin 36^\circ\tan 72^\circ)}{\tan 72^\circ+\tan(54^\circ-\phi)},\\-\tan 72^\circ x_4-R(\cos 36^\circ+\sin 36^\circ\tan 72^\circ)\end{pmatrix}$

2:	$0 < d \leqslant d_1(0)$	$\vec{d}=(d\sin\phi,-d\cos\phi)$
$5.55^\circ < \Phi <$	$d_1 < d \leqslant d_1+d_2\,(1)$	$\vec{d}=(d\sin\phi,(d-2d_1)\cos\phi)$
$22.386^\circ, S(1)$	$d_1+d_2 < d \leqslant d_1+d_2+d_3\,(2)$	$\vec{d}=\begin{pmatrix}(d_1+d_2)\sin\phi-(d-d_1-d_2)\cos(18^\circ+\phi),\\(d_2-d_1)\cos\phi-(d-d_1-d_2)\sin(18^\circ+\phi)\end{pmatrix}$
$\rightarrow S(3)\rightarrow S(5)$	$d_1+d_2+d_3 < d\,(3)$	$\vec{d}=\begin{pmatrix}(d_1+d_2)\sin\phi-d_3\cos(18^\circ+\phi)+(d-d_1-d_2-d_3)\cos(\phi-18^\circ),\\(d_2-d_1)\cos\phi-d_3\sin(18^\circ+\phi)+(d-d_1-d_2-d_3)\sin(\phi-18^\circ)\end{pmatrix}$

where $d_1=\dfrac{R\cos 36^\circ}{\cos\phi}$, $d_2=\sqrt{(x_2-x_1)^2+(y_2-y_1)^2}$, $d_3=\sqrt{(x_3-x_2)^2+(y_3-y_2)^2}$

$(x_1,y_1)=(R\cos 36^\circ\tan\phi,-R\cos 36^\circ)$, $(x_2,y_2)=\left(\dfrac{R(1+2\cos 36^\circ)}{\cot\phi+\tan 36^\circ},R-\tan 36^\circ\cdot x_2\right)$

$(x_3,y_3)=\begin{pmatrix}\dfrac{\tan(18^\circ+\phi)x_2-y_2-R(\cos 36^\circ+\sin 36^\circ\tan 72^\circ)}{\tan 72^\circ+\tan(18^\circ+\phi)},\\-\tan 72^\circ x_3-R(\cos 36^\circ+\sin 36^\circ\tan 72^\circ)\end{pmatrix}$

3:	$0 < d \leqslant d_1\,(0)$	$\vec{d}=(d\sin\phi,-d\cos\phi)$
$22.386^\circ < \Phi <$	$d_1 < d \leqslant d_1+d_2\,(1)$	$\vec{d}=(d\sin\phi,(d-2d_1)\cos\phi)$
$26.267^\circ, S(1)$	$d_1+d_2 < d \leqslant d_1+d_2+d_3\,(2)$	$\vec{d}=\begin{pmatrix}(d_1+d_2)\sin\phi-(d-d_1-d_2)\cos(18^\circ+\phi),\\(d_2-d_1)\cos\phi-(d-d_1-d_2)\sin(18^\circ+\phi)\end{pmatrix}$
$\rightarrow S(3)\rightarrow S(1)$	$d_1+d_2+d_3 < d \leqslant\,(3)$	$\vec{d}=\begin{pmatrix}(d_1+d_2)\sin\phi-d_3\cos(18^\circ+\phi)-(d-d_1-d_2-d_3)\cos(18^\circ+\phi),\\(d_2-d_1)\cos\phi-d_3\sin(18^\circ+\phi)+(d-d_1-d_2-d_3)\sin(18^\circ+\phi)\end{pmatrix}$

where $d_1=\dfrac{R\cos 36^\circ}{\cos\phi}$, $d_2=\sqrt{(x_2-x_1)^2+(y_2-y_1)^2}$, $d_3=\sqrt{(x_3-x_2)^2+(y_3-y_2)^2}$.

$(x_1,y_1)=(R\cos 36^\circ\tan\phi,-R\cos 36^\circ)$, $(x_2,y_2)=\left(\dfrac{R(1+2\cos 36^\circ)}{\cot\phi+\tan 36^\circ},\ R-\tan 36^\circ\cdot x_2\right)$,

$(x_3,y_3)=\left(\dfrac{y_2-\tan(18^\circ+\phi)x_2-R}{\tan 36^\circ-\tan(18^\circ+\phi)},\ y_3=R\cos 36^\circ\right)$

Table 3-4-1 (Continued)

Condition	Range/(No. of Reflections)	Vector Form
4:	$0 < d \leqslant d_1$ (0)	$\vec{d}=(d\sin\phi,-d\cos\phi)$
$26.267^\circ < \Phi$	$d_1 < d \leqslant d_1+d_2$ (1)	$\vec{d}=(d\sin\phi,(d-2d_1)\cos\phi)$
$36^\circ, S(1)$	$d_1+d_2 < d \leqslant d_1+d_2+d_3$ (2	$\vec{d}=\begin{pmatrix}(d_1+d_2)\sin\phi+(d-d_1-d_2)\cos(54^\circ+\phi),\\(d_2-d_1)\cos\phi+(d-d_1-d_2)\sin(54^\circ+\phi)\end{pmatrix}$
$\rightarrow S(2) \rightarrow S(3)$	$d_1+d_2+d_3 < d \leqslant d_1+d_2+d_3+d_4$ (3)	$\vec{d}=\begin{pmatrix}(d_1+d_2)\sin\phi+d_3\cos(54^\circ+\phi)-(d-d_1-d_2-d_3)\cos(54^\circ-\phi)\\(d_2-d_1)\cos\phi+d_3\sin(54^\circ+\phi)-(d-d_1-d_2-d_3)\sin(54^\circ-\phi)\end{pmatrix}$
$\rightarrow S(5)$	$d_1+d_2+d_3+d_4 < d$ (4)	$\vec{d}=\begin{pmatrix}(d_1+d_2)\sin\phi+d_3\cos(54^\circ+\phi)-d_4\cos(54^\circ-\phi)+(d-d_1-d_2-d_3-d_4)\cos(\phi-18^\circ),\\(d_2-d_1)\cos\phi+d_3\sin(54^\circ+\phi)-d_4\sin(54^\circ-\phi)+(d-d_1-d_2-d_3-d_4)\sin(\phi-18^\circ)\end{pmatrix}$

where $d_1=\dfrac{R\cos 36^\circ}{\cos\phi}$, $d_2=\sqrt{(x_2-x_1)^2+(y_2-y_1)^2}$, $d_3=\sqrt{(x_3-x_2)^2+(y_3-y_2)^2}$, $d_4=\sqrt{(x_4-x_3)^2+(y_4-y_3)^2}$

$(x_1,y_1)=(R\cos 36^\circ\tan\phi,-R\cos 36^\circ)$, $(x_2,y_2)=\left(\dfrac{R(1+2\cos 36^\circ)}{\cot\phi+\tan 36^\circ},\ \cot\phi\cdot x_2-2R\cos 36^\circ\right)$,

$(x_3,y_3)=\left(\dfrac{R+\tan(54^\circ+\phi)x_2-y_2}{\tan 36^\circ+\tan(54^\circ+\phi)},-\tan 36^\circ x_3+R\right)$. $(x_4,y_4)=\left(\dfrac{\tan(54^\circ-\phi)x_3-y_3-R(\cos 36^\circ+\sin 36^\circ\tan 72^\circ)}{\tan 72^\circ+\tan(54^\circ-\phi)},\right.$
$\left.-\tan 72^\circ x_4-R(\cos 36^\circ+\sin 36^\circ\tan 72^\circ)\right)$

Mirror Folding

Previous section proposes a method of finding the ray exit locations. This section provides another approach to determining ray exit locations, using a square light pipe as an example. The square *A* in Fig. 3-4-4(a) shows the ray propagation path projected on the light pipe exit surface. When the ray touches the pipe wall, it will be reflected. If the square is folded, the ray will propagate in a straight line like a virtual image in a mirror.

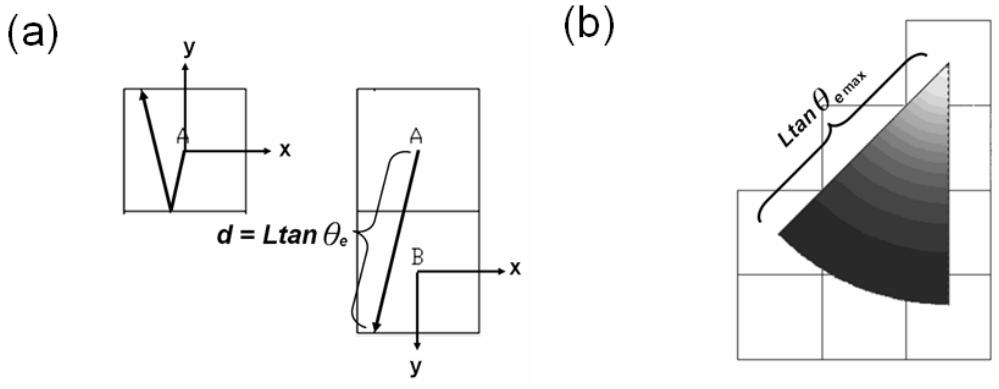

Figure 3-4-4 (a) Schematic diagram of a ray propagated in a folding square light pipe; (b) Ray exit location range in a folding square light pipe.

Figure 3-4-4(a) shows that the ray path in square light pipe *A* can be mapped into the

folded square *B*, reversing the coordinate axis. If a 45° fan with a radius $L\tan\theta_{e\max}$ is overlaid with folded squares, the fan area contains all ray exit locations with emitting ranges $0°<\phi<45°$ and $0°<\theta_e<\theta_{e\max}$, where θ_e is the ray entrance angle, $\theta_{e\max}$ is the maximum of θ_e, and the ray fan gradient represents the ray density exit location , as Fig. 3-4-4(b) shows. When ϕ is fixed and θ_e increases, rays are located on different squares. Depending on the sequence in which they pass through the squares, rays can be classified in four conditions, as Fig. 3-4-5 shows.

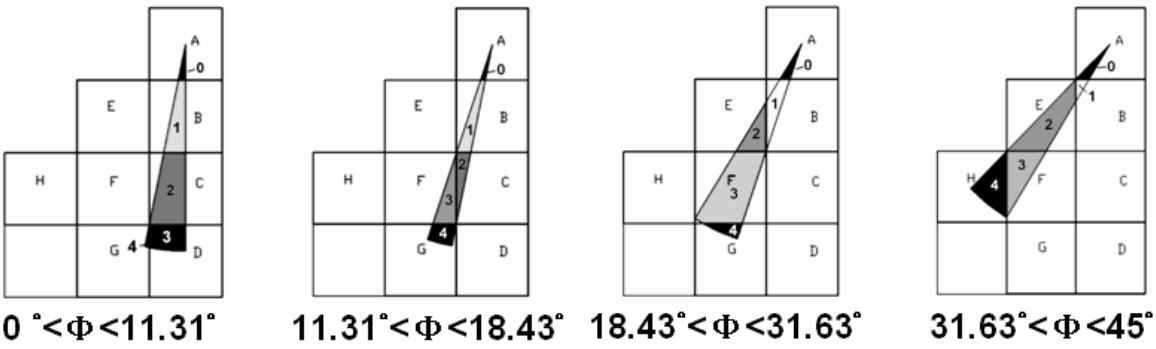

Figure 3-4-5 Four conditions of mirror folding method.

In other words, one 45° fan can be divided into four minor fans, and the numerical tag on each region represents the number of reflections. A different light pipe length *L* leads to a different fan radius $L\tan\theta_{e\max}$, and the corners of the folded squares intersected and overlaid with the 45° fan denote the total number of conditions and the range of each condition. To deduce the ray location equation, the symbols must be defined first: *w* is the square semi-width, *P* is the vector from square *A* center (the coordinate origin) to the ray exit location at some specific ϕ and θ_e, *A*~*H* are the coordinates of each square center, and d_1~d_4 are the boundary conditions. The expression of each symbol is:

$w = R\sin 45°$, $P = \left(-L\tan\theta_e\cdot\sin\phi,\ -L\tan\theta_e\cdot\cos\phi\right)$,

$A = (0,\ 0)$, $B = (0,\ -2w)$, $C = (0,\ -4w)$, $D = (0,\ -6w)$,

$E=(-2w,\ -2w)$, $F=(-2w,\ -4w)$, $G=(-2w,\ -6w)$, $H=(-4w,\ -4w)$

The ray exit location vector $\vec{d}(\theta_e,\phi)$ on the exit surface can now be deduced for any θ_e and ϕ. Table 3-4-2 lists the results.

Table 3-4-2 Ray exit location deduction of square light pipe

Condition	Range/(No. of Reflections)	Vector Form
1: $0°<\Phi<11.31°$, Square $A\rightarrow B\rightarrow C\rightarrow D\rightarrow G$	$0<d\leq d_1$ (0)	$\vec{d}=\overrightarrow{PA}$
	$d_1<d\leq d_2$ (1)	$\vec{d}=\overrightarrow{PB}\cdot(1,-1)$
	$d_2<d\leq d_3$ (2)	$\vec{d}=\overrightarrow{PC}$
	$d_3<d\leq d_4$ (3)	$\vec{d}=\overrightarrow{PD}\cdot(1,-1)$
	$d>d_4$ (4)	$\vec{d}=\overrightarrow{PG}\cdot(-1,-1)$
where $d_1=\frac{w}{\cos\phi}$, $d_2=3w\sqrt{(1+\tan^2\phi)}$, $d_3=5w\sqrt{(1+\tan^2\phi)}$, $d_4=w\sqrt{(1+\cot^2\phi)}$		
2: $11.31°<\Phi<18.43°$, Square $A\rightarrow B\rightarrow C\rightarrow F\rightarrow G$	$0<d\leq d_1$ (0)	$\vec{d}=\overrightarrow{PA}$
	$d_1<d\leq d_2$ (1)	$\vec{d}=\overrightarrow{PB}\cdot(1,-1)$
	$d_2<d\leq d_3$ (2)	$\vec{d}=\overrightarrow{PC}$
	$d_3<d\leq d_4$ (3)	$\vec{d}=\overrightarrow{PF}\cdot(-1,1)$
	$d>d_4$ (4)	$\vec{d}=\overrightarrow{PG}\cdot(-1,-1)$
where $d_1=\frac{w}{\cos\phi}$, $d_2=3w\sqrt{(1+\tan^2\phi)}$, $d_3=w\sqrt{(1+\cot^2\phi)}$, $d_4=5w\sqrt{(1+\tan^2\phi)}$		
3: $18.43°<\Phi<31.63°$, Square $A\rightarrow B\rightarrow E\rightarrow F\rightarrow G$	$0<d\leq d_1$ (0)	$\vec{d}=\overrightarrow{PA}$
	$d_1<d\leq d_2$ (1)	$\vec{d}=\overrightarrow{PB}$
	$d_2<d\leq d_3$ (2)	$\vec{d}=\overrightarrow{PE}\cdot(-1,-1)$
	$d_3<d\leq d_4$ (3)	$\vec{d}=\overrightarrow{PF}\cdot(-1,1)$
	$d>d_4$ (4)	$\vec{d}=\overrightarrow{PG}\cdot(-1,-1)$
where $d_1=\frac{w}{\cos\phi}$, $d_2=w\sqrt{(1+\cot^2\phi)}$, $d_3=3w\sqrt{(1+\tan^2\phi)}$, $d_4=5w\sqrt{(1+\tan^2\phi)}$		
4: $31.63°<\Phi<45°$, Square $A\rightarrow B\rightarrow E\rightarrow F\rightarrow H$	$0<d\leq d_1$ (0)	$\vec{d}=\overrightarrow{PA}$
	$d_1<d\leq d_2$ (1)	$\vec{d}=\overrightarrow{PB}\cdot(1,-1)$
	$d_2<d\leq d_3$ (2)	$\vec{d}=\overrightarrow{PE}\cdot(-1,-1)$
	$d_3<d\leq d_4$ (3)	$\vec{d}=\overrightarrow{PF}\cdot(-1,1)$
	$d>d_4$ (4)	$\vec{d}=\overrightarrow{PH}$
where $d_1=\frac{w}{\cos\phi}$, $d_2=w\sqrt{(1+\cot^2\phi)}$, $d_3=3w\sqrt{(1+\tan^2\phi)}$, $d_4=3w\sqrt{(1+\cot^2\phi)}$		

This approach can evaluate the ray exit positions of a square light pipe, and is simpler than the approach in previous section. Applying this method, such as summing to find the irradiance distribution or the actual ray position on the output surface, the flipping of the coordinate must be noticed.

Figures 3-4-6(a)~3-4-6(c) show that this approach can be applied to triangular and hexagonal light pipes, but is unsuitable for pentagonal pipes. The mirrored apertures in a pentagonal pipe cannot be geometrically arranged well because the pentagon angle (108°) is not a common divisor of 360°.

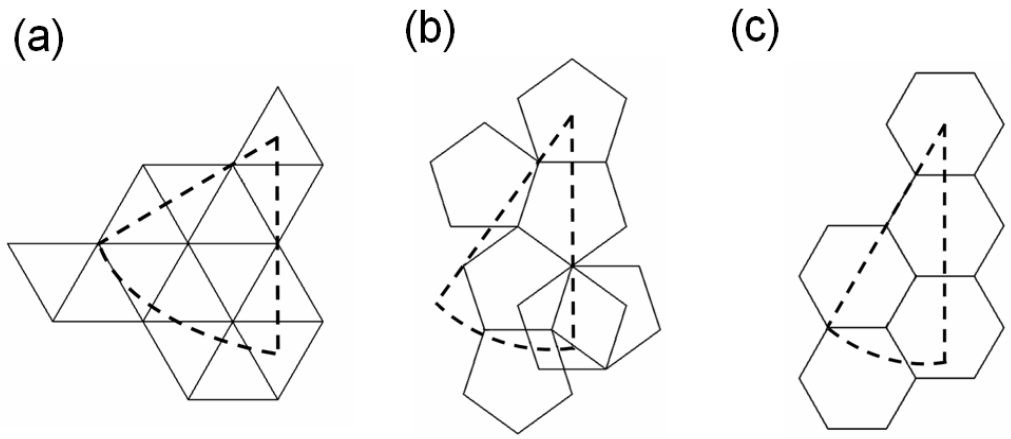

Figure 3-4-6 Exit surface folding for different shapes of light pipes: (a) triangle; (b) pentagonal; (c) hexagonal.

Polygonal Light Pipe Irradiance Distribution

According to the approaches in last two sections, ray locations can be determined for the exit surfaces of various geometrically-shaped light pipes. Collecting the flux for each ray enables the deduction of the irradiance distribution on the light pipe exit. For example, Fig. 3-4-7 shows a pentagonal exit surface which is superposed by concentric rings, and each ring has the same width Δr.

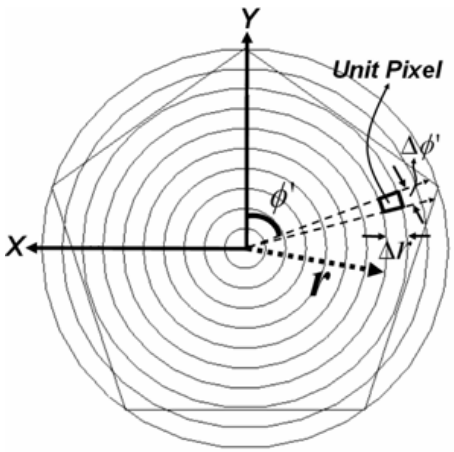

Figure 3-4-7 Schematic diagram of flux collection for a pentagonal light pipe

For a point Lambertian source, the normalized intensity follows $I(\theta_i)=\cos\theta_i$, where θ_i is the ray emitting angle. That means that when one Lambertian ray propagates in θ_i direction, the flux collected from this ray in unit solid angle is $\cos\theta_i$, and the irradiance on the detector unit pixel contributed by this ray is also $\cos\theta_i$. Ignoring the absorption of the light pipe material, the flux carried by each ray with entrance angle θ_e in any incident plane angle ϕ inside the light pipe can also be treated as $\Phi(\theta_e)=\cos\theta_i=\sqrt{1-n^2\sin^2\theta_e}$, which is independent of ϕ. Fresnel loss describes the ray energy lost through the dielectical material and air interface [3-10]. The TIR light pipe energy loss can be deduced by the Fresnel equation [3-10], and the reflectance R on the interface is

$$R=\left|\frac{n_i\cos\theta_i-n_t\cos\theta_t}{n_i\cos\theta_i+n_t\cos\theta_t}\right|^2 \qquad (3\text{-}4\text{-}3)$$

where i and t denote the incident and transmissive rays, respectively. This equation is only applicable to TIR loss at the input and output interfaces. On the other hand, referring to Eq.(3-4-2) and Table 3-4-1, it is possible to extract rays when the exit location vector $\vec{d}(\theta_e,\phi)=(\vec{x},\vec{y})$ is located at the same radial angle $\phi'=\cos^{-1}\left(\frac{\vec{x}\cdot\vec{y}}{\|\vec{x}\|\|\vec{y}\|}\right)$ on the light pipe exit plane. Irradiance distribution can then be deduced for some specific direction ϕ'. The average irradiance in each unit pixel at some specific ϕ' at the light pipe exit is

$$\begin{aligned}E(r)&=\frac{Total\ \ flux\ of\ \ one\ unit\ \ pixel}{Area\ of\ \ one\ unit\ \ pixel}\\&\approx\frac{\sum(1-R_{in})(1-R_{out})\Phi(\theta_e)}{r\Delta r\Delta\phi'}\end{aligned} \qquad (3\text{-}4\text{-}4)$$

where r is the ring radius and $\Delta\phi'$ is the radial angular range of each unit pixel.

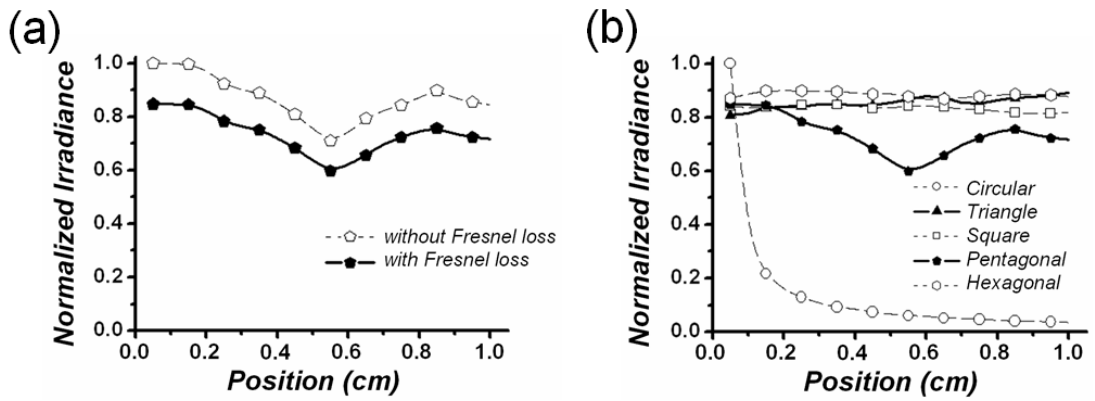

Figure 3-4-8 Irradiance distribution of *L/2R*=5 light pipes (a) pentagonal aperture; (b) different geometric shapes.

Figure 3-4-8(a) shows the calculated irradiance distribution of a pentagonal light pipe, with length L=10, cross section circumradius R=1, and material refractive index=1.493 (Acrylic). The two curves represent examples with and without Fresnel loss. The results indicate that the flux is localized at the light pipe center, decays along the radial direction, but increases at outboard. Fresnel loss decreases the irradiance, but does not affect the distribution trend. The analysis above was produced with MATLAB [3-11], where the angular entrance ray ϕ ranges from 0° to 36°, θ_e ranges from 0° to 39°, and the angular displacement is 0.1°. Figure 3-4-8(b) shows the calculated results (with Fresnel loss) of triangular, square, pentagonal, hexagonal, and circular TIR straight light pipes. The light pipe length and cross section diameter ratio *L/2R* is 5. These results indicate that triangular, square, and hexagonal light pipes exhibit uniform irradiance distribution, but pentagonal and circular light pipes have flux localized characteristics. This conclusion agrees with previous studies [3-10] [3-11].

Simulation Verification

For further analysis, we also used TracePro to verify the previous deduction. Different geometric shapes of TIR light pipes were built of acrylic material (n=1.493), including triangular, square, pentagonal, hexagonal, and circular straight light pipes. Each light pipe

has a length of 10cm, and the circumradius is 1cm. The Lambertian point-like source was placed outside the material and in front of the center of each light pipe input at a distance of 0.01mm. The Fresnel loss at the material and air interface was calculated. A corresponding detector with the same size as the light pipe aperture was set behind the exit to collect the flux. The sampling of detector has 21x21 points, and a smoothing with 128x128 resolutions was set to increase realistic rendering. Figures 3-4-9(a)~3-4-9(e) show the ray tracing results. Figure 3-4-9(f) shows the irradiance cross profiles, and the arrows in Figs. 3-4-9(a)~3-4-9(e) indicate the crosscut direction. The simulation results are consistent with the analytical results in the previous section. Comparing Fig. 3-4-9(f) with Fig. 3-4-8(b) reveals that the pentagonal light pipe has flux localized characters, while the triangular, square, and hexagonal apertures show uniformity. The circular light pipe also shows a hot spot, much like a hollow case.

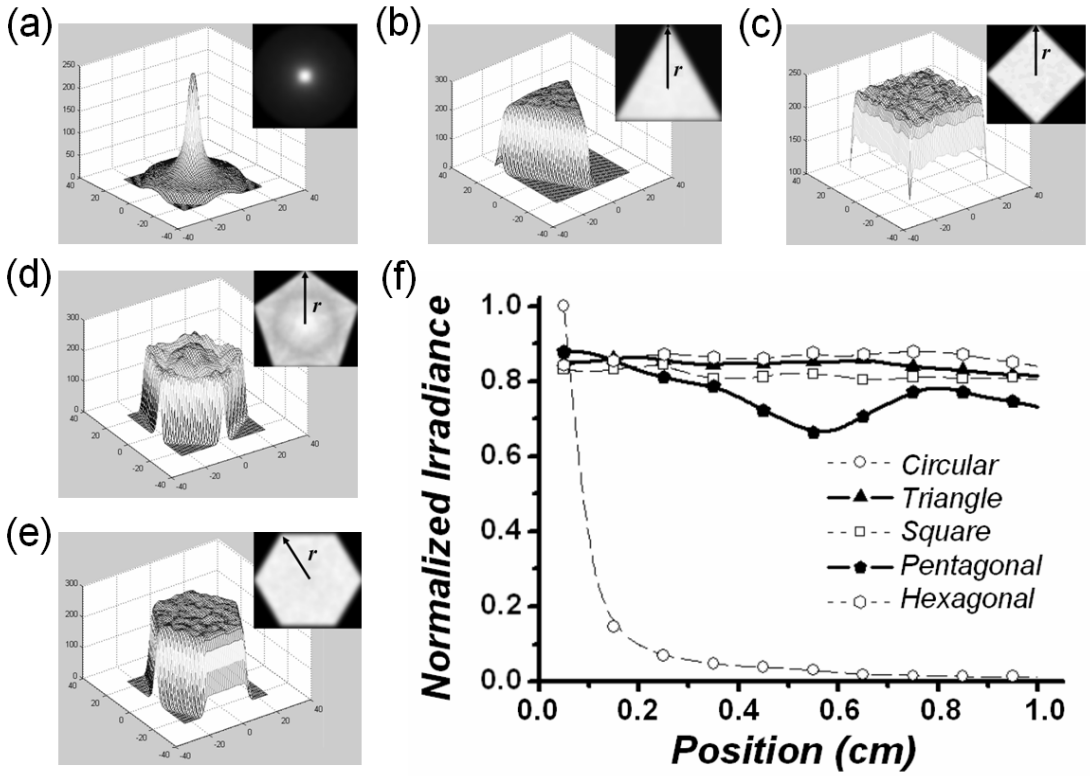

Figure 3-4-9 Simulation results of irradiance distribution for different geometric shapes of light pipes: (a) circular; (b) triangle; (c) square; (d) pentagonal; (e) hexagonal; (f) cross profiles of each light pipe.

Experimental Exploration

A real experiment can be considered for further discussion. This experiment involves different geometric shapes of straight acrylic light pipes and a Lambertian white-light emitting diode (Lumileds, model PW09), which served as the light source. The PW-09 LED source has a Lambertian emitting angular property, and the emitting area diameter is 5.25mm [3-12]. A diffusive sheet with uniform random roughness was placed at the light pipe output, serving as an image plane. The irradiance distribution shown on the diffusive sheet was captured by a commercial digital camera (Nikon, model D70) with a 3008x2000 pixel resolution. All measurements were taken in a dark room to prevent ambient light interference.

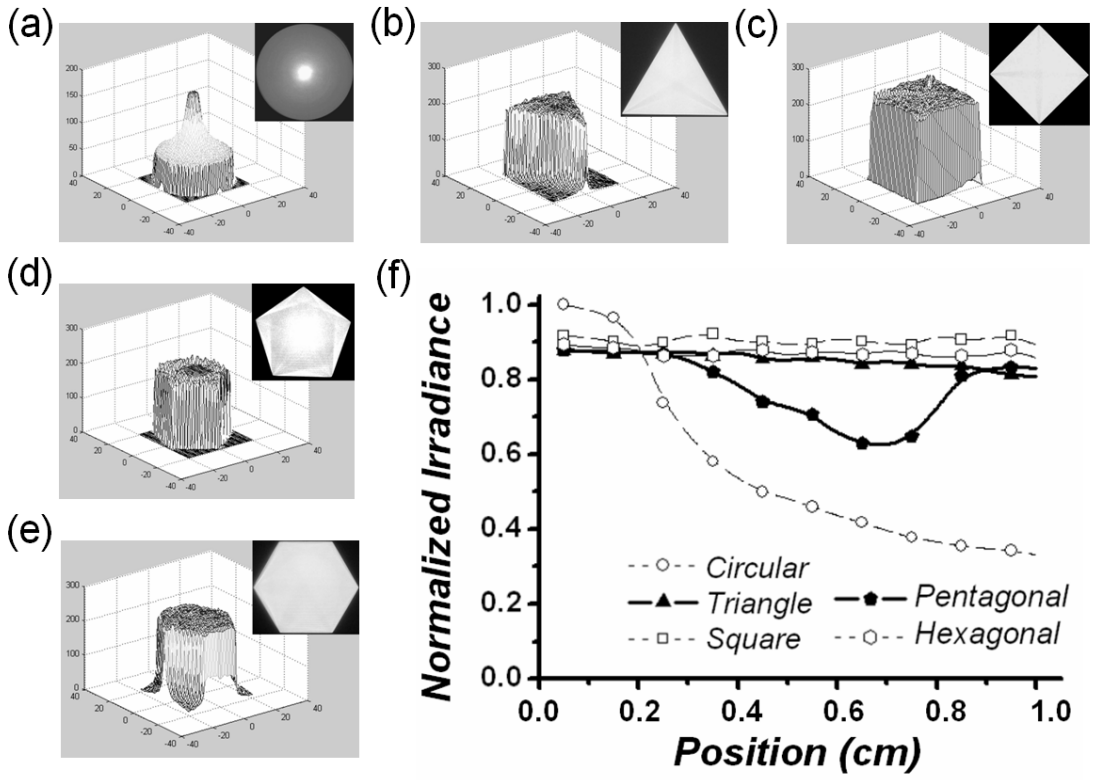

Figure 2-4-10 Experimental results of irradiance distribution for different geometric shapes of light pipes: (a) circular; (b) triangle; (c) square; (d) pentagonal; (e) hexagonal; (f) cross profiles of each light pipe.

Figures 3-4-10(a) ~3-4-10(e) show the image output from the light pipe exit. These figures show irradiance characteristics similar to those in the simulation. The experimental

result profiles were further processed by MALAB to intercept the cross-section plots, and Fig. 3-4-10(f) shows the results. The circular aperture has a hot spot. The pentagonal light pipe also shows irradiance decay along the radial direction, but the irradiance increases on the fringe. The triangular, square, and hexagonal light pipes have uniform distribution. The experiment and theoretical results exhibit the same characteristics

Some differences between the experimental and theoretical results still remain, and these differences can be attributed to three causes: (1) Material scattering and ray leakage due to imperfectly polished light pipe surfaces, which would influence the observability of the irradiance characteristics, especially in a circular light pipe; (2) Manufacturing defects of polygonal edges and angles, which would create veins in irradiance patterns and affect the uniformity of triangular, square, and hexagonal light pipes; (3) A finite-sized LED source. Hence, the observed irradiance is composed of the irradiance patterns of infinite point sources from different emitted positions. The following section provides further discussion of the source size influence.

The Influence of Light Pipe Length and Source Size

In the previous sections, simulation and experimental results both show that circular and polygonal light pipes have flux localized characteristic. *How does the localization vary with the light pipe length and source size?*

Investigating this issue requires a discussion of the pentagonal light pipe first. Several acrylic pentagonal light pipes were built, all with the same circumradius R but different lengths L. The irradiance profiles of different light-pipe lengths were compared within a range from L/R=1 to L/R=20. Figure 3-4-11(a) shows that when the L/R ratio was less than 10, flux localized characteristics could be observed. Once the pentagonal light pipe is long enough (L/R~20), a uniform irradiance arises. Figure 3-4-11(b) shows the irradiance profiles of one L/R=10 circular light pipe with various source sizes. For comparison, the source's

scale dimension was normalized to the light pipe radius and denoted as *S*. The simulation was carried out from a point-like source to a source size 99% of the incident plane. The results show that the circular light flux localization decreases as the source size increases. This corresponds to the circular light pipe experimental result above, which used a PW-09 LED about *S=2.5* in size. To further evaluate the irradiance, we introduced uniformity deviation defined by

$$\delta = \left[\frac{1}{n} \sum_{i=1}^{n} \left| E_i - \overline{E} \right| \right] \Big/ \overline{E}, \qquad \text{(3-4-5)}$$

where $\overline{E}$ indicates the average irradiance of *n* sampling points. The deviation can serve as a merit function to evaluate light pipe performance when processing a uniform illumination design. This study used 21*21 sampling points, which were equally distant from each other and located at the observation plane, to calculate the uniformity deviation. Figure 3-4-11(c) shows the uniformity deviation variance of a pentagonal light pipe, and the variables are light pipe length and source size. As the *L/R* ratio increases, the uniformity deviation decreases. Magnifying the source size also eliminate it.

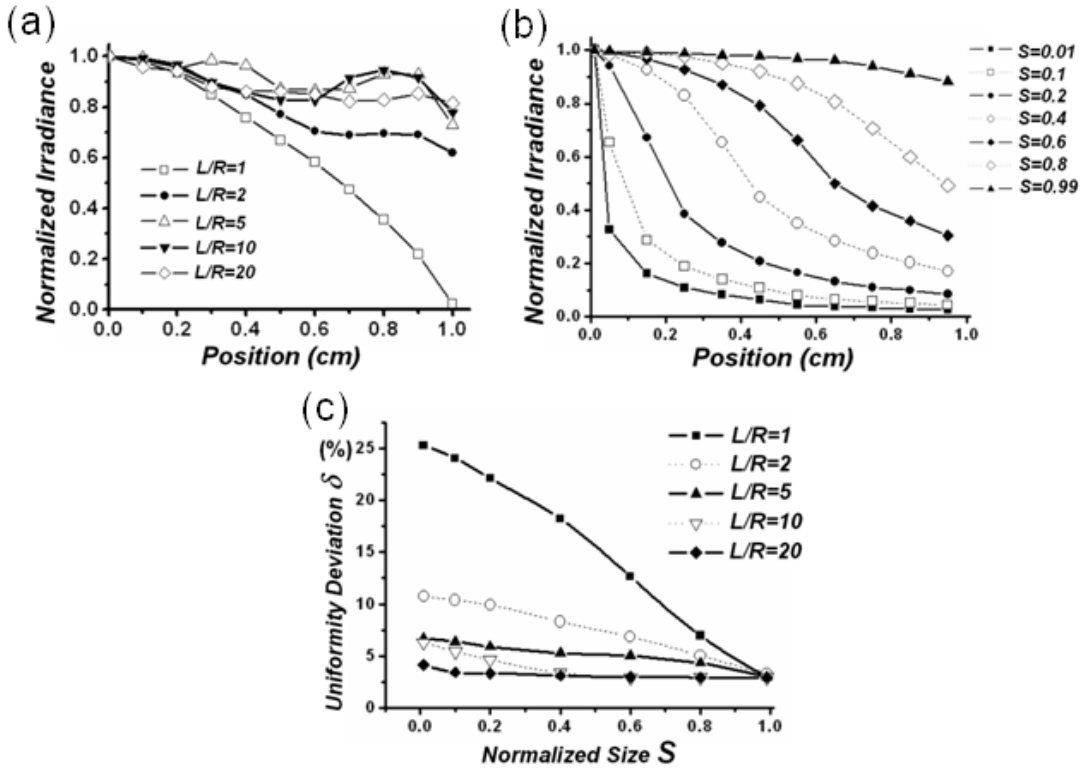

Figure 3-4-11 (a) Irradiance profiles for pentagonal light pipe with different *L/R* ratio; (b) Irradiance profiles for circular light pipe with different source size; (c) Uniformity deviation versus light pipe scale *L/R* for a pentagonal light pipe.

Table 3-4-3 lists the smallest uniform-mixing *L/R* ratio (least integer, when δ<5%) for on-axis point Lambertian source in polygonal light pipes. The uniform-mixing *length/circumradius* ratio could be an important factor when designing light pipe systems. Table 3-4-3 indicates that triangular, square, and hexagonal light pipes are suitable for uniform illumination applications, while the “hot spot” of circular light pipes cannot be eliminated by increasing light pipe length. These results are consistent with analytical modeling results. A pentagonal light pipe remains flux localized until the *L/R* ratio equals 19.

Table 3-4-3 Lists of smallest uniform-mixing *L/R* ratios

No. of Light-Pipe Edges	Smallest Uniform-Mixing *L/R* Ratio	Uniformity Deviation δ (%)
Circular	N/A	>66
3	3	4.62
4	3	4.59
5	19	4.31
6	3	4.81

3-5 Summaries

In summary, the irradiance distributions of different geometrical shapes of hollow and total-internal-reflection (TIR) straight light pipes with a point Lambertian source were deduced analytically and investigated using a Monte Carlo, non-sequential ray tracing simulation. This study proposes two methods of tracing the ray location paths on the light pipe exit, and further, collecting the flux which forms the irradiance distribution. Analytical and simulation results both show that circular and pentagonal light pipes have flux localized characters, while triangular, square, and hexagonal light pipes exhibit uniform distribution. This study also conducts experimental exploration and confirmation of polygonal acrylic light pipes with a white-light emitting diode.

References

[3-1] K. K. Li, “Illumination engine for a projection display using a tapered light pipe,” U.S. Patent #6739726 (2005).

[3-2] N. Takahashi and S. Umemoto, “Liquid crystal display apparatus having light pipe with reflective polarizer,” U.S. Patent #6778235 (2004).

[3-3] J. Lee and J. E. Greivenkamp, “Modeling of automotive interior illumination systems,” *Opt. Eng.* **43,** 1537–1544 (2004).

[3-4] H. Delattre, “Motor vehicle headlight with light pipe,” U.S. Patent #6547428 (2003).

[3-5] R. E. Fischer and B. Tadic-Galeb, *Optical System Design*, (McGraw-Hill, New York, 2000), p. 297.

[3-6] A. Gupta, J. Lee, and R. J. Koshel, “Design of efficient lightpipes for illumination by an

analytical approach," *Appl. Opt.* **40**, 3640-3648 (2001).

[3-7] F. Zhao, N. Narendran, and J. Van Derlofske, "Optical Elements for mixing colored LEDs to create white light," *Solid State Lighting II. Proceedings of the SPIE*, vol. 4776, 206-214 (2003).

[3-8] Y. -K. Cheng and J. -L. Chern, "Irradiance formations in hollow straight light pipes with square and circular shapes," J. Opt. Soc. Am. A **23**, 427-434 (2006).

[3-9] Y. -K. Cheng, M. -H. Wang, and J. -L. Chern, "Irradiance formations of on-axis Lambertian pointlike sources in polygonal total-internal-reflection straight light pipes", J. Opt. Soc. Am. A **24**, 2748-2757 (2007).

[3-10] M. Born and E. Wolf, Principles of Optics, 7th ed.(Cambridge U. Press, 1999), pp. 42–43, 50–51.

[3-11] More information on MatLab can be found at http://www.mathworks.com.

[3-12] More information on PW-09 LED can be found at http://www.lumileds.com.

Chapter 4

Polarization Properties and Applications of Light Pipes

4-1 Motivation

Preserving the polarization of a beam of light after propagation has many practical uses in a variety of applications such as biological tissue light probes or ellipsometers for refractive index and film thickness measurement, etc. [4-1] [4-2]. When light is propagated, displaced, or deflected, its polarization is usually changed. For example, when light bounces off a reflective mirror, the reflection introduces an additional phase that alters the polarization of the light beam. Azzam suggested solutions to displace a monochromatic light beam parallel to itself without change of polarization by utilizing a pair of parallel mirrors with a single dielectric layer coating [4-3] [4-4]. On the other hand, Cojocaru [4-5] and Wang et al. [4-6] proposed the design of coating layers with totally reflecting prism to provide a convenient and efficient method to control the phase retardance. Galvez presented the combinations of four total reflecting prisms to preserve polarization [4-7]. Galves' scheme has benefits in achromatic application and very good tolerance which can preserve the polarization with a square of ellipse ratio variation of less than 1% while one degree of component tilt occurs [4-8]. These studies provide very useful schemes to maintain polarization, but they generally focus on the displacement of a light beam, i.e., when the propagating direction of a displaced beam is parallel to the original beam. However, angular shifting is generally employed to reduce the optical path of beam propagation and hence the system size, which has practical value. Technically, polarization-preserving angular shifting provides more flexibility in optical engineering applications, e.g., polarized light probe with angular incident injection could provide another useful scheme in exploring 3D structure and response. However, it is

quite uncertain and difficult to deflect the beam direction while maintaining the state of polarization using this technique. This study proposes and numerically verifies novel polarization-preserving beam angular shifters based on a wedge plate and a circular-bent light pipe. A polarization-preserving wedge or bent light pipe has an advantage in manufacture and has better extendibility on the applications of polarization controlling mechanisms. A polarization-preserving wedge or bent light pipe can provide both spatial and angular shift of beam propagation path, and zero vertex angle/bent angle can reduce a wedge/light pipe angular shifter to become a beam displacer. Our work had also been published in academic papers [4-9] [4-10].

4-2 Wedge Type Polarization-Preserving Angular Shifter

Let us first summarize the general properties of a polarized ray propagating in a dielectric-filled material. According to Fresnel's equations, the transmitted and reflected fields of a light beam on air-dielectric interface follows [4-11]

$$R_s = \frac{\cos\theta_i - n\cos\theta_t}{\cos\theta_i + n\cos\theta_t} E_s, \quad R_p = \frac{n\cos\theta_i - \cos\theta_t}{n\cos\theta_i + \cos\theta_t} E_p,$$
$$T_s = \frac{2\cos\theta_i}{\cos\theta_i + n\cos\theta_t} E_s, \quad T_p = \frac{2\cos\theta_i}{n\cos\theta_i + \cos\theta_t} E_p \qquad (4\text{-}2\text{-}1)$$

In Eq. (4-2-1), *E*, *R*, and *T* represent the incident, reflected, and refracted fields, and the subscripts *s* and *p* denote the parallel and perpendicular directions, respectively. θ_i is the incident angle, θ_t is the angle of refraction, and *n* is the refractive index of the dielectric medium.

Stokes parameters make it possible to derive the Mueller matrix for the reflection and refraction on air-dielectric interface from Eq. (4-2-1). Referring to [4-12], the Mueller matrix of transmission on air-dielectric interface is

$$M_T = \frac{\sin 2\theta_i \sin\theta_t}{2(\sin\Theta_+ \cos\Theta_-)^2} \begin{pmatrix} \cos^2\Theta_- + 1 & \cos^2\Theta_- - 1 & 0 & 0 \\ \cos^2\Theta_- - 1 & \cos^2\Theta_- + 1 & 0 & 0 \\ 0 & 0 & 2\cos\Theta_- & 0 \\ 0 & 0 & 0 & 2\cos\Theta_- \end{pmatrix}, \qquad (4\text{-}2\text{-}2)$$

where $\Theta_\pm = \theta_i \pm \theta_t$, while for total internal reflection it follows that

$$M_{TIR} = \begin{pmatrix} 1 & 0 & 0 & 0 \\ 0 & 1 & 0 & 0 \\ 0 & 0 & \cos\Delta & -\sin\Delta \\ 0 & 0 & \sin\Delta & \cos\Delta \end{pmatrix}, \qquad (4\text{-}2\text{-}3)$$

where $\Delta = -2\tan^{-1}\left(\frac{\cos\theta_i\sqrt{n^2\sin^2\theta_i - 1}}{n\sin^2\theta_i}\right)$. Equations (4-2-2) and (4-2-3) govern the variations of polarization as a light ray interacts within a dielectric-filled material.

The next challenge is: *How can we design an optical component that is capable of*

guiding a ray to a special angular direction while simultaneously preserving its polarization? Technically, the total phase delay (or phase shift) during ray propagation must be kept as 2π, or an integral multiple of 2π, and the deflected angle between the exit and incident beams should match the designed value. The following section shows that a wedge plate is a possible candidate to achieve this goal.

The Issue of Polarization Preservation and Its Conditions

In this section, we will show how to resolve the issue indicated in above section. Much like the wedge plates considered in Refs. [4-13] and [4-14], Fig. 4-2-1 shows that a ray is incident to the narrow side of the wedge plate as long as the incident angle when the ray first strikes the top wedge surface is greater than the total internal reflection angle θ_c. This ray can continuously propagate between the top and bottom surfaces of the wedge plate until it reaches the wide side (or the exit surface). To avoid unnecessary complexity, the wedge input and exit surfaces were cut such that their directions of surface normal are the same as the directions of incident and exit beams, respectively. In Fig. 4-2-1, α_i is the angle between the ray propagation direction and the horizontal axis after the i^{th} total internal reflection, θ_i is the incident angle before the i^{th} total internal reflection, θ_v is the wedge vertex angle, and n is the refractive index of the plate material. Before leaving the wedge plate, this ray encounters m times of total internal reflection.

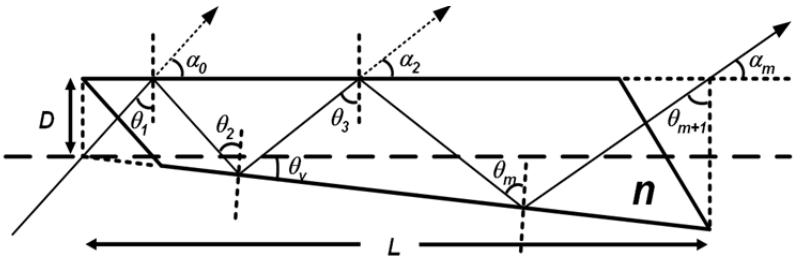

Figure 4-2-1 Schematic diagrams of ray propagating in a wedge plate

Without loss of generality, we assume this ray finally escapes from the top surface of the

wedge plate and *m* is an even number. The geometry in Fig. 4-2-1 shows that $\theta_i = \theta_1 + (i\text{-}1)\theta_v$, $\alpha_i = 90 - \theta_i - \theta_v$ (when *i* is even), and the ray deflection angle $\Delta\alpha = \alpha_0 - \alpha_m = m\theta_v$. In short,

$$\begin{cases} \Delta\alpha = m\theta_v \\ \sum_{i=1}^{m} -2\tan^{-1}\left(\dfrac{\cos[\theta_1 + (i-1)\theta_v]\sqrt{n^2 \sin^2[\theta_1 + (i-1)\theta_v] - 1}}{n\sin^2[\theta_1 + (i-1)\theta_v]} \right) = -2\pi \cdot k \end{cases}, \qquad (4\text{-}2\text{-}4)$$

where *m* is even and *k* is an integer. After specifying the ray deflection angle $\Delta\alpha$, multiple solutions of (θ_1, θ_v) can be derived from Eq. (4-2-4) with different values of *m* and *k*. Equation (4-2-4) is the basic condition of a polarization-preserving angular shifter for a wedge plate. Formally, θ_1 and θ_v are the dominate parameters in Eq. (4-2-4), but the real scale of the wedge plate, i.e., the width of input port *D*, and the total length of wedge *L*, provide the degree of freedom in an angular shifter.

Numerical Exploration

For a numerical illustration, consider a typical glass, BK7, where *n* = 1.51509 at 632.8nm, and request $\Delta\alpha = 30^o$. After solving, two solutions were arbitrarily selected for demonstrations: (1) *m*=10, $\theta_1 = 49.46^o$, $\theta_v = 3^o$, where the total phase delay is $\sim -2\pi$, i.e., -2π -7.3 x10^{-4}; and (2) *m*=20, $\theta_1 = 48.69^o$, $\theta_v = 1.5^\circ$, where the total phase delay is $\sim -4\pi$, i.e., -4π +6.3x10^{-5}. Figure 3-2-2 shows the series of a virtually folded wedge by which the multi-reflection ray path can be treated as a straight line. In Fig. 4-2-2, L_1 is the length from wedge vertex to first total internal reflection position and L_{m+1} is the length from wedge vertex to $(m+1)^{th}$ total internal reflection position. Simple mathematics prove that $L_1 = D(\cot\theta_v + \tan\theta_1)$ and $L_{m+1} = \dfrac{L_1 \cos\theta_1}{\sin(90^\circ - \theta_{m+1})}$, and hence, the total length *L* from the ray incident position to the exit position is

$$L = L_{m+1} - L_1 + D\tan\theta_1$$
$$= D(\cot\theta_v + \tan\theta_1)\frac{\cos\theta_1}{\cos(\theta_1 + m\theta v)} - D\cot\theta_v \cdot \qquad (4\text{-}2\text{-}5)$$

By Eq. (3-2-5), one can determine the exact size of the wedge plate by choosing the port width D or the wedge length L.

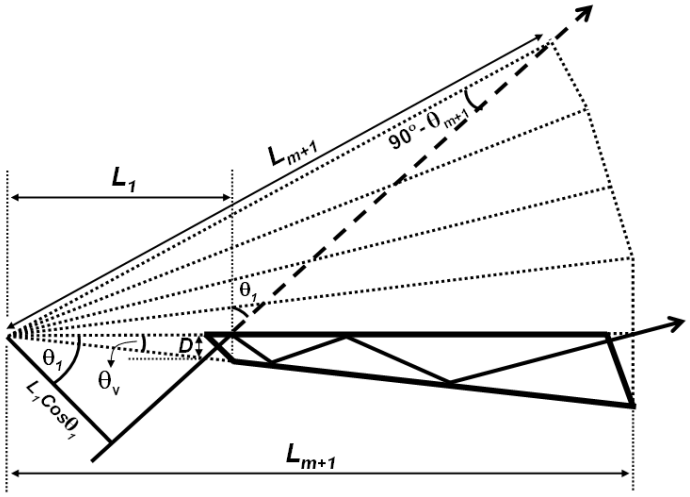

Figure 4-2-2 Schematic diagrams of ray propagating in a virtually folded wedge plate

In the numerical example above, θ_v =3°, and the thickness of the entrance port D=5mm. By Eq.(4-2-5), the plate length L is 264.5mm. For simplicity of presentation (without loss of generality), ignore the absorption for the time being. This study uses TracePro for numerical verification. A collimated beam with +45° linearly polarization was propagated into the wedge plate at α_0 =40.54°, and finally exited the wedge plate at α_{10} =10.54° after 10 total internal reflections. Figure 4-2-3(a) shows the polarization states (the Stokes parameters) after the ray encounters even times of total internal reflection. Ellipse ratio e of a linear polarized beam was considered and $e^2=I_{min}/I_{max}$ was calculated, where I_{max} and I_{min} are the maximum and minimum intensities of the optical beam, proportional to the squares of semimajor and semiminor axes of the ellipse, respectively, described by the beam's electric field vector. Results show that the output polarization beam has a good linear property, with the square of ellipse ratio e^2=1.3332x10^{-7} and the azimuth of polarization axis 44.51°. This study also considers an example of 20 total internal reflections, where D=5mm and θ_v =1.5°.

In this case, L=470.9mm, the incident angle is α_0=41.31^o, and hence, α_{20}=11.31^o. Figure 4-2-3(b) shows this simulation result, clearly indicating that the output beam also retains very good linear polarization characteristics with the squared ellipse ratio e^2=9.8809x10^{-10} and the azimuth of polarization axis 44.43^o.

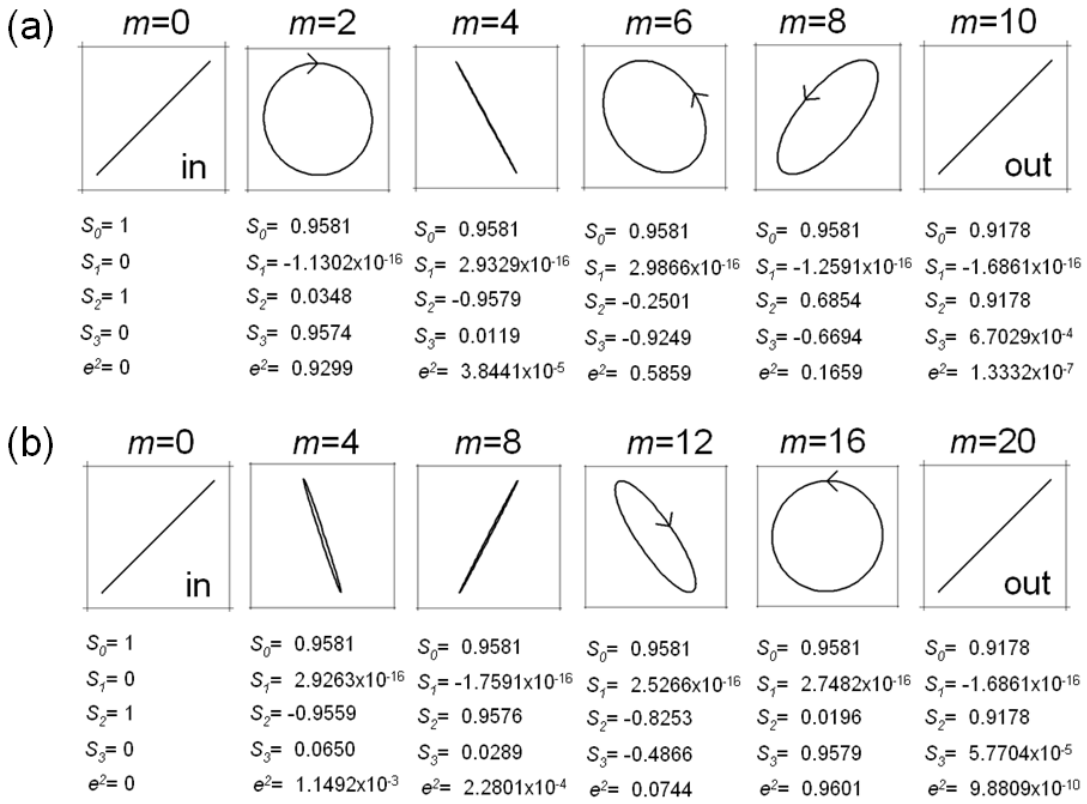

Figure 4-2-3 Polarization variations when total internal reflections happen, (a) m=10 and (b) m=20.

4-3 Polarization-Preserving Light Pipe

Another case to preserve polarization state of propagating ray is by take advantage of a circular-bent light pipe. Figure 4-3-1 shows a segment of the circular-bent light pipe, α_i is the angle between the ray propagation direction and the horizontal axis after the i^{th} total internal reflection, θ_i is the incident angle before the i^{th} total internal reflection, θ_f is the fan angle between i^{th} and $(i+1)^{th}$ reflections , and n is the refractive index of the plate material. To avoid complexity, we also cut the input and exit surfaces of circular-bent light pipe so that their directions of surface normal are the same as the directions of incident and exit beams. Similar to the deduction of wedge case in section 4-2, we have

$$\begin{cases} \Delta\alpha = m\theta_f \\ \sum_{i=1(odd)}^{m-1} -2\tan^{-1}\left(\dfrac{\cos(\alpha_0+\theta_f)\sqrt{n^2\sin^2(\alpha_0+\theta_f)-1}}{n\sin^2(\alpha_0+\theta_f)}\right) + \sum_{i=2(even)}^{m} -2\tan^{-1}\left(\dfrac{\cos\alpha_0\sqrt{n^2\sin^2\alpha_0-1}}{n\sin^2\alpha_0}\right) = -2\pi\cdot k \end{cases} \quad (4\text{-}3\text{-}1)$$

where m is even and k is an integer. After specifying the ray deflection angle $\Delta\alpha$, multiple solutions of (θ_1,θ_f) can be derived from Eq. (4-3-1) with different values of m and k, as the result of the wedge plate form . Equation (4-3-1) is the basic condition of a polarization-preserving angular shifter for a circular-bent light pipe. The width of input port D, and the radius of inner surface R, provides the degree of freedom in an angular shifter.

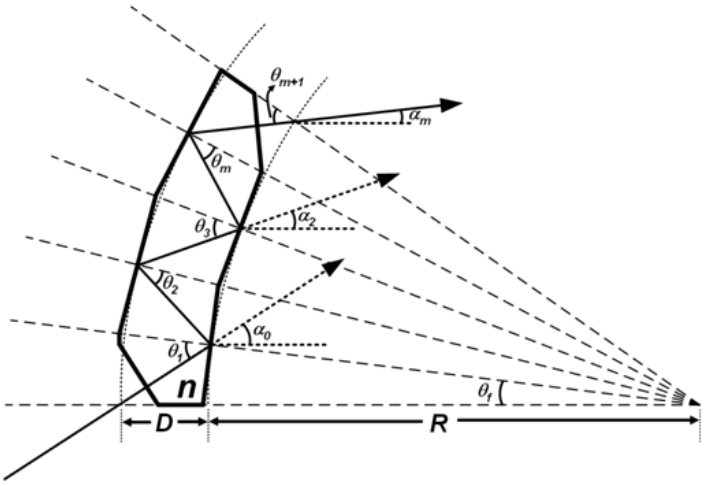

Figure 4-3-1 Schematic diagrams of ray propagating in a circular-bent light pipe

Numerical Exploration

In the circular-bent light pipe case, we also consider a typical glass, BK7, where n = 1.51509 at 632.8nm, but request $\Delta\alpha$ =60°. After solving, an arbitrarily solution was selected: m=10, θ_1 =42.54°, θ_f =6°, where the total phase delay is ~-2π, i.e., -2π -1.497 x10^{-4}. Figure 4-3-2 shows the ray path when first reflection occurs inside the circular-bent light pipe, D is the width of input port and R is the radius of light pipe inner surface, H is the height of first total internal reflection point. By simple trigonometry, one can prove

$$R = \frac{D \tan \alpha_0}{\sin \theta_f - \tan \alpha_0 + \cos \theta_f \tan \alpha_0}. \qquad (4\text{-}3\text{-}2)$$

By Eq. (4-3-2), we can determine the exact size of the circular-bent light pipe by choosing the port width D or the inner surface radius R.

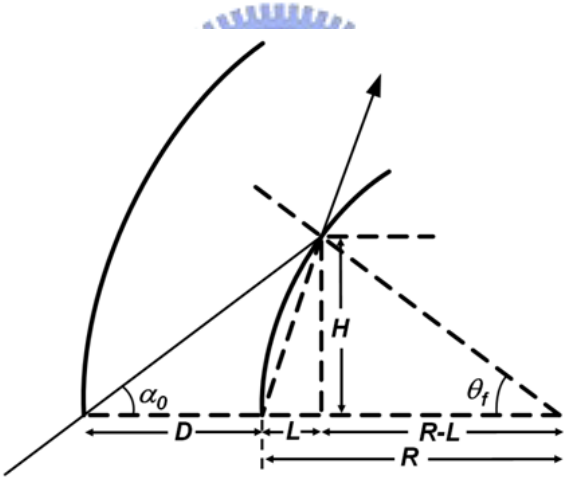

Figure 4-3-2 Schematic diagrams of ray first reflection in a circular-bent light pipe

For numerical verification, we choose the width D=5mm as the numerical example and the inner surface radius R is 46.11mm. The incident beam of numerical example was a collimated beam with right circular polarization, was propagated into the wedge plate at α_0 =42.54°, and finally exited the wedge plate at α_{10} = -17.46° after 10 total internal reflections. Results in Fig 4-3-3 show that the output polarization beam has a good circular property, with the square of ellipse ratioe^2=1-2.994x10^{-4}.

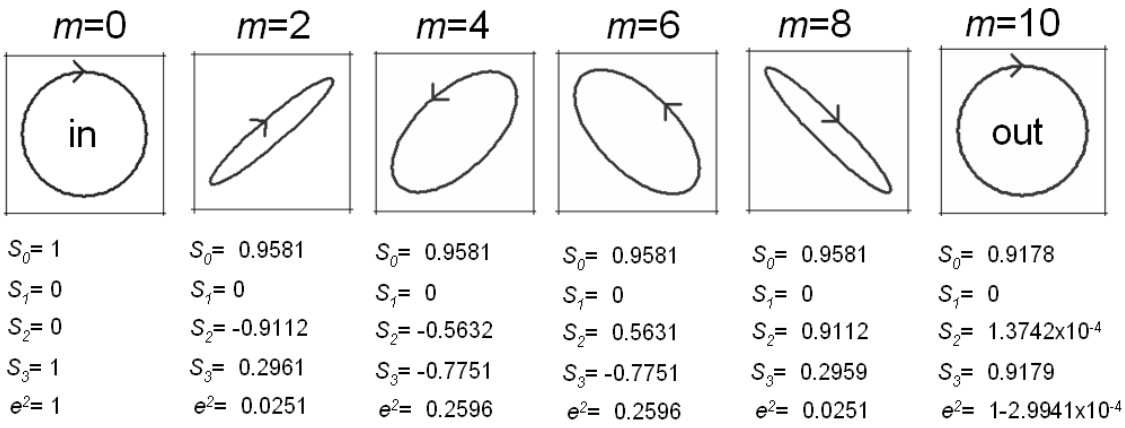

Figure 4-3-3 Polarization variations when total internal reflections happen in a circular-bent light pipe

4-4 Limitation and Tolerance Issue

Limitation of Polarization-Preserving Angular Shifter

Physically, the limit of the ray deflection angle $\Delta\alpha$ for wedge plate type polarization-preserving angular shifter should be less than the incident angle α_0, while α_0 should be less than 90^o-θ_c. For BK7 at a 632.8nm wavelength, the critical angle θ_c is 41.3^o, hence, the deflection angle $\Delta\alpha$ cannot be greater than 48.7^o when the wedge plate has an even number of reflections. Determining the limit of angular shifter is worthwhile, so this study explores the possible range of deflection angle $\Delta\alpha$ at specific vertex angles θ_v, which range from 0.5^o to 5^o with a unit of 0.25^o. Figure 4-4-1 shows the results, indicating that the available wedge vertex angle is limited from 0^o to 3.5^o, although the range bounded up to 5^o has been checked, and 8 total internal reflections are required for the wedge plate to preserve the polarization after ray propagation.

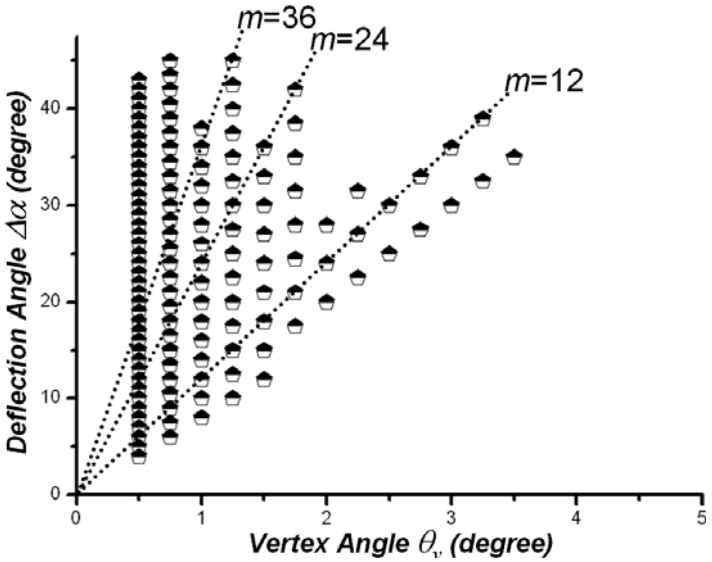

Figure 4-4-1 Possible ray deflection angles versus wedge vertex angle. The vertex angles θ_v is picked up from 0.5^o to 5^o with a unit of 0.25^o to determine the possible ray deflection angle.

A greater number of reflections increases the system dimensions and enlarges the phase difference caused by incident angle error. Figure 3-2-4 shows different solutions for three

reflection numbers *m*=12, 24, and 36 highlighted by dashed lines. This figure indicates that the maximal deflection angle can reach 39^o when the deflection number is 12, while twice as many reflections increase the deflection angle to 42^o, and three times as many reflections contributes an additional 3 degrees of deflection angle range.

For simplicity, this study only shows an even number of reflections for both cases. Nevertheless, one can simply multiply the deflection angle $\Delta\alpha$ twice by means of the wedge plate case with an odd number of total internal reflections. On the other hand, the circular-bent light pipe has an advantage than the wedge plate on the unlimited deflection angle range. Furthermore, utilizing multiple polarization-preserving wedges can also increase the deflection angle.

Tolerance Issue

A polarization-preserving wedge or bent light pipe can be manufactured using glass molding or plastic injection. The accuracy of the incident plane angle and incident beam angle plays an important role in preserving the polarization state. Figures 4-2-1 and 4-3-1 show that the polarized beam normally incidents to the obliquely-cut input surfaces and exits from the output surfaces after *m* total reflections in both cases. Incident angle errors negatively affect polarization-preserving shifter performance because additional phase delay arises with these errors occur.

This study discusses two kinds of variation on tolerance when the ray is propagating in a wedge.

(1): if the ray normally incident to the input surface which is tilted by a small angle δ_s, i.e. the incident angle $\alpha_0' = \alpha_0 + \delta_s$, then the ray angle after the m^{th} reflection for wedge plate is $\alpha_m' = \alpha_0 + \delta_s + m\ \theta_v$ and the ray exit angle becomes $\alpha_{out} = \alpha_0 + sin^{-1}(n\sin\delta) + m\,\theta_v = \alpha_m + sin^{-1}(n\sin\delta_s)$. The deflection angle of the output ray can

be altered by another small angle $sin^{-1}(n\sin\delta_s)-\delta_s$, i.e., $\Delta\alpha' = \Delta\alpha + sin^{-1}(n\sin\delta_s)-\delta_s = m\theta_v + sin^{-1}(n\sin\delta_s)-\delta_s$.

(2): even if surfaces of the polarization-preserving wedge is manufactured identically, but the misalignment of the incident beam with the incident plane decreases performance. When the incident beam is tilted a by small angle δ_i, i.e. the incident angle $\alpha_{in} = \alpha_0 + \delta_i$, the ray angle before first reflection should be adjusted to $\alpha_0' = \alpha_0 + sin^{-1}\left(\frac{\sin\delta_i}{n}\right)$. The ray angle after the m^{th} reflection is then $\alpha_m' = \alpha_0 + sin^{-1}\left(\frac{\sin\delta_i}{n}\right) + m\theta_v$, and the ray exit angle finally becomes $\alpha_{out} = \alpha_0 + \delta_i + m\theta_v = \alpha_m + \delta_i$. Thus, an angular error in the output beam is the same as the incident beam's angular error. In other words, the ray deflection angle $\Delta\alpha$ can remain unchanged when the incident beam is misaligned.

For the circular-bent light pipe case, the angular errors of output beam direction due to surface tile or beam misalignment or variation on refractive index have the same form as that in the wedge plate case. One can easily determine the angular shift of output beam by replace the wedge vertex angle θ_v as the fan angle θ_f.

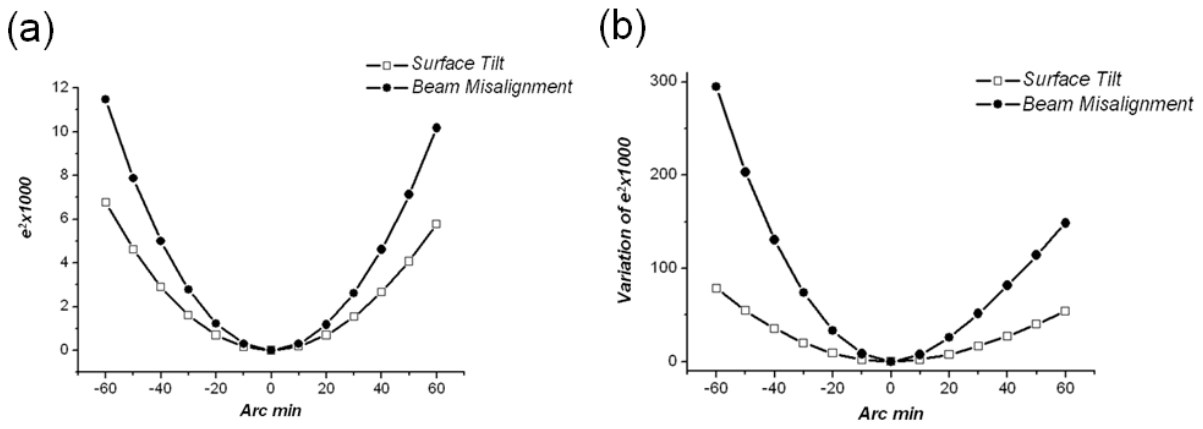

Figure 4-4-2: Investigations on performance degradation that is due to incident surface tile and beam misalignment for: (a) wedge plate; (b) circular-bent light pipe

Angular errors on incident surfaces or incident beam alignment do not seriously affect

the deflection angle (or output ray direction) in both scenarios above, but variation in the output beam's polarization state is unavoidable. The phase shift contributed by input and output surfaces, as deduced in Eq. (4-2-2), must be considered as well. Figures 4-4-2(a) and 4-4-2(b) investigate variations of the square of ellipse ratio e^2 for both the wedge plate and the circular-bent light pipe cases in previous two sections, where angular errors occur in the input surface, and incident beam alignment. The simulation results in Figs. 4-4-2(a) and 4-4-2(b) show that variations of e^2 caused by one degree of the input surface error are less than 1% (for wedge plate) and 30% (for circular-bent light pipe). The results also show the impact of one degree of misalignment in the incident beam. The impact of the incident beam misalignment is similar to that of input surface tilt.

4-5 Summary

In summary, this study proposes and numerically demonstrates that a wedge plate or a circular-bent light pipe can angularly shift a collimated beam while maintaining its polarization state. This study provides the conditions for polarization preservation and the method of estimating the system scale to allow others to design and manufacture a polarization-preserving angular shifter based on this approach. For simulation investigation, two numerical cases of different types of polarization-preserving shifters were discussed. Simulation results show that this method can indeed transfer a polarization beam into a desired angle while maintaining its polarization state. Tolerance analysis shows that the incident beam angle's angular error does not affect the deflection angle and the variation of squared ellipse ratio can be kept under 1% (for wedge plate) and 30% (for circular-bent light pipe) with 1 degree accuracy for the incident beam angle.

Polarized beams are widely used in measuring thin film, biological tissue, glass surface stress, and so forth. This study helps designers understand ray polarization behavior within dielectric-fill material and control the phase difference by properly choosing wedge or light pipe parameters. This method can easily be extended to other applications of polarization controlling mechanisms. For example, it is possible to replace the requirement of 2π total phase with another value to create a defecting phase retarder.

References

[4-1] M. L. Faupel, S. B. Bambot, T. Harrell, and A. Agrawal, "Multi-modal optical tissue diagnostic system," U.S. Patent #6975899, (2005).

[4-2] R. M. Azzam and N. M. Bashara, *Ellipsometry and polarized light*, (North-Holland, New York, 1989).

[4-3] R. M. Azzam, "Displacement of a monochromatic light beam parallel to itself without

change of polarization," Opt. Lett., **7**, 80–82 (1982).

[4-4] R. M. Azzam and M. Emdadur Rahman Khan, "Polarization-preserving single-layer-coated beam displacers and axicons," Appl. Opt., 21, 3314–3322 (1982).

[4-5] E. Cojocaru, "Polarization-preserving totally reflecting prisms," Appl. Opt., **31**, 4340–4342 (1992).

[4-6] Z. P. Wang, W. M. Sun, S. L. Ruan, C. Kang, Z. J. Huang, and S. Q. Zhang, "Polarization-preserving totally reflecting prisms with a single medium layer," Appl. Opt., **36**, 2802-2806 (1997).

[4-7] E. J. Galvez, "Achromatic polarization-preserving beam displacer," Opt. Lett., **26**, 971–973 (2001).

[4-8] A-C Hsu, C.-F. Ho, and J.-L. Chern, "Tilting tolerance analysis of a broadband polarization-preserving beam displacer", Appl. Opt., **41**, 5956-5962 (2002).

[4-9] Y.-K. Cheng and J.-L. Chern, "Polarization-preserving angular shifter," J. Opt. Soc. Am. A **25**, 1558-1563 (2008).

[4-10] Y.-K. Cheng and J.-L. Chern, "Design of a Wedge Plate for a Polarization-Preserving Angular Shifter," (Accepted by Opt. Rev.) (2009).

[4-11] M. Born and E. Wolf, *Principles of Optics*, 7th ed. (Cambridge, University, New York, 1999), pp. 42-43 and 50-51.

[4-12] E. Collett, *Polarized light: fundamentals and applications*, (Marcel Dekker. Inc., New York, 1992), pp. 139-161.

[4-13] Y.-K. Cheng, S.-N. Chung, and J.-L. Chern, "Analysis and reduction of dark zone in ultra-thin wedge plate display", J. Soc. Inf. Disp. **14**, 813–818 (2006).

[4-14] Y.-K. Cheng, S.-N. Chung, and J.-L. Chern, "Aberration analysis of a wedge-plate display system", J. Opt. Soc. Am. A, **24**, 2357–2362 (2007).

Chapter 5

Light Guide Applications on Ultra-Thin Display Systems

5-1 Motivation

Wedge plate light guide has been widely used in optical engineering [5-1]; it also has notable applications to display systems. Wedge-plate display is the projection technique which includes an optical projection engine and a thin plate with a slope, utilizing the total internal reflection (TIR) of ray inside it, to guide image on the screen. In recent years, display technology has exerted an increasing influence on human life. The primary goal of display technology development is to improve screen size and increase resolution. Cathode ray tubes (CRTs) and Liquid Crystal Displays (LCDs) are limited in screen size expandability, and plasma display panels (PDPs) have difficulty maintaining high resolutions. Only rear projection televisions (RPTVs) can simultaneously exceed a diagonal screen size of 50” and retain high definition television (HDTV) resolution [5-2]. However, RPTVs have a thickness disadvantage compared to LCDs or PDPs. An ultra-thin wedge plate display plan has made up the defect for RPTV [5-3] ~ [5-6]. From the ray propagation point of view, a wedge-plate display is a multi-mirror reflective system for which the literature [5-7] has apparently, but not actually, addressed the corresponding third order correction. This discrepancy is caused by the effective number of “mirrors” varies with the wedge-plate display incident angle.

As mentioned above, in viewing the attractive application of ultra-thin rear projector, great efforts have been developed and focused in past few years. Despite these efforts, the fundamental investigation and analysis of aberration behavior is still difficult due to the underlying large field of view (or large angles in chief ray terms). Nevertheless, this kind of analysis is necessary for technical improvement. With the purpose of establishing an

optimization design for ultra-thin wedge-plate display systems, this chapter reports verifies by simulation the aberration analysis of a wedge-plate display. This chapter also discusses significant aberration behavior features which are inherent in such wedge-plate display. One such feature is kink, which represent either the onset of dark zone in imaging or the coincidence of ray direction to the vertex.

Dark zone originates from that the reflections of output rays are different. Since the angles of source rays are continuously distributed, the ray arrives in far side of screen would have a lager angle relative to surface normal before emerging out than that in near side of screen. If ray angle before emerging out is just lager than the critical angle of wedge plate media, this ray would encounter more reflections to reduce the angle before emerging out and the exit position would have a “jump” than that of the previous one. Finally, there will be several concentric-circle-like unilluminated regions in the screen of wedge-plate display which were called “dark zones” [5-4]. Dark zone would cause the image discontinuousness and damage the brightness uniformity of wedge-plate display. In view of the potentials of wide applications of wedge-plate display, it is worthwhile to provide an analysis to explore the limitation for such a wedge plate by which dark zone can be eliminated or reduced.

On the another hand, the non-flat-panel display has highly value in commercial shows. The present technique is made by using red, green, and blue light emitting diodes (LEDs) and rotates in constant frequency, utilizing the photogene of human eyes [5-8]. The disadvantage of this method lies in using a large number of LEDs to arrange into an array, which will produce large amount of heat, and cause the decay of the luminance. At the same time, the image resolution will be restricted because the LEDs stand side by side closely. We propose a new type circular display based on the principal of wedge-plate display. It can be realized by using the technique of optical engine of RPTV in existence, and a suitable optical adaptor. In such it can solve the limitation of image resolution and reduce power consumption and heat of display. Above work had also been published in academic papers [5-9] ~ [5-11].

5-2 Aberration Analysis of Wedge Display System

Basic Formulation of Ray Tracing

Referring to Fig. 5-2-1, the entrance angle of ray from a source, which was denoted by a grid of field points, essentially determines the distance traveled by the ray in the wedge plate. This also implies that the entrance angle of ray can be converted to the exit position of ray on the screen as to be shown below. Therefore, by controlling the entrance angle of ray, one can guide the ray to a desired position on the screen and hence, enhance display quality. It would be worthwhile to emphasize that even without imaging optics; the grid of field points can still form the image over the exit port of the wedge plate, i.e., the upper screen, provided the ray is well limited to some specified emitted angle.

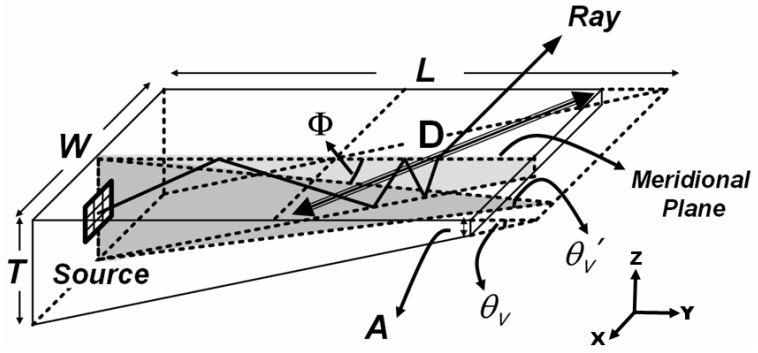

Figure 5-2-1 Schematic diagram of a wedge plate display where *D* is the length of screen diagonal.

Basically, when one ray propagates inside the wedge plate, if the reflective angle does not reach to the critical angle, the ray will encounter a total internal reflection (TIR) by which the interface between the plate and air would act as a mirror, and the corresponding reflected angle will decrease gradually until it reaches the critical angle such that the ray exits away from the plate. To deduce the relation between entrance angle and emergent position, Travis and Zhong assumed that ray enters into wedge plate with an incident angle θ_i would exit the plate at a position *X* and the exit angle θ_o is the same with the critical angle of wedge plate θ_C, and hence, the relation follows $\sin\theta_i = \dfrac{X \cdot \cos\theta_C}{L}$, where *L* is the side length of

wedge plate, as shown in Fig. 5-2-2(a) [5-5]. However, the exit angle does not have to equal the critical angle: the ray would exit the wedge plate even when the reflective angle is smaller than the critical angle because of *finite* vertex angle of wedge plate. In other word, the formula in prior work [5-5] works for specific case and has to be reconsidered.

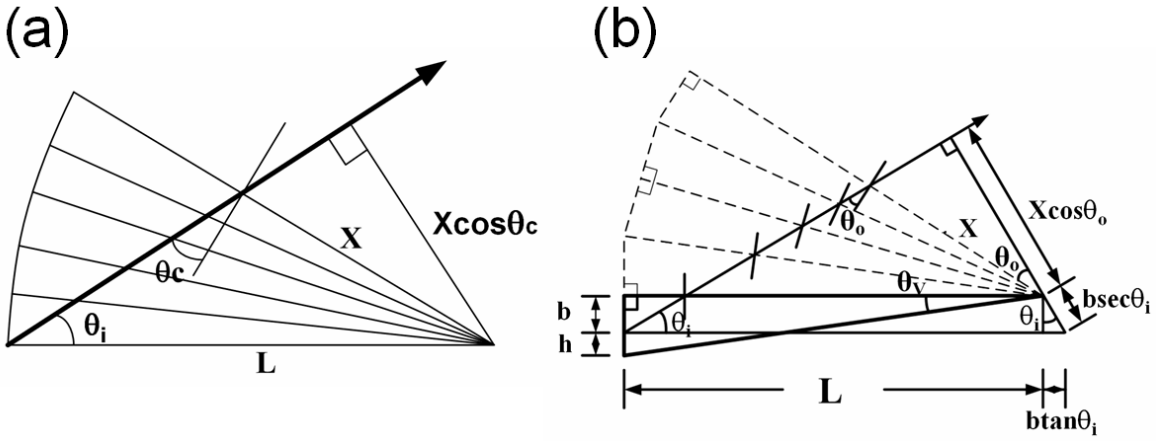

Figure 5-2-2 Schematic diagram of ray propagation: (a) a virtually-folded wedge plate and (b) a virtually-folded wedge plate with non-zero entrance height.

Let us assume that one ray propagated inside the wedge plate and finally exited away from the upper side of the wedge plate, then the times of reflections could be denoted as *2m*, and the exit angle follows $\theta_o = 90^\circ - \theta_i - 2m \cdot \theta_V$, where θ_V is the vertex angle of wedge plate. When the exit angle θ_o is slightly smaller than the critical angle θ_C, the corresponding incident ray will have the same number of reflections, and $m = ceiling[\frac{90^\circ - \theta_i - \theta_C}{2 \cdot \theta_V}]$ approximately, where *ceiling* is a function that gives the nearest integer value that lager than the exact value (e.g., $ceiling[\pi]$=4). With these considerations, we have

$$\sin\theta_i = \frac{X \cdot \cos\left\{90^\circ - \theta_i - 2 \cdot ceiling[\frac{90^\circ - \theta_i - \theta_C}{2 \cdot \theta_V}] \cdot \theta_V\right\}}{L}, \qquad (5\text{-}2\text{-}1)$$

which specifies the required entrance angle θ_i for some specific *X*. Referring to Fig. 5-2-2(b), if ray enters the wedge plate at a height *h*, Eq.(5-2-1) can be rewritten as

$$\sin\theta_i = \frac{X\cdot\cos\left\{90^\circ-\theta_i-2\cdot ceiling\left[\frac{90^\circ-\theta_i-\theta_C}{2\theta_V}\right]\cdot\theta_V\right\}+b\cdot\sec\theta_i}{L+b\cdot\tan\theta_i}, \qquad (5\text{-}2\text{-}2)$$

where b is the height of the incident ray at entrance and the wedge thickness of entrance port is $b+h$. Equations 5-2-1 and 5-2-2 are the basic formulas of ray tracing in wedge plate.

When a skew ray is incident along the non-meridional direction of wedge plate, the corresponding (effective) vertex angle θ_V' would be small than the original θ_V, as seen in Fig. 5-2-1, and follows $\theta_V' = \tan^{-1}(\tan\theta_V\cos\Phi)$ where Φ is the angle between the meridional and non-meridional planes. Therefore, to have the ray-tracing formula of non-meridional ray, one could simply replace θ_V of Eq.(5-2-2) by θ_V'. Equations (5-2-1) and (5-2-2) and their extensions provide the complete formulas of ray tracing for wedge plate and hence, a base for the analysis of the formation of dark zone and display quality without additional imaging optics.

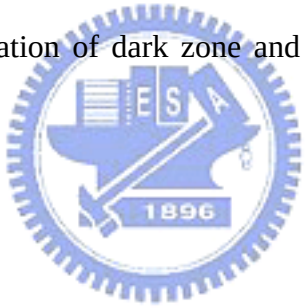

Aberration Analysis

Eq. (5-2-2) describes basic behavior of ray propagating in wedge plate. For further illustration, when ray propagated in the meridional plane, Eq. (5-2-2) can be rewritten as

$$x = \frac{(L+b\cdot\tan\theta)\cdot\sin\theta - b\cdot\sec\theta}{\cos\left[90^\circ-\theta-2*ceiling\left[\frac{90^\circ-\theta-\theta_c}{2\theta_V}\right]*\theta_V\right]}, \qquad (5\text{-}2\text{-}3)$$

And when a skew ray is incident along the non-meridional direction of the wedge plate, the ray-tracing formula should be

$$x = \frac{(L+b\cdot\tan\theta)\cdot\sin\theta - b\cdot\sec\theta}{\cos\left[90^\circ-\theta-2*ceiling\left[\frac{90^\circ-\theta-\theta_c}{2\tan^{-1}(\tan\theta_V\cos\Phi)}\right]*\tan^{-1}(\tan\theta_V\cos\Phi)\right]} \qquad (5\text{-}2\text{-}4)$$

where Φ is the angle between the meridional and non-meridional planes.

Next we explain the wedge plate aberration form. Referring to Fig. 4-2-3(a), if an object with height *h* and distance *d* emits one ray into the wedge plate at aperture height ρ, the ray angle after entering wedge is

$$\theta_i = \sin^{-1}[\frac{\rho - fp*h}{n\sqrt{d^2 + (\rho - fp*h)^2}}] \qquad (5\text{-}2\text{-}5)$$

Substituting this equation into Eq.(5-2-3) produces the actual exit location of this ray in the wedge screen, based on system parameters. However, some exceptions must be noted in practical situations. Figure 5-2-3(b) shows that when the entrance angle θ is smaller than vertex angle θv (even $\theta < 0$), the ray will touch the bottom surface of the wedge plate first. This situation assumes that the ray is emitted from a virtual source location *A* which is separated from the top of entrance port by distance *b'*, and the entrance angle should be adapted to $2\theta v - \theta$. By trigonometry,

$$b' = b + \frac{h_1}{\tan\theta_V - \tan\theta} \cdot [\tan(2\theta_V - \theta) - \tan\theta] \qquad (5\text{-}2\text{-}6)$$

With this assumption, Eq. (5-2-3) is suitable for all practical rays emitted outside the wedge plate.

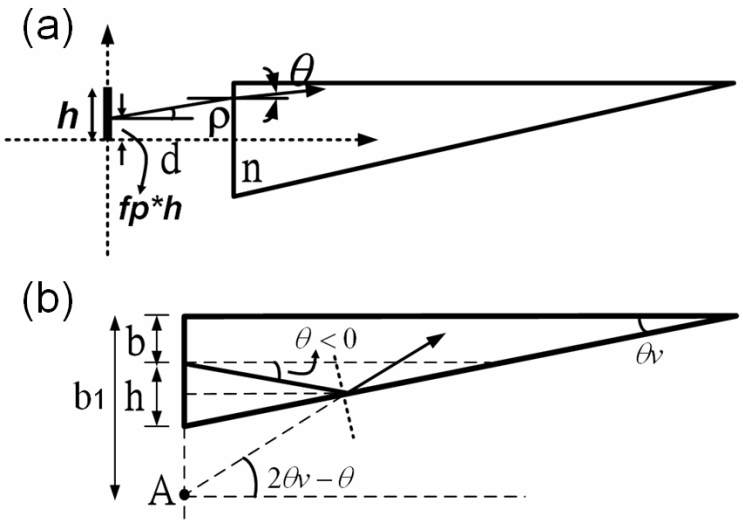

Figure 5-2-3 (a) Schematic diagram of a ray emitted from a finite size object; (b) Schematic diagram when ray incidents to bottom of wedge

The ideal location for a ray in the screen should be the emitting position (height) multiplied by the corresponding magnification. For example, if the system magnification is *m*, the object height is *h*, and the ray is emitted from field point *fp*, then the ideal exit location in the wedge screen should be

$$X_{perfect} = (1 - fp) \cdot m \cdot h \qquad (5\text{-}2\text{-}7)$$

For an optical system, the aberration is the deviation between the ideal and real locations. The following formula can identify the aberration D_x of the wedge plate:

$$\begin{aligned} D_x &= x_{real} - x_{perfect} \\ &= \frac{(L + b \cdot \tan\theta) \cdot \sin\theta - b \cdot \sec\theta}{\cos\left[90^\circ - \theta - 2 * ceiling\left[\frac{90^\circ - \theta - \theta_c}{2\theta_V}\right] * \theta_V\right]} - (1 - fp) \cdot m \cdot h \end{aligned} \qquad (5\text{-}2\text{-}8)$$

Equation (5-2-8) can determine the aberration relative to different ray locations on entrance port for some particular wedge systems. Consider an illustration with object height *h*=1, object distance *d*=10, aperture height *T*=5 and the refractive index of wedge plate *n*=1.51872 (BK7) for a 50-inch wedge plate display, *L*= 62.25 and w=43.578 inches. In this study, the aberration curve in field points h=0.0, 0.7, and 1.0 were sketched by Mathematica.

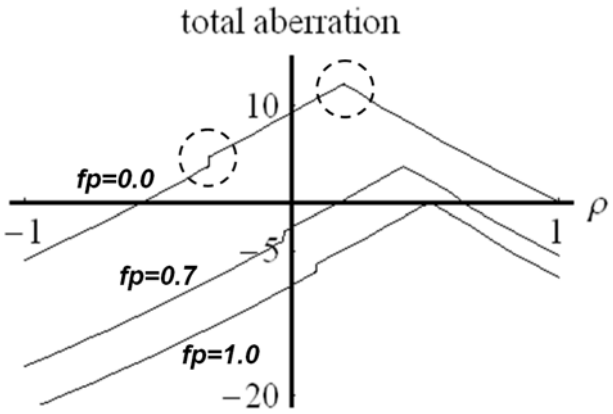

Figure 5-2-4 Analytical result of total aberration plots of the wedge-plate display

Contrary to the generally accepted concept of aberration theory, the results in Fig. 5-2-4 show that the ray intercept curve exhibits non-differential characteristics, i.e., kink-like features, as the signature of aberration behavior for wedge-plate type displays. The onset of this kink-like signature is linked to the appearance of the imaging dark zone. The dark zone was

excited because the finite vertex angle which is inevitable in wedge-plate displays [5-4] [5-10].

The following contains a short summary of the physical mechanism, i.e., the dark zone for completeness. The dark zone is caused by different output ray reflections. The distribution of emerging ray positions "jumps" where the emerging angle is equal to the critical angle of the wedge plate, and the reflection number increases after each "jump." The dark zone affects image quality and the brightness uniformity of the wedge-plate display. The analysis and reduction of dark zone will be discussed in the next section.

Numerical Verification

Ray tracing can be performed by using TracPro. We build a dielectric-filled wedge plate, laying on the z-axis, with a 50 inch diagonal screen length, 5 inch wedge thickness, length of 62.25 inch, width of 43.578inch, and refractive index n=1.51872(BK7). The bottom surface produces 100% reflection so that rays can only leave the wedge from the upper side. Other surfaces produce 100% transmittance to prevent ghost image formation by Fresnel loss, while still retaining total internal reflection. Figure 5-2-3(a) shows an object with height $h=1$ placed in front of the wedge plate at distance $d=10$. Figure 5-2-5 shows the tracing from $\rho=-1$ to $\rho=1$ (with normalization) for the field point h=0.0 at the meridional plane.

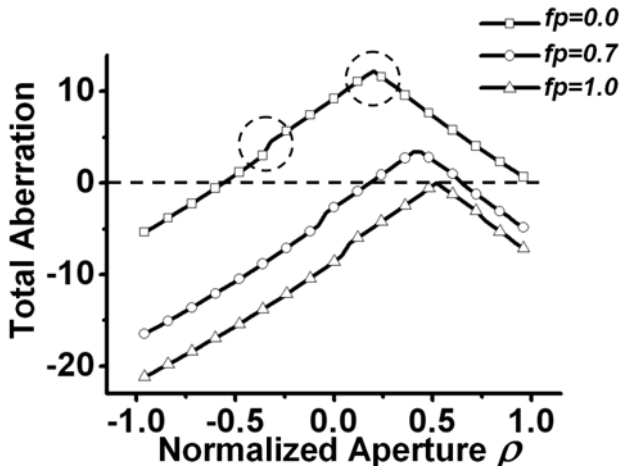

Figure 5-2-5 Simulation result of total aberration plots of the wedge-plate display

Dark zones obviously exist, as indicated by the dashed circle in Fig. 5-3-3. Equation (5-2-8)

shows that the aberration can be calculated from practical position to the ideal location for each ray, and Fig. 5-2-5 shows that the ray tracing was also extended to another two field points h=0.7, and 1.0. The simulation results show precise conformity to the analytical results. Comparing the top bend and the non-continuous kink-like feature caused by the dark zone in three field points with Fig. 5-2-4 shows that Eq. (5-2-8) is highly accurate.

Third-Order Aberration Coefficients

Without loss of generality, a Taylor series expansion can be made for the aberration along the meridional plane. The leading terms of the third-order aberration are listed below:

$$\begin{aligned} D_x = {} & a_0 + a_1 h + a_2 \rho \\ & + a_3 h^2 + a_4 \rho^2 + a_5 \rho h \\ & + a_6 h^3 + a_7 \rho^2 h + a_8 \rho^3 + a_9 \rho h^2 + ... \end{aligned} \qquad (5\text{-}2\text{-}9)$$

where a_0, a_1, a_2….are the corresponding coefficient terms listed in increasing order. According to the method in last section, the curves of a_1 to a_9 terms where field points are 0, 0.7, and 1.0, are sketched as shown in Figs. 5-2-6(a)~5-2-6(i).

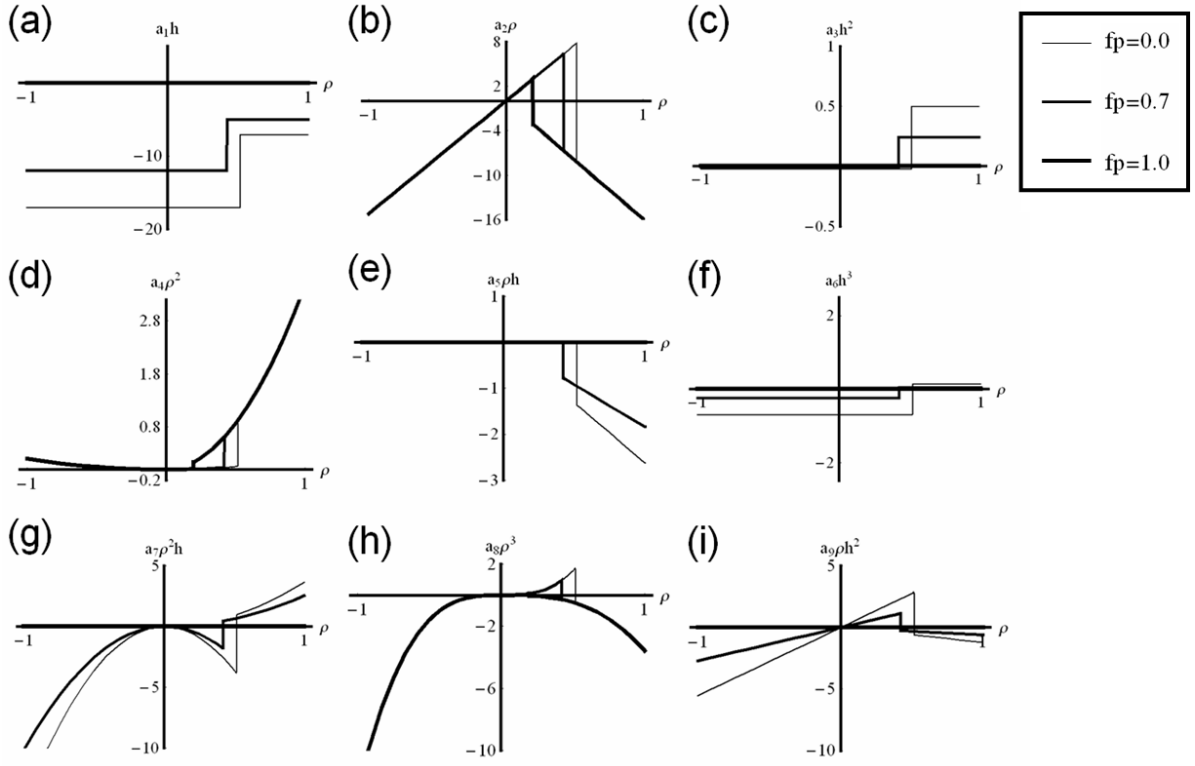

Figure 5-2-6 (a)-(i) Aberration plots of the first three-order terms of the wedge-plate display.

These graphs reveal that each term in Eq. (5-2-9) as a non-continuous reverse curve located at the same ρ value as the top bend in Fig. 5-2-5. The $a_4\rho^2$ and $a_8\rho^3$ terms correspond to the traditional spherical aberration; the $a_7\rho^2 h$ term corresponds to coma; the $a_9\rho h^2$ term corresponds to astigmatism; $a_4\rho^2$ and $a_8\rho^3$ terms correspond to distortion; the $a_5\rho h$ term belongs to second order aberration, and is difficult to refer to as regular aberration. Table 5-2-1 lists a few leading aberration coefficient items.

Table 5-2-1 Aberration coefficients

a_1	$-fpm+\frac{fpCsc(2\theta_c Ceiling\Theta)}{\mathrm{d}n}(L+(1-Ceiling'\Theta)Cot(2\theta_c Ceiling\Theta))$
a_2	$\frac{Csc(2\theta_2 Ceiling\Theta)}{\mathrm{d}n}(-\mathrm{d}n+L-(1-Ceiling'\Theta)Cot(2\theta_V Ceiling\Theta))$
a_3	$\frac{fp^2Csc(2\theta_V Ceiling\Theta)}{\mathrm{d}^2n^2}\left(-\frac{1}{2}+LCot(2\theta_V Ceiling\Theta)(1-Ceiling'\Theta)+Cot^2(2\theta_V Ceiling\Theta)+\frac{1}{2}(1-Ceiling'\Theta)^2+\frac{Cot(2\theta_V Ceiling\Theta)Ceiling''\Theta}{4\theta_V}\right)$
a_4	$\frac{Csc(2\theta_V Ceiling\Theta)}{\mathrm{d}^2n^2}\left(-\frac{1}{2}+(\mathrm{d}n+L)Cot(2\theta_V Ceiling\Theta)(1-Ceiling'\Theta)+Cot^2(2\theta_V Ceiling\Theta)(1-Ceiling'\Theta)^2+\frac{1}{2}(1-Ceiling'\Theta)-\frac{Cot(2\theta_V Ceiling\Theta)Ceiling''\Theta}{4\theta_V}\right)$
a_5	$\frac{fpCsc(2\theta_V Ceiling\Theta)}{\mathrm{d}^2n^2}\left(1-(1-Ceiling'\Theta)(\mathrm{d}n+2L)Cot(2\theta_V Ceiling\Theta)+\mathrm{d}n(1-Ceiling'\Theta)(2Cot^2(2\theta_V Ceiling\Theta)+1)+\frac{Cot(2\theta_V Ceiling\Theta)Ceiling''\Theta}{2\theta_V}\right)$
where	$\Theta=\frac{90^\circ-\theta_c}{2\theta_V}$

Figure 5-2-7 outlines the sum of the first three-order approximation of aberration for a 50-inch wedge plate, where the wedge parameters are the same as those in simulation. In this numerical example, the third-order aberration approximation corresponds well with the total aberration. This provides a useful guideline in designing the display. Referring to Fig. 5-2-7, two angular solutions with zero aberration corresponding to Case 1 (Fig. 5-2-3(a))

and Case 2 (Fig. 5-2-3(b)) would be found for each field point. The advantage of aberration analysis is that it can determine the best emitting angle for each field point of object.

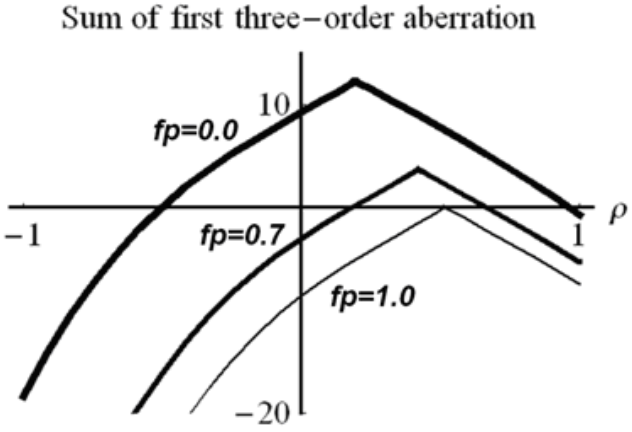

Figure 5-2-7 Sum of the first three-order aberration.

Wedge Parameter Analysis

Adjusting wedge plate parameters can minimize aberration and optimize image quality. To this end, the aberration of the 50-inch wedge is deconstructed as a function of the wedge vertex angle θv and refractive index n for the same incident position $\rho=0$, as shown in Figs. 5-2-8(a) and 5-2-9(a). The field point fp=0.7 was chosen in this representative case. The results indicate that it can be difficult to efficiently reduce aberration during the discussing range. This study assumes rays incident through entrance pupil center ($\rho=0$). As long as the field point fp is selected, the traced ray angle is also determined. This angle may have large discrepancy with the ideal incident angle, and cause a lot of aberration. It is hard to eliminate aberration using only the system parameters (refractive index n, wedge vertex angle θv, etc.). In another words, determining a good initial condition is a perquisite to wedge optimization.

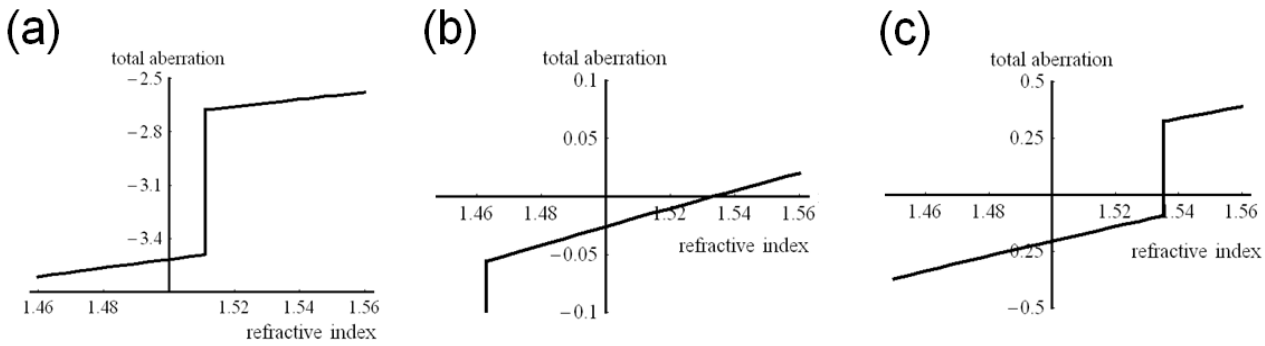

Figure 5-2-8 Aberration plots with variable *n*: (a) when ρ=0; (b) when ρ=0.18; (c) whenρ=0.65.

According to Fig. 5-2-4, when a ray emits from field point *fp* =0.7, less aberration will occur when rays pass through ρ=0.18 and ρ=0.65. The analysis for the refractive index *n* is reconfirmed with these two incident angles, as shown in Figs. 5-2-8(b) and 5-2-9(c). These results show that the aberration would equal zero if the refractive index *n* was about 1.535. While *n* varies from 1.5 to 1.55, the aberration fluctuates smoothly in Fig. 5-2-8(b) and rapidly in Fig. 5-2-8(c). This shows that the two zero-aberration initial designs would have different refractive index tolerance, and the analysis in this study can help select the better one. The relation between aberration and the wedge vertex angle θv when rays emit from *fp*=0.7 and pass through ρ=0.18 and ρ=0.65 can also be plotted by the same method. Figures 5-2-9(b) and 5-2-9(c) show the results.

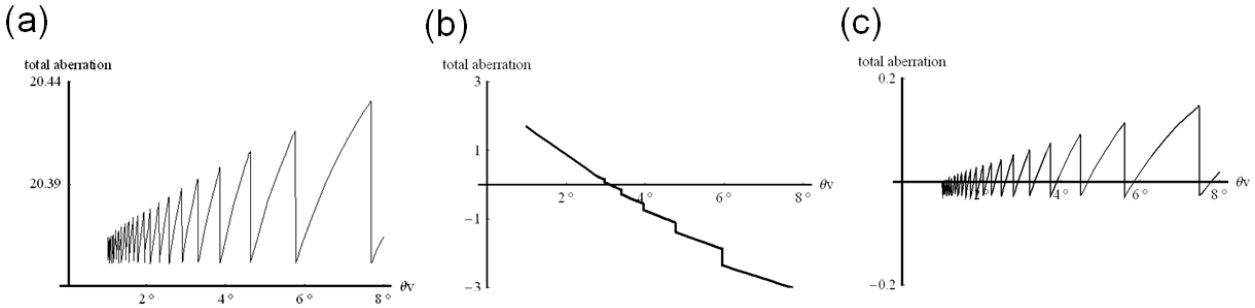

Figure 5-2-9 Aberration plots with variable θv : (a) when ρ=0; (b) when ρ=0.18; (c) whenρ=0.65.

5-3 Analysis and Reduction of Dark Zone in Wedge-Plate Display

Formation of Dark Zone

As illustrated in the precious section, it is possible to form the image of a grid of field points by the wedge plate even without any additional imaging optics, provided that the emitted angles of each field point can be well controlled. Two plates of apertures can achieve such a controlling, though it is not efficient. However, image blur is inevitable generally. Furthermore, the imaging quality is also limited by the appearance of dark zone. The origin of dark zone has to be clarified for further utilization of wedge plate in display.

Physically, the formation of dark zone is due to the numbers of reflection are different when the exit angle θ_o is slightly lager or smaller than the critical angle θ_c. In short, once a *finite*-vertex-angle wedge plate is used, the appearance of dark zone is inevitable. Referring to Fig. 5-3-1, one ray enters wedge plate by θ_i and exits by an angle θ_{c-} which is slightly less than the critical angle θ_c after being reflected by $2m$ times. Considering that if θ_i becomes slightly smaller, the ray would be reflected by $2(m+1)$ times and the exit angle should be θ_{c+}-$2\theta_v$ where θ_{c+} is slightly larger than the critical angle θ_c.

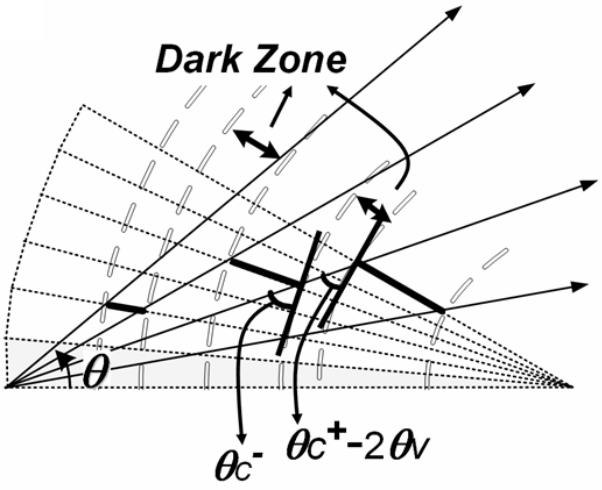

Figure 5-3-1 Dark-zone ranges of a wedge plate display

After some algebraic manipulations of Eq. (5-2-1) and (5-2-2), the dark zone boundary that correlated to $2m^{th}$ times TIR follows

$$\frac{(L+b\cdot\cot\Theta_m)\cdot\cos\Theta_m - b\cdot\csc\Theta_m}{\cos(\theta_C-2\theta_v)} < X < \frac{(L+b\cdot\cot\Theta_m)\cdot\cos\Theta_m - b\cdot\csc\Theta_m}{\cos\theta_C}, \quad (5\text{-}3\text{-}1)$$

and the width of the corresponding dark zone follows

$$\Delta X_{2m} = \frac{(L+b\cdot\cot\Theta_m)\cdot\cos\Theta_m - b\cdot\csc\Theta_m}{\cos\theta_C} - \frac{(L+b\cdot\cot\Theta_m)\cdot\cos\Theta_m - b\cdot\csc\Theta_m}{\cos(\theta_C-2\theta_v)}, \quad (5\text{-}3\text{-}2)$$

where $\Theta_m = \theta_C + 2m\theta_V$. Equations (5-3-1) and (5-3-2) are the basic formulas for the formation of dark zone.

With the resolution of human eye, Eq. (5-3-2) provides a basic design criterion for wedge-plate display. Practically, for display application, the width of dark zone should be less than α**d*, where *d* is the distance from the audience to the screen and angle α is the angular resolution of human eye. Typically, the resolution limit of human eye is one minute of arc [5-12].

Simulation Verification

As a real exploration, also referring to Fig. 5-2-1, we consider a wedge plate where the plate length and width are *L*=17.43 and *W*=12.2 inches, respectively, the thickness of entrance port *T*=0.7, the thickness of exit port *A*=0.197 inches, and the vertex angle θ_V is 1.653°. The plate material is Acryl with *n*=1.49309. The corresponding screen's diagonal is ~14 inches because only half of the area of wedge plate is used as the display screen. Effectively, the ratio of display's thickness and screen's diagonal length is ~1:20.

In analysis, the source was assumed on the meridional plane and located at the bottom of entrance port, i.e. *b*=0.7 inches (and *h*=0). The ray tracing was also performed by TracePro. For simplification, the bottom surface of wedge plate is with 100% reflection such that the ray can only leave the plate from the upper side, while the upper surface is with 100% transmission. Simulation is separated into twofold: one for a comparison of analytical result and the other for experimental observation.

For the comparison of the analytical result of meridional plane, a two-dimensional

Lambertian point source was defined as a grid source lying vertically, i.e., on the y-axis; each ray, emitted from the same point, but with a different angle θ, carried a flux $\cos\theta$. Each angular displacement is 0.01°; hence there are 9,001 rays from 0° to 90°. A Lambertian point-like source was also traced in three-dimensional space. As shown in Fig. 5-3-2(a), simulation shows that the dark zones existed and the result of simulation is closely related to that of analytical result as identified in Table 5-3-1. Meanwhile, it can be verified from Eq.(5-3-2) that the width of dark zone reduced as the times of reflection *2m* increases. The differences between the results of simulation and analysis were caused by the finite-resolution setting of source and rays in simulation as depicted above.

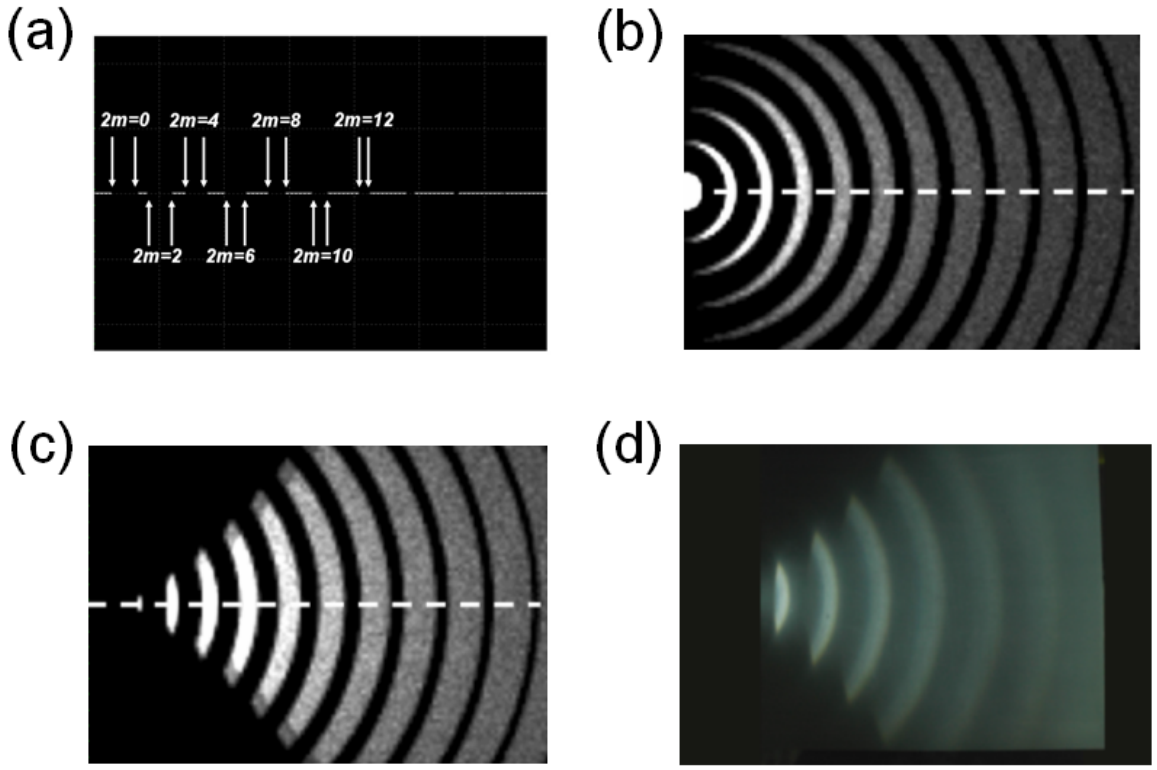

Figure 5-3-2 Dark-zone formation of a 14-inch wedge plate: (a) simulation along the meridional plane; (b) and (c) are the simulations of three-dimensional case where the source is placed at right outside and inside the entrance port of wedge plate respectively; (d) Experimental result with a Lambertian LED source.

In the simulation of three-dimensional case, it is worthwhile to compare the results that the source was placed either right outside and inside the wedge plate. The results are shown

in Figs. 5-3-2(b) and 5-3-2(c) in which the meridional plane is denoted by dashed line and concentric characteristics can be identified for both. When rays were emitted from a position inside the wedge, the entrance angles is ranged from 0° to 90°; while from a position outside the wedge, the entrance angles is ranged from 0° to the critical angle (42.051°), resulting in a smaller illuminated area as shown in Fig. 5-3-2(c). However, the boundaries of dark zone are the same because the vertex angles and refractive indices are the same, respectively, for the cases of simulation and analysis.

Experimental Exploration

Next, we can take a real experiment where the source is placed outside for further discussion. A corresponding Acrylic 14-inch wedge-plate display was made and a Lambertian white-light emitting diode (Lumileds, model PW-09) was used for the light source. The output image from wedge screen was capture by a commercial digital camera (Nikon, model D70) as shown in Fig. 5-3-2(d) where concentric characteristics that are very similar to that of simulation can be seen. The profiles were further processed by MatLab to determine the dark-zone boundaries and widths, and the result was included in Table 5-3-1. One can see that correspondence between experiment and theoretical exploration is in a good degree of consistence.

Table 5-3-1 Analytical, simulation, and experimental results of dark zone.

Number of reflections ($2m$)	Entrance angle (°)	Width of dark zone (unit: inches)		
		analytical	simulation	experiment
4	41.34	1.0003	1.0165	0.95
6	38.03	0.9292	0.9570	0.88
8	34.73	0.8508	0.8904	0.81
10	31.42	0.7778	0.8206	0.68
12	28.12	0.6981	0.7480	0.59

It can be seen that there are still some differences between the experiment and the

analysis. The origins can be attributed to two causes: (1) the LED source is with finite size and wide band of wavelength. Hence, the observed dark zone is composed by the dark zone patterns of infinite point sources from different emitted positions with different wavelengths, which cause a blur of image and a width reduction of dark zone. (2) Ray leakage due to imperfectly polished wedge surface, which affects the estimate of dark zone boundaries and reduces the width.

Reduction of Dark Zones

From above discussions, one can see the appearance of dark zone in the wedge plate display looks natural. Equation (5-3-2) indicates that for a point source, there must exist dark zone, unless the wedge vertex angle θv reduces to zero. But according to Eq.(5-2-1), zero θv would cause infinite reflections, i.e., ray will always be trapped inside the wedge plate. Nevertheless, it is possible to eliminate as to be shown below. Namely, they could be achieved by either correcting the surface or rearranging the source pattern.

A. Surface Correcting

Referring to Fig. 5-3-3, on the exit surface of the wedge plate, dark regions and bright regions will appear alternately. As illustrated in section 3, the ray angles relative to the surface normal of exit surface before and after $2m^{th}$ dark zone are θ_{c^-} and $\theta_{c^+} - 2\theta_V$, where θ_{c^-} (θ_{c+}) is $\theta_c - \delta\theta$ ($\theta_c + \delta\theta$), and $\delta\theta$ is a tiny angle. If we extend both ray paths after refracting out, we found these two rays will intersect at one point P_{2m}. By Snell's law and simple manipulation of algebra, the location of P_{2m} follows

$$P_{2m}(x,h) = (X_{2m}^{R} + t,\ t \cdot \tan\beta), \qquad (5\text{-}3\text{-}3)$$

where $t = \dfrac{(X_{2m}^{R} - X_{2m}^{L}) \cdot \tan\alpha}{\tan\beta - \tan\alpha}$, $\alpha = \cos^{-1}[n\sin(\theta_c - \delta\theta)]$, $\beta = \cos^{-1}[n\sin(\theta_c + \delta\theta - 2\theta_v)]$,

and X_{2m}^{R} (X_{2m}^{L}) is the right (left) dark zone boundary in Eq. (5-3-1) respectively.

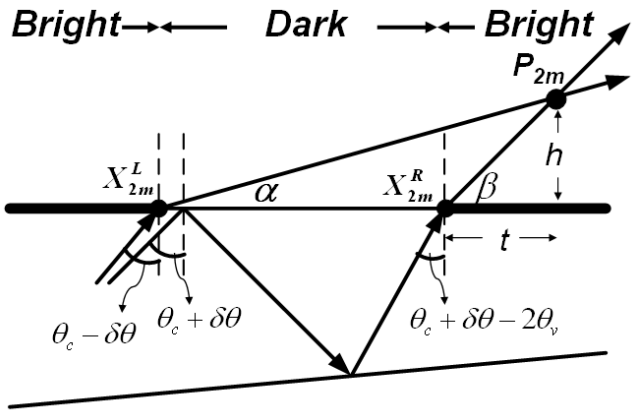

Figure 5-3-3 Ray intersection after emerging from the wedge surface.

As a numerical demonstration, we select $\delta\theta$ =0.5º, for a 52 inch screen diagonal wedge with plate length L = 64.96, plate width W=45.67, and entrance port thickness T=1.53 inches. The vertex angle θ_V is 1°. Then we solve different locations of P_{2m}. The trajectory of locations forms a no-dark-zone corrected surface which can be fitted as a straight line, as shown in Fig.5-3-4(a). Figure 5-3-4(b) shows the irradiance profile on the wedge exit surface and the new corrected surface. One can see the discontinuous irradiance (dark zone) on the wedge exit surface had been connected as we expected. The non-uniform irradiance on the corrected surface can be improved by redistribute the ray interval on it. In other words, we can rewrite the function relation of Eq. (5-2-1) from $\theta \rightarrow X$ (on the wedge exit surface) to $\theta \rightarrow X'$ (on the corrected surface), then calculate the requisite angles to get a uniform irradiance distribution.

For non-meridional direction, we only have to convert the rectangular coordinate (X,Y) in Fig. 5-2-1 into a circular coordinate (R,Φ), and modify the vertex angle in the non-meridional direction by $\theta_V' = \tan^{-1}(\tan\theta_V \cos\Phi)$. Figure 5-3-3(c) shows an example of a two-dimensional corrected surface of a 52-inch wedge plate, where Φ is ranged from 0º to 90º and each angular displacement is 10°. Note that the surface slope will alter for different Φ so the whole surface is not planer. However, when the vertex angle is small, the corrected surface can be approximated by a flat plane. On the other hand, due to the

symmetry, the negative Φ portion would have a mirrored shape.

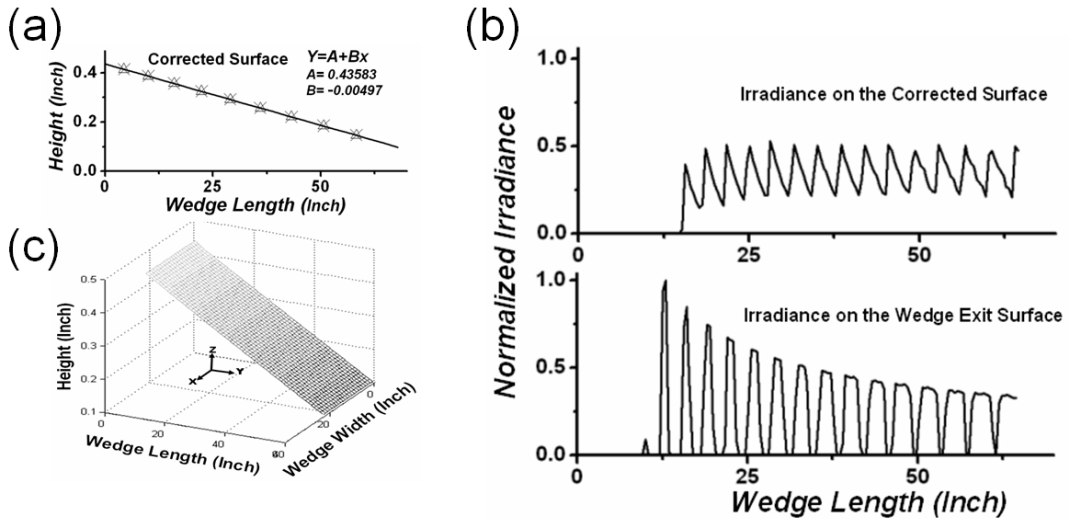

Figure 5-3-4 (a) The curve of the corrected surface on the meridional plane; (b) irradiance at the corrected surface and the wedge exit plane; (c) an entire geometry of the corrected surface

B. Source-Pattern Rearranging

In reality, the projected source object has finite size. Referring to Fig. 5-2-2(b), rays emitted from different field point of the object which correspond to an individual b in Eq.(5-2-2) would result in different dark zone distribution. So additional variable b can provide a more effective way to have continuous ray locations distributed on the wedge exit surface than that provided by the corrected surface method. Mathematically, solution sets of (b,θ) for some specific X are infinite. By utilizing a digital image panel and a suitable micro-lens array, our proposal can be realized. Each pixel on the digital panel stands for one b value and the micro lens element guides the chief ray of the pixel into an expected direction. Therefore, the choice of solution set of (b,θ) for specific X would be limited by the following two conditions: (1) The value of b is discrete and is separated by the pixel interval; (2) The assignment of b cannot be repeated for different X. Table 4-3-2 lists one group of solution sets of (b,θ) for the 52 inch wedge. The range of b (source panel height) is 0.5 inch and is divided into ten equal parts.

Table 5-3-2 Rearranged ray parameters

Start Height ($b_{\#}$) (inchs)	0.05 (b_1)	0.10 (b_2)	0.15 (b_3)	0.20 (b_4)	0.25 (b_5)	0.30 (b_6)	0.35 (b_7)	0.40 (b_8)	0.45 (b_9)	0.50 (b_{10})
Entrance Angle (degrees)	26.52	15.16	23.18	22.04	13.42	18.95	17.13	19.93	23.92	15.94
Exit Position ($X_{\#}$) (inchs)	40.0 (X_1)	60.0 (X_9)	45.0 (X_3)	47.5 (X_4)	62.5 (X_{10})	52.5 (X_6)	55.0 (X_7)	50.0 (X_5)	42.5 (X_2)	57.5 (X_8)

A two-dimensional demonstration was shown in Figs. 5-3-4(a) and 5-3-4(b), which neglected the variation of Φ. From the result, one can see that dark zone has been eliminated.

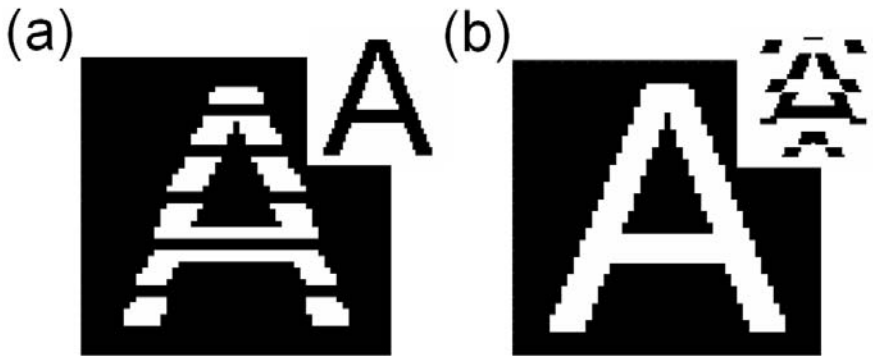

Figure 5-3-5 (a) An original source pattern and the projected result (with dark zone); (b) a rearranged source pattern and the projected result (without dark zone)

5-4 Wedge Type Circular Display

According to Eqs. (5-2-2), we can control the projected image take advantage of incident ray angle. If we rotate the meridional plane along a fixed axis, we can get a circular hollow cylinder which any vertical cross section is a wedge plane, as shown in Fig. 5-4-1.

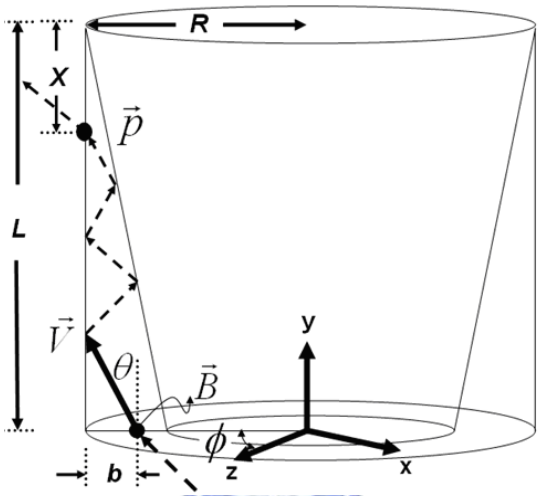

Figure 5-4-1 Schematic diagram of ray propagates in the meridional plane of a wedge-plate display

Rays propagate in any tangent plane will in accordance with Eq. (5-2-2), as long as we extend the equation from two-dimension to three-dimension. Referring to Fig. 5-4-1, we can rewrite Eq. (5-2-2) as

$$\vec{V} = f(\vec{P}, \vec{B}) \qquad (5\text{-}4\text{-}1)$$

where

$\vec{V} = (\sin\theta\cos\phi,\ \cos\theta,\ \sin\theta\sin\phi)$ is the ray direction after entering wedge cross plane,

$\vec{P} = (L - X)(\cos\phi,\ 1,\ \sin\phi)$ is the ray location on cylinder surface,

$\vec{B} = (R - b)(\cos\phi,\ 0,\ \sin\phi)$ is the ray incident position on cylinder bottom.

According to Eq. (5-4-1), we can calculate the required angles for any figure on cylinder image surface, at this time the image source forming a ring-type incident positions.

Numerical Verifications

We utilize TracePro to verify the above idea. First we build up a wedge cross-section cylinder, and make the screen wide to length ratio as 4:3, and set the picture width as 1/3 of cylinder circle, as shown in Fig. 5-4-2.

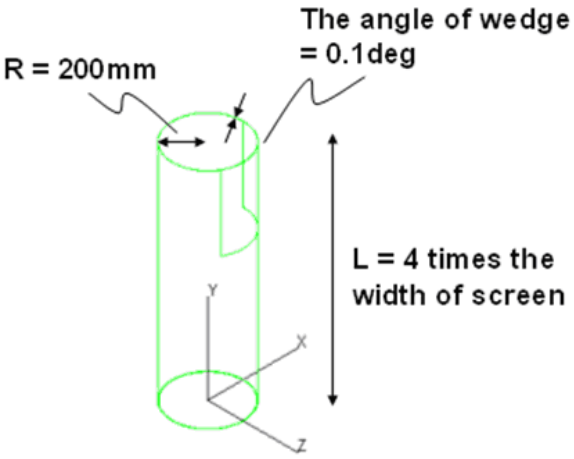

Figure 5-4-2 System parameters of a cylindrical wedge

The radius of cylinder is 200mm, the wedge vertex angle is 0.1°, the length of cylinder is 4 times of screen wide (about 1675.5mm), and the material is Acrylic. We select *"NCTU IEO"* words as the test pattern (or one can regard it as the ideal position of image formation), as shown in Fig. 5-4-3(a). Utilizing Mathematica, we project the test pattern to the output of cylinder and calculate the position of each pixel, as shown in Fig. 5-4-3(b).

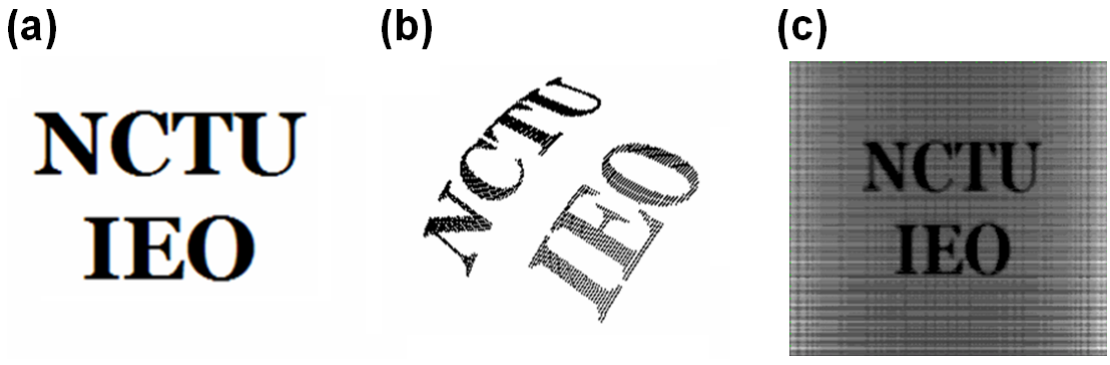

Figure 5-4-3 Simulation verification for cylindrical wedge: (a) original image; (b) when image projects on cylinder surface; (c) simulation results.

According to Eq. (5-4-1), we calculate the required incident positions and angles for rays to

propagate to each selected pixel, then convert it into TracePro light source format. Fig. 5-4-3(c) shows the result when this source incident into wedge type circular display by a non-sequential ray tracing. Compare to Fig. 5-4-3(a), one can find that Eq. (5-4-1) has highly accuracy.

The simulation result above is a simple black-and-white figure. Next, we take a color BMP picture to verified the actually behavior of wedge type circular display. The pixel resolution of our selected picture is 400*300, as shown in Fig. 5-4-4(a). According to Eq. (5-4-1), we calculate the required incident positions and angles for rays in each pixel on the picture to propagate to the ideal location. Unlike above section, due to this picture is color one, each pixel in object space emits three rays, include red, green, and blue; each color has 256 intensity step to recombined a desire color. Figure 5-4-4(b) shows the simulation result. There will be different refractive angles when rays incident into wedge type circular display due to their different wavelength, and result in small imprecision on image pattern, this is also called color shift.

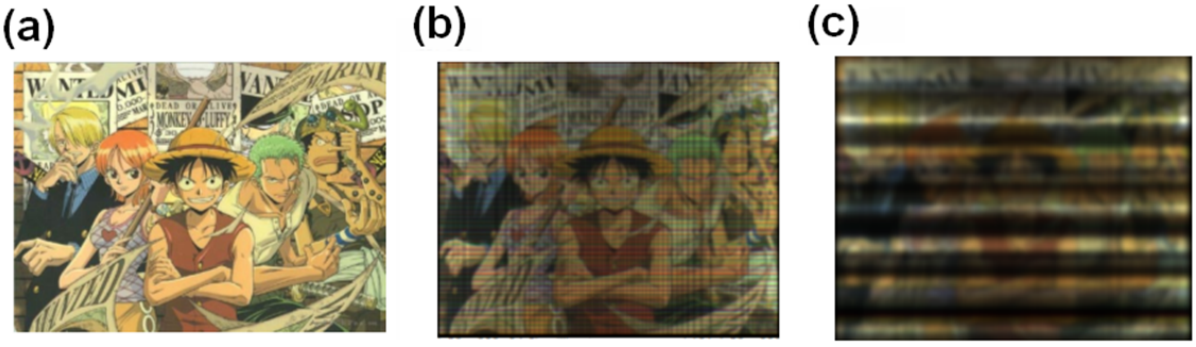

Figure 5-4-4 Simulation verifications for color figure on cylindrical wedge: (a) original image; (b) when L is 4 times of screen width; (c) when L is 1.2 times of screen width

The dark zone phenomenon discussed in previous section also appeared here. It would be more significant when cylinder length get shorter with wedge vertex angle unchanged. Figure 5-4-4(c) shows a pattern with serious dark zone, at this point the cylinder length is 500mm (about 1.2 times of screen width). The projected image would be cut off and

become inconsecutively. Spin out the cylinder length L can reduce the dark zone, but this would increase the size the weight of wedge type circular display. As mentioned in section 5-3, additional procedure on the output surface can also improve the dark zone [5-9].

Experimental Exploration

In this sub-section, experiments are implemented to show the performance our proposed wedge-type circular display in practical situations. This study created cylindrical light guide with material of Acrylic and a wedge-type cross section with vertex angle θ_v of 0.1 degree using computer numerical control (CNC) machining as shown in Fig. 5-4-2. Figure 5-4-5 shows the experimental setup for measuring the image projection of wedge-type circular display.

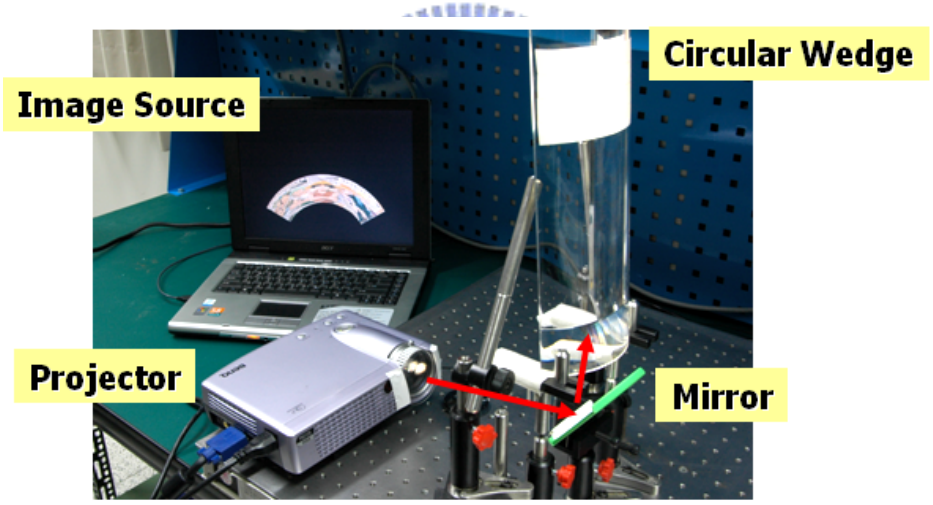

Figure 4-4-5 Experimental setup of cylindrical wedge

The image source was emitted from a commercial DLP^{TM} projector (Benq, Model cp220). To shorten the light path, we fold the ray path by a flat mirror. Following by the discussion of previous subsection, the whole circular display is designed for three frames and in here, for simplification, only 1/3 of wedge-type cylinder was created. A soft diffuser was pasted on the output surface of cylindrical wedge smoothly and was became a screen. According to Eq. (5-4-1), we can consider the require source pattern for desired projected image. After calculation, we produce a single-wavelength pattern and the source arrangement was set as

fan shape. Figure 5-4-6(a) demonstrates the fan-shape source pattern, and Fig. 5-4-6(b) shows the projected image. From the results, one can see the cylindrical wedge indeed can transmit rays and the projected image shows good discernment.

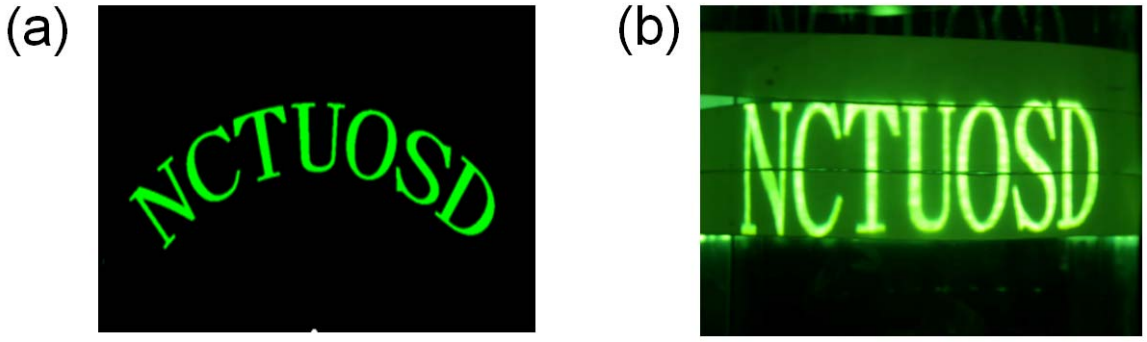

Figure 5-4-6 Single color projection by cylindrical wedge: (a) source pattern; and (b) projected image.

For color image verification, we choose a 400*300 resolution color picture, which is the same as that in the simulation. This picture is also needed to transform into fan-shape arrangement and the result in Fig. 5-4-7(a) shows our cylindrical wedge can restore the picture without distortion. Another example is also provided by choose a real color photograph and Fig. 5-4-7(b) shows the projected result.

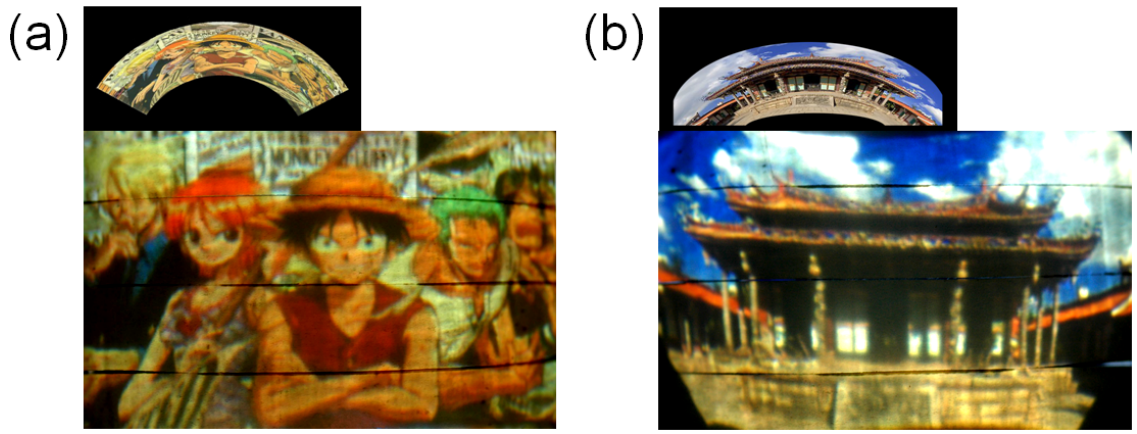

Figure 5-4-7 (a) and (b): Two verifications of color image projection

5-5 Summary

In summary, we analysis and investigate the performance of the ultra-thin wedge-plate display. This study deduces a basic ray transition formula for an ultra-thin wedge-plate display and carries out a traditional aberration analysis. The analytical results show a non-continuous kink-like feature which is confirmed by the computer simulation. At the same time, the third-order approximation is investigated and is compared to total aberration to show the advantage. This study also discusses practical applications of wedge parameters based on this aberration analysis. The analysis results of wedge parameters show that when the wedge plate becomes thinner, the quantity of total aberration would be smaller for some specific ray emitting conditions.

The most observable aberration behavior of wedge-plate display is the kink-like feature, which comes from the dark zone. The dark zone causes a discontinuous image and damage the uniformity. The formation of dark zone in ultra-thin wedge plate has been derived analytically and verified numerically. Reduction of dark zone was also proposed and numerically verified. Additional micro optical elements and an electrically controlled digital panel can help the improvement of aberration and remove dark zone.

On the other hand, we also propose a wedge-plate type of circular display based on the concept of the wedge-plate display, and verify its feasibility by simulation and experimental methods. The experimental results show that such cylindrical wedge can indeed transfer single and multi color images from the commercial projector into circular screen.

Reference

[5-1] M. Laikin, *Lens design*, 3rd ed. (Marcel Dekker, New York, 1991), chapters 26-27.

[5-2] E. H. Stupp and M. S. Brennesholtz, *Projection display*, (Wiley, New York, 1999).

[5-3] A. Travis, T. Large, and M. Buckingham, "Image quality in flat projection wedges," SID Symposium Digest **35**, 850–853 (2004).

[5-4] A. Travis, J. Moore, and J. Zhong, "Optical design of a flat panel projection wedge display," SID Symposium Digest **33**, 461–464 (2002).

[5-5] A. Travis and J. Zhong, "Linearity in flat panel wedge project," SID Symposium Digest **34**, 716–719 (2003).

[5-6] A. Travis, "The focal surface of a wedge projection display," SID Symposium Digest **36**, 896 (2005).

[5-7] D. Korsch, *Reflective optics*, (Academic, New York, 1992); chapter 10.

[5-8] T. C. Wang, "Display apparatus," *US Patent # 5818401* (Oct. 6, 1998).

[5-9] Y.-K. Cheng, S.-N. Chung and J.-L. Chern, “Aberration analysis of a wedge-plate display system,” J. Opt. Soc. Am. A **24**, 2357-2362 (2007).

[5-10] Y.-K. Cheng and J.-L. Chern, "Analysis and reduction of dark zone in ultra-thin wedge plate display," J. Soc. Inf. Display **14**, 813 (2006).

[5-11] Y.-K. Cheng, Z.-Y. Wu, R.-H. Chang, and J.-L. Chern, "Wedge-plate type circular display," SID Symposium Digest **37**, 1035 (2006).

[5-12] J. L. Miller and E. Friedman, *Photonics Rules of Thumb*, (McGraw-Hill, New York, 1996), p. 149.

Chapter 6

Conclusions and Future Works

6-1 Conclusions of Works in Light Pipes and Light Guides

In conclusion, light pipes and light guides have become important elements in present electro-optical systems. Devices which can propagate or conduct light are referred to a generalized light pipe or light guide. The collect and transmissive efficiencies are the key issues for light pipes, while the uniformity and spatial distribution are that for light guides. Our research works have provided fundamental analysis about light pipes and light guides, in the cases of polygonal light pipe, polarization-preserving mechanism, and wedge plate in an ultra-thin display. The deductions in this study provide several ways of tracing ray propagation paths in light pipes and light guides.

We have built up numerical models to describe the behaviors of a large number of rays inside light pipes or light guides. The studying result of this dissertation is to understand the underlying mechanism of such elements so we can go deep into design for facilitation in practical applications. Further study in this area can contribute to an understanding of ray transmission mechanisms, and may lead to improvements in the design and optimization of light pipe systems.

6-2 Future works

In this dissertation, we put our efforts on researches of polygonal light pipe and discussion of ray polarization property. We also put our attention on applications of wedge plate light guide in ultra-thin and circular displays. These results can help light pipe designers design and control spatial profiles or polarization property at the target region, especially in beam shaping or illumination applications. The realizations of new display techniques with large screen, thin thickness, and panoptic view are also provided. However, some important issues remain to be discussed. For future works, we consider several issues to be the extension of our research; they are including different light sources, the influence of light pipe bending, and non-symmetry light pipe shape, etc. These methods can also be extended to multi-wavelength situations, i.e., analyzing color mixing effects. For such a case, the source position should be considered and the dispersion effect of the light pipe material must be shown. Besides, any new type of light pipe or light guide would be also concerned.

作者簡介

鄭伊凱，1976 年出生，台北市人。2009 年 1 月取得交通大學光電所博士。專長於光學系統設計，尤其是以 LED 為光源的各式照明設計，提供光學解決方案。

ykcheng.eo91g@nctu.edu.tw (永久有效)

Publication List

Journal Papers

1. A.-C. Hsu, **Y.-K. Cheng**, K.-H. Chen, J.-L. Chern, S.-C. Wu, C.-F. Chen, H. Chang, Y.-H. Lien and J.-T. Shy, “Far-Infrared Resonance in Split Ring Resonators,” Japan J. Appl. Phys. (Letter) **43**, L176-179, (2004).
2. **Y -K. Cheng** and J. -L. Chern, "Irradiance formations in hollow straight light pipes with square and circular shapes," J. Opt. Soc. Am. A **23**, 427-434 (2006).
3. **Y.-K. Cheng**, S.-N. Chung and J.-L. Chern, “Analysis and reduction of dark zone in ultra-thin wedge plate display,” J. Soc. Inf. Disp. **14**, 813–818 (2006).
4. **Y.-K. Cheng**, S.-N. Chung and J.-L. Chern, “Aberration analysis of a wedge-plate display system,” J. Opt. Soc. Am. A **24**, 2357-2362 (2007).
5. **Y.-K. Cheng**, Meng-Hua Wang and J.-L. Chern, "Irradiance formations of on-axis Lambertian pointlike sources in polygonal total-internal-reflection straight light pipes," J. Opt. Soc. Am. A **24**, 2748-2757 (2007).
6. **Y.-K. Cheng** and J.-L. Chern, “Polarization-preserving angular shifter,” J. Opt. Soc. Am. A **25**, 1558-1563 (2008).
7. **Y.-K. Cheng** and J.-L. Chern, “Design of a Wedge Plate for a Polarization-Preserving Angular Shifter,” (Accepted by Opt. Rev.) (2009).

Conference Papers

1. **鄭伊凱**，吳忠穎，張燃宏與陳志隆,“楔形板環場顯示器,“ 台灣光電科技研討會(2005) (學生論文獎)
2. **Y.-K. Cheng**, Z.-Y. Wu, R.-H. Chang and J.-L. Chern, “Wedge-plate type circular display,” SID Symposium Digest **37**, 1035 (2006).
3. **Y.-K. Cheng** and J.-L. Chern, “Design of a Wedge Plate for Polarization-Preserving Angular Shifter”, ODF (2008).
4. **Y.-K. Cheng** and J.-L. Chern, “Polarization-preserving angular shifter,” Proc. of SPIE Vol. 7059 70590J (2008).

Patents

1. J.-L. Chern, S-N. Chung, **Y.-K. Cheng** and M-D. Chou, “Circular display device with a projective light source”, US 7,123,811(Oct. 17. 2006).
2. J.-L. Chern, S-N. Chung, M-D. Chou and **Y.-K. Cheng**, “Waveguide device for planar display device and related planar display device”. US 20070081783
3. J.-L. Chern, R.-H. Chang, **Y.-K. Cheng** and M-D. Chou, “Projector”, US 20070097339.
4. 陳志隆，張燃宏，**鄭伊凱**與周明德，”投影裝置”，中華民國專利號 I268393 (Dec. 11. 2006).
5. 陳志隆，鍾森年，**鄭伊凱**與周明德，”可將影像畫面投射至柱狀影像傳輸板之外側的環場顯示器”，中華民國專利號 I268393 (Apr. 21. 2008).